Propulsion Systems

Edited by Alessandro Serpi and Mario Porru

Propulsion Systems

*Edited by Alessandro Serpi
and Mario Porru*

IntechOpen

Supporting open minds since 2005

Notice
Statements and opinions expressed in the chapters are these of the individual contributors and not
necessarily those of the editors or publisher. No responsibility is accepted for the accuracy of
information contained in the published chapters. The publisher assumes no responsibility for any
damage or injury to persons or property arising out of the use of any materials, instructions, methods
or ideas contained in the book.

We are IntechOpen,
the world's leading publisher of Open Access books
Built by scientists, for scientists

4,300+
Open access books available

117,000+
International authors and editors

130M+
Downloads

151
Countries delivered to

Our authors are among the
Top 1%
most cited scientists

12.2%
Contributors from top 500 universities

WEB OF SCIENCE™

Selection of our books indexed in the Book Citation Index
in Web of Science™ Core Collection (BKCI)

Interested in publishing with us?
Contact book.department@intechopen.com

Numbers displayed above are based on latest data collected.
For more information visit www.intechopen.com

Meet the editors

Alessandro Serpi obtained his Master's degree in Electrical Engineering and PhD in Industrial Engineering from the University of Cagliari in Italy in 2004 and 2009, respectively. He then did research on power electronics, electrical machines, and drives as a postdoc researcher at the same university, where he became assistant professor in November 2015. His research activity currently concerns the development and implementation of optimal/predictive control algorithms for electrical drives and energy storage systems. Alessandro Serpi is a coauthor of about 90 scientific publications in international journals and conference proceedings and 2 book chapters. He is the proposing associate of "NEPSY" (Novel Electric Propulsion System), an academic spin-off of the University of Cagliari that was set up in August 2017.

Mario Porru obtained his Bachelor's and Master's degrees in Electrical Engineering and PhD in Electronic and Computer Engineering from the University of Cagliari, Italy, in 2009, 2011, and 2015, respectively. From 2015 to 2018, he was a postdoc researcher at the same university, where he has recently become assistant professor of power electronics, electrical machines, and drives (April 2018). His research activity focuses on the management and control of energy storage systems and highly integrated electric propulsion systems. He is a coauthor of about 30 papers published in international conference proceedings and journals and 1 book chapter. Mario Porru is a cofounder and associate of NEPSY (Novel Electric Propulsion System), a spin-off company of the University of Cagliari.

Contents

Preface

The transport sector is one of the most valuable sectors in the world. It represents the large oil consumers but still relies mainly on fossil fuels. Since the world trend in fossil fuel use is expected to increase further, a more sustainable transportation system is unavoidable to cope with emerging economic and social issues, such as massive energy consumption and emissions of pollutant gases. In this regard, several solutions are possible, among which are improving the energy efficiency of conventional propulsion systems, using alternative and less-pollutant fuels, and/or employing hybrid and full-electric propulsion systems. In particular, transport electrification is a very promising and suitable solution because it increases well-to-wheel efficiency and reduces emissions, also through the use of a mix of energy sources; this reduces the dependence of the transport sector on oil, especially in those countries where a high share of electricity is or will be produced by renewable energy sources.

In this scenario, this book provides an overview of some recent and promising technological advancements in propulsion systems, ranging from on-board components to different propulsion system architectures. In particular, the first chapter presents a survey of the most employed propulsion systems for liquefied natural gas carriers: each propulsion solution is analysed and compared with others in terms of economic factors, efficiency, and emissions. The second chapter deals with road vehicles, namely the main electrical subsystems for a zero emissions vehicle are presented and discussed, which consist mainly of energy storage systems, power electronic converters, traction motors, and charging infrastructures. Electric propulsion systems are also the topic of the third chapter, which presents their application to distributed propulsion of unmanned aerial vehicles (UAVs); in particular, the design of two UAVs characterized by different electric propulsion systems is presented and discussed by highlighting the most important features of each design solution. The fourth chapter of the book deals instead with laser-based propulsion systems, which are particularly suitable for space vehicles. The operating principles of different laser propulsion systems are described and discussed by highlighting the most important advantages and issues that still need to be addressed. The fifth and last chapter of the book is on Hall thrusters, especially on the erosion process of the discharge chamber (DCh); in this regard, methods of how to measure the DCh erosion process are presented; one of which is analysed and discussed in detail.

In conclusion, the book will provide a brief but significant insight into propulsion system design and architecture by covering different topics and application fields (road, marine, and aerospace). In this regard, electric propulsion systems are becoming increasingly attractive with the aim of reducing pollutant emissions and increasing propulsion efficiency, not only for road vehicles but also for the marine and aerospace sectors. Therefore, although full-electric propulsion systems may not be economic and/or technically viable in all sectors yet, the increasing use of hybrid propulsion systems reveals that the transition from conventional fuel-based to full-electric propulsion has started, which could be accomplished in the next few

decades due to the expected technological advancements of energy storage systems and electric drives.

Dr. Alessandro Serpi and Dr. Mario Porru
Department of Electrical and Electronic Engineering,
University of Cagliari,
Italy

Chapter 1

Options and Evaluations on Propulsion Systems of LNG Carriers

Tu Huan, Fan Hongjun, Lei Wei and Zhou Guoqiang

Abstract

The LNG carriers are undergoing a period of rapid and profound change, with much larger size ships and novel propulsion systems emerging for fulfilling the market trends of LNG shipping industry. There are various proposed propulsion solutions for LNG carriers, ranging from the conventional steam turbine and dual fuel diesel electric propulsion, until more innovative ideas such as slow speed dual fuel diesel engine, combined gas turbine electric & steam system, and hybrid propulsion based on steam turbine and gas engine. Since propulsion system significantly influenced the ship's capital, emission regulation compliance and navigation safety, the selection of a proper propulsion option with technical feasibility and economic viability for LNG carriers is currently a major concern from the shipping industry and thus must be comprehensively assessed. In this context, this chapter investigated the main characteristics of these propulsion options in terms of BOG treatment, fuel consumption, emission standards compliance, and plant reliability. Furthermore, comparisons among different propulsion system were also carried out and related evaluation was presented.

Keywords: LNG carrier, propulsion system, steam turbine, gas turbine, dual fuel diesel electric propulsion, slow speed dual fuel engine

1. Introduction

The LNG shipping industry had been tremendously cautious in choosing the propulsion system, and the steam turbine had been practically an exclusive option for LNG carriers over the last several decades. Influencing factors including economic consideration, environmental regulation, as well as safety issues made a profound impact on the technology developments implemented on LNG carrier propulsion systems. Since 2004 many LNG carrier projects with propulsion other than steam turbine have been under construction, such as dual-fuel diesel electric propulsion and two-stroke diesel engine propulsion with reliquefaction plant. Steam turbine domination in the LNG carrier sector has been gradually broken. So far there is no standard propulsion system that applicable to all types of LNG carriers [1, 2].

The development history of the propulsion system for LNG carriers is presented in **Figure 1**. Steam turbine has been the dominating propulsion plant used on LNG carriers since 1960. Because it offers dual fuel burning capability, low maintenance cost and high reliability. However, in order to improve operational efficiency, reduce engine room size and increase cargo capacity, a number of alternative propulsion
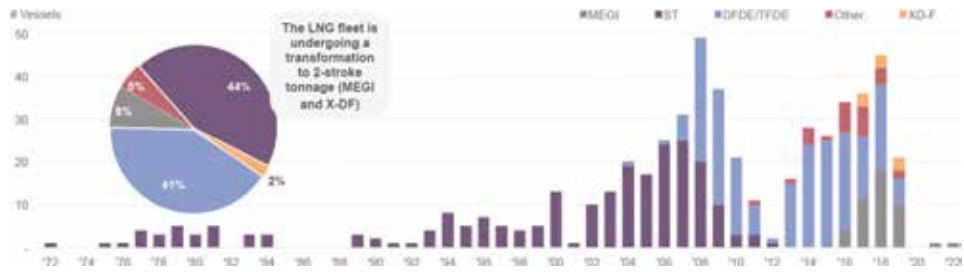
Figure 1.
LNGC fleet and order book by propulsion type (as of May 2017).

options have been developed in the industry. In 2004, the four-stroke dual fuel engine broke the domination of the steam turbine and started to be used on LNG carriers as a part of dual fuel diesel electric propulsion system. After 2010, two-stroke dual fuel technology has made a breakthrough and has been applied to LNG carriers, including both the high pressure and low pressure gas injection concept. The two-stroke dual fuel engines can offer substantial efficiency advantages over both the DFDE and steam turbines. So they become a popular propulsion system choice for LNG carriers.

The driving factors for the development of the propulsion system come from the following three aspects [3]:

- *Change of trade pattern*. Traditionally, LNG was almost exclusively traded under inflexible long-term contracts and the vessels are operating on fixed sailing routes. However, the proportion of short-term contracts and even spot cargoes has increased substantially since 2000. So this change requires a more flexible and efficient propulsion system to accommodate various operating profiles.

- *Upgrading of emission regulation*. The NOx emission limits and the Energy Efficiency Design Index (EEDI) are getting more and more stringent. In order to comply with the stricter regulation, the propulsion plant has to improve its emission performance and fuel efficiency.

- *Improvement on insulation technology*. The boil off rate is significantly reduced due to the improvement in LNG tank insulation. This results in the insufficient BOG to fuel the propulsion plant and leads to the development of alternative more fuel efficient propulsion systems.

After an exhaustive review of works related to propulsion systems of LNG carriers, an extensive variety of systems installed on board has been found, ranging from turbines to internal combustion engines with endless variants. Therefore, the purpose of this chapter is to investigate the various LNG carrier propulsion systems, taking into account the latest technology progress and innovation in this field.

2. Characteristics of LNG carriers

2.1 Size of LNG carriers

The size of an LNG carrier is based on its obtainable volumetric capacity of liquid natural gas in m^3. The most common size of LNG carriers delivered or on order is between 120,000 and 180,000 m^3, and often referred to as conventional type [4]. The demand for lower LNG transportation costs is most effectively met

LNG carrier classes	Dimensions	Ship size—LNG capacity
Small	B: up to 40 m, L_{OA}: up to 250 m	Up to 90,000 m^3
Small conventional	B: 41–49 m, L_{OA}: 270–298 m	120,000–149,999 m^3
Large conventional	B: 43–46 m, L_{OA}: 285–295 m	150,000–180,000 m^3
Q-flex	B: approx. 50 m, L_{OA}: approx. 315 m	200,000–220,000 m^3
Q-max	B: 53–55 m, L_{OA}: approx. 345 m	More than 260,000 m^3

Table 1.
LNG carrier classes.

by increasing the LNG capacity of the LNG carriers. Thus, the LNG carriers to and from Qatar ordered over the last few years are of the large sizes of approx. 210,000 and 265,000 m^3, and referred to as Q-flex and Q-max, respectively. The LNG carrier classes often used today can therefore be referred to as listed in **Table 1**.

2.2 Trade mode changes

The traditional LNG trade mode is based on long term shipping contracts and dedicated fleets of ships sailing on the fixed routes and schedules between LNG terminals in the world. The LNG supply chain does not have much buffering capacity and it is very important that the cargo is delivered on time. However, due to the increasing demand and supply of LNG the number of short-term contracts and even spot trade has increased significantly.

From the shipping point of view this means that the operators are bound to look for ships with more operational flexibility and efficiency in response to varying contractual situations. Primarily this calls for a flexible and efficient propulsion plant able to accommodate different ship speeds and alternative operating profiles [3].

2.3 Boil-off gas problem

Most of LNG carriers have the boil-off gas problem which takes place during storage, loading or discharging and the ship's voyage. LNG carriers are designed to carry natural gas in liquid form at a temperature below its boiling temperature point. Despite tank insulation designed to limit the admission of external heat, even a small amount of it will cause slight evaporation of the cargo, known as boil-off gas (BOG). The amount of liquid that is evaporating from cargo due to heat leakage and expressed in % of total liquid volume per unit time. Typical values are 0.15%/day or below, recent projected LNG carriers are offered with a boil off rate close to 0.1%.

The BOG result from natural evaporation is unavoidable and has to be removed from the tanks in order to maintain the cargo tank pressure. To relieve the pressure in LNG tanks, BOG can be re-liquefied, used as fuel or burned in a combustion unit. Reliquefaction occurs when evaporated LNG is cooled and reverted back to its liquid state. Excess gas can also be led to the engines which have a capability of burning gas fuel. Another alternative is to burn the unwanted gas in a combustion unit, but this results in wastage of materials and valuable energy.

2.4 Evolution on containment system

Categorization of containment systems for LNG carriers is shown in **Figure 2**. The IGC code categorizes cargo tanks into two main types: integral tanks and independent tanks. In addition, the integral tanks are mainly of membrane type and the
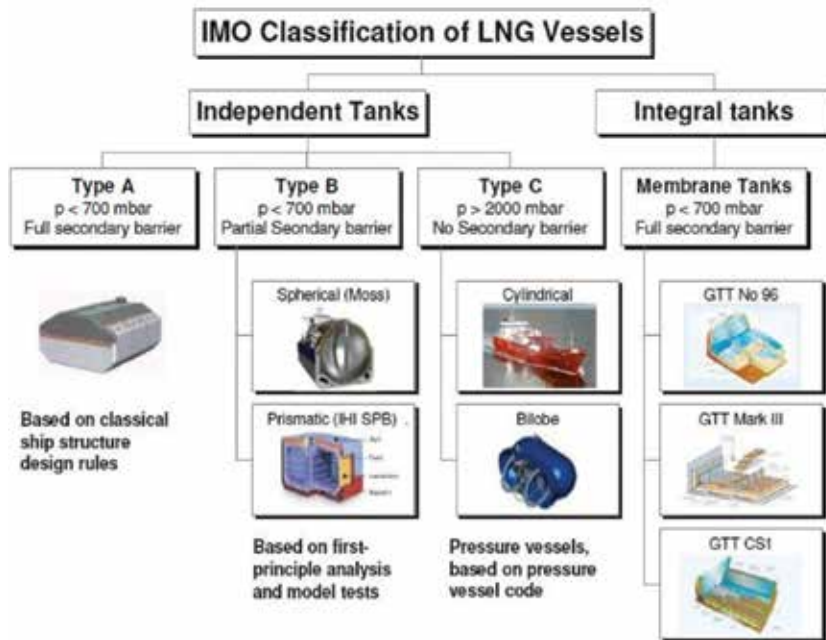
Figure 2.
Categorization of containment systems for LNG carriers.

independent tanks can be further classified into three subcategories, which are referred to as Type A, Type B and Type C. For small-scale LNG carriers and LNG fuelled ships other than LNG carriers, we typically use type C tank. On large-scale carriers, type B and membrane tanks are mainly used. From the fleet breakdown by containment system, we found that over 70% of the active fleet had a membrane tank. This is most likely because prismatic membrane tanks utilize the hull shape more efficiently, and thus have less void space between the cargo tanks and ballast tanks. However, self-supporting type B tanks are more robust and have greater resistance to sloshing forces.

2.5 Regulatory framework

The safety requirements for the propulsion system are specified by the international code and classification rules and the regulatory framework is constantly improving along with the development of the propulsion system. Since the dual fuel engines are extensively used on LNG carriers, the revised IGC code has included the gas-fuelled engines. IACS proposed new Unified Requirement to cover the low pressure gas engines. Classifications also issued dedicated rules or guidelines for propulsion system applied on LNG carriers. ABS (American Bureau of Shipping) has issued guide for propulsion systems for LNG carriers, and CCS (China Classification Society) has released guidelines for design, installation and testing of gas engines on LNG carriers [5, 6].

3. Propulsion options for LNG carriers

The propulsion system for LNG vessels is closely related with the generation and consumption of the BOG [7]. There are various proposed propulsion systems being used and considered by the industry. From the categorization of propulsion systems for LNG carriers as shown in **Figure 3**, we can see that the prime movers include steam

Figure 3.
Categorization of propulsion systems for LNG carriers.

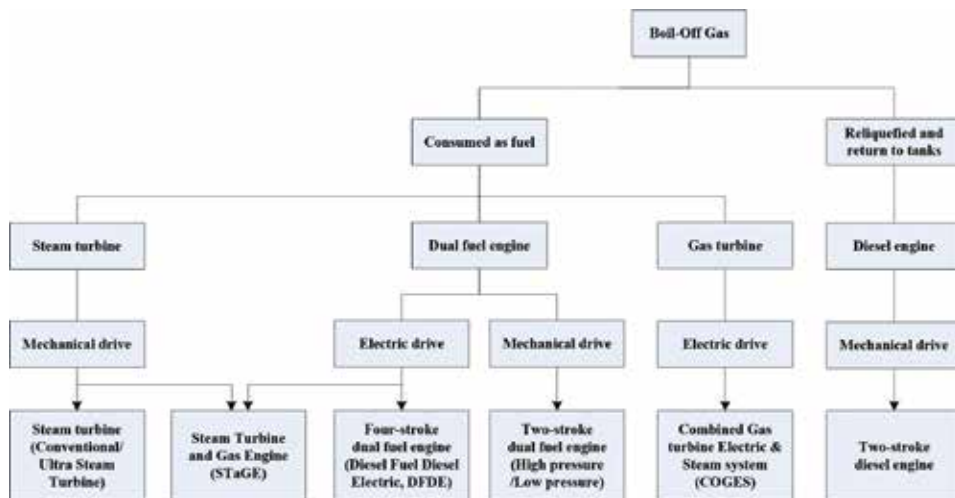turbine, gas turbine, diesel engine, dual fuel engine. Based on the prime movers and their combinations, we have six propulsion system options, including steam turbine propulsion, dual fuel diesel electric propulsion, slow speed dual fuel engine propulsion, gas turbine propulsion, slow speed diesel engine propulsion with re-liquefaction plant, and hybrid propulsion system based on steam turbine and gas engine.

3.1 Steam turbines

Figure 4 shows a simplified schematic of a typical steam propulsion system. A steam turbine based propulsion system usually comprises two gas/HFO fuelled boilers supplying overheated high pressure steam, typically at a pressure of 60–70 bar at 520°C, to the high and low pressure turbines driving a single propeller via a reduction gearbox [8, 9]. The steam is also used to feed turbo generators which provide electric power for auxiliary services (e.g., hotel load, powering pumps). Two turbo generators are installed to guarantee the redundancy, and each one has a power capacity capable of covering the peak load demand which is normally during full rate cargo discharge. Two auxiliary diesel engines are installed as well, with a combined capacity equal to one of the turbo generator sets, as a safety requirement to supply sufficient power during black outs. The excessive BOG generated in situations when the steam turbine is out of service or at low load is also burned in the boilers, and the steam generated is dumped in the condenser to dissipate the energy to the sea. Through this simple philosophy it is able to stabilize the tank pressure, eliminating the need for a gas combustion unit (GCU).

The boilers can burn the heavy fuel oil (HFO) and boil-off gas (BOG) simultaneously at any liquid/gas ratio, thus offering a very easy method to handle the BOG. In addition, the steam turbine propulsion is also featured with ease of use, intrinsic reliability, and reduced maintenance costs. However, the steam turbine has the lowest overall efficiency of the propulsion system available, approximately 35% at full load and the efficiency becomes lower as the turbine load goes down, which directly led to high fuel cost and the resulting high CO_2 emissions. Another disadvantage is the steam turbine is not space efficient, so in the case of Q-Flex/Q-Max ships with twin screw designs, it is very difficult to arrange side by side steam turbine machinery in the engine rooms. Therefore, steam turbine propulsion is not a feasible solution for Q-Flex/Q-Max ships.
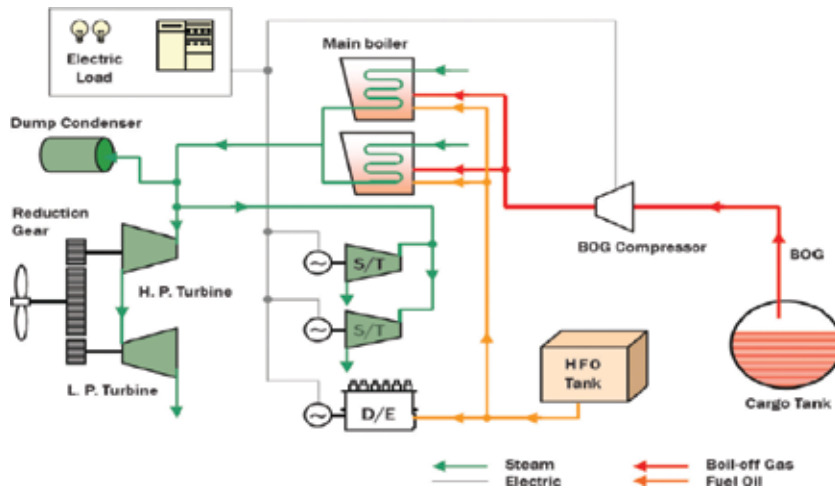
Figure 4.
Simplified schematic of a steam propulsion system [9].

3.2. Dual fuel diesel electric

The other big group of vessels with non-steam propulsion is featured with Dual Fuel Diesel Electric plants (DFDE). The DFDE configuration provides a more straightforward and simple layout of the propulsion system. The DFDE propulsion system employs multiple engines of the same type, typically four or five, coupled to electrical generators to supply energy to the entire ship including propulsion, which is driven by means of electric motors [10]. The schematic of a four-stroke DFDE propulsion system is shown in **Figure 5**.

Dual fuel engines can operate on BOG, MDO or HFO. Duel fuel engines have different operation modes depending on the fuel to be used. When gas is burned as fuel (gas mode), the engine adopts the concept of the lean Otto cycle. On the contrary, if MDO or HFO are used, the engine operates at diesel cycle (diesel mode).
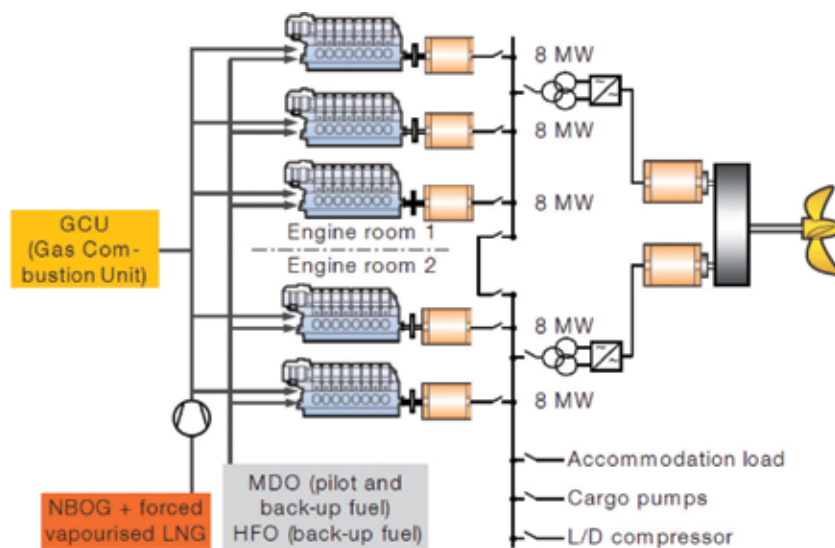
Figure 5.
Schematic main machinery of a four-stroke DFDE plant [10].

In Gas Mode, the BOG is injected to the air intake before each cylinder individually through a gas admission valve, where it is mixed with the charged air before entry to the combustion chamber. The mechanism enables the compressing and injecting of the BOG at a relatively low pressure, approximately 5–6 bar, which reduce the complexity of the fuel gas supply system and thus the risks using methane at high pressure in the engine room. A small amount (approx. 1%) of MDO is also required as a pilot fuel when operating on gas, giving a high-energy ignition source for the main fuel gas charge in the combustion chamber. In diesel mode, the DF-engine works resemble any diesel engine, utilizing traditional jerk pump fuel injection system. Switching between the two operating modes can be conducted stably without interruption in power supply. Gas mode and diesel mode follow the different operating principles, and as a result they have different operating features. The diesel mode performances better in terms of thermal efficiency and dynamic response, while the Gas mode has advantages in terms of fuel cost and exhaust emissions.

The combustion control system is an important issue that must be taken into account in DF engines. In gas mode following Otto cycle, as the engine load increased along with the mean effective pressure, the operating window between misfiring and knocking becomes narrower. To stay within the operating window and have optimal performance for all cylinders regarding safety, efficiency and emissions in all conditions, it requires a system to control the combustion process each cylinder individually and precisely.

The largest dual fuel engines available can develop 950–1000 kW per cylinder and are configured as L-type of 6–9 cylinders or V-type of 12–18 cylinders. The number of engines and configuration of cylinder are selected so as to provide as near optimal loading as possible for the engines required to be operated during the various working conditions of the vessel. With a multi-engine configuration, the DFDE propulsion system provides a superior performance in terms of redundancy and safety.

If there is more BOG available than the power required for the propulsion or electric load, then the excess BOG is sent to the gas combustion unit (GCU). The installed capacity of GCU is usually sized to handle the total BOG capacity on a typical laden journey.

In the DFDE concept, since the power demand for propulsion and cargo handling are in different operating time phase the installed power of the ship can be considerably reduced compared with other mechanical propulsion system, which is a notable advantage. The drawback of this propulsion system is the high investment and maintenance costs, resulting from the dual fuel engines and the increased amount of equipment comprised in the electric propulsion system.

3.3 Two-stroke slow speed diesel engine with re-liquefaction plant

Two-stroke slow speed diesel engines are predominant propulsion plant in merchant shipping, which is benefit from its high efficiency, capability of burning low-quality low cost fuels, and low maintenance costs. Since the two-stroke slow speed engine is a single fuelled (HFO) propulsion plant without a BOG burning capability, the natural BOG from cargo tanks shall be liquefied and sent back to cargo tanks. With the increase in LNG carrier's dimension to approximately 210,000 and 265,000 m^3, referred to as Q-flex and Q-max respectively, the volume of BOG of the tanks has increased significantly and is now within the capacity range of re-liquefaction plant. In this context, the two-stroke slow speed diesel engines with re-liquefaction plant turn into a feasible and attractive option for the ship owners. For this kind of propulsion concept, the abbreviation SSDR is typically used for reference.

The schematic main machinery of a two-stroke diesel engine powered LNG carrier with re-liquefaction plant is illustrated in **Figure 6**. The main machinery of
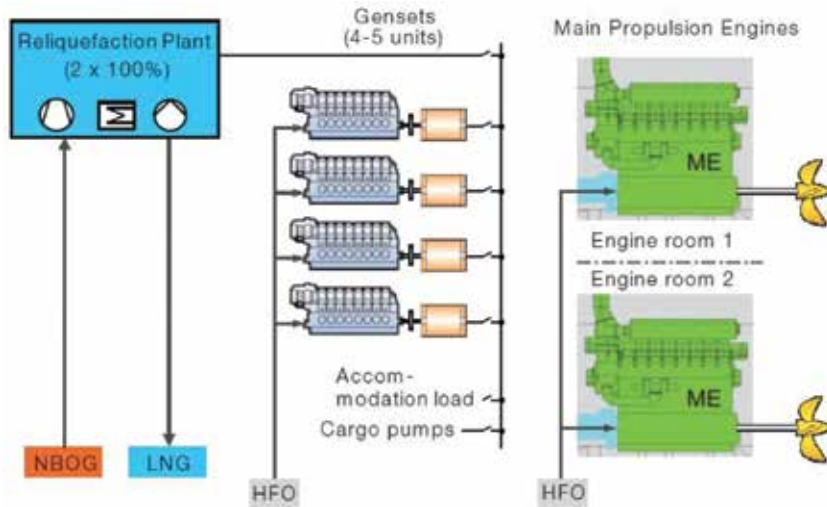
Figure 6.
Schematic main machinery of a two-stroke LNG carrier with re-liquefaction plant [10].

SSDR based LNG carrier of Q-flex/Q-max size typically comprises two low speed diesel engines for propulsion in twin screw format, and four auxiliary generator sets for electric power generation. The re-liquefaction plant is used for re-liquefying the BOG generated in cargo tanks and returning it to into a liquid state, maintaining a proper pressure in cargo tanks, and moreover avoiding any wastage of the LNG being transported. Besides, a GCU is also equipped to burn the BOG generated which, in case of re-liquefaction plant failures, would be impossible to treat, avoiding the pressure increase in the tanks and could cause great damage.

The BOG re-liquefaction principal is based on a closed cycle using nitrogen as a refrigerant, absorbing the heat from BOG. In this cycle, cargo boil off is suctioned from the LNG tanks and compressed to 5 bar by a low duty compressor, and then the vapor is cryogenically cooled to −160°C in a heat exchanger. This ensures condensation of all hydrocarbons in the BOG so they can be converted back to LNG, while the nitrogen and other non-condensable remain at gaseous state. These gas impurities are finally removed in a gas-liquid separator where the LNG is separated and delivered back to the cargo tanks with the nitrogen-rich non-condensable gases either discharged to the atmosphere or burnt in the GCU.

The operation of a re-liquefaction plant requires a high electric power supply by auxiliary generators composed of either 3 or 4 power generators. Taking the case of a 149,000 m^3 LNG vessel, the re-liquefaction plant has a consumption of 3.5-7 MW depending on the BOG generated in the cargo tanks. The vessel's net auxiliary power is therefore increased to the order of 14 and 16 MW. Considering the overall performance of the system, the tremendous power consumption of the re-liquefaction plant substantially diminishes the efficiency advantages provided by the two-stroke slow speed diesel engines.

3.4 Slow speed dual fuel engine

The propulsion system of choice for the majority of LNGC new buildings was the four-stroke engine based DFDE option, from around 2002 until 2012. In December 2012, the slow speed two-stroke dual fuel engines received the first orders for a pair of gas fuelled container vessels, marked the beginning of the two-stroke dual-fuel power train era. Dual fuel engines of two-stroke low-speed

types offer major propulsive efficiency advantages over both the DFDE and steam turbines, the most popular propulsion system options during the early stages of development for LNG carriers. Distinct technical routes have been adopted by the two main manufacturers. MAN Diesel & Turbine utilize the high pressure concept while Wartsila focuses on the low pressure concept.

Initial LNG ship owner interest in two-stroke, dual-fuel propulsion was focused primarily on the MDT high-pressure plant, known as its Mechanically operated, Electronically controlled, Gas Injection (ME-GI) diesel engine. In recent years, the WinGD low pressure X-DF two-stroke engines have also undergone substantial development and application [11].

3.4.1 High pressure

Figure 7 shows the schematic main machinery of a ME-GI propulsion plant. The ME-GI high pressure gas engines operate on the diesel cycle. The BOG is pressurized through the fuel gas supply system (FGSS), and then directly injected at high pressure (250–300 bar) into the cylinder after the diesel pilot fuel has ignited near the top dead center. It is claimed that this concept would have significant advantages compared with the premixed Otto cycle gas process, i.e. eliminates the risk of knocking and capable of burning gas from any source irrespective of the methane number, due to the fact that the fuel gas is not involved in the compression stroke. This concept makes it possible to utilize high compression ratio designs, thereby offering higher energy efficiency. For a LNG carrier with a capacity of 145,000 m^3 or larger, double ME-GI engine solution is the most attractive option, providing the redundancy in terms of propulsion.

The high pressure FGSS for ME-GI engines have two basic system configurations. One system where a piston compressor feeds the ME-GI with high-pressure fuel gas, and one system where an LNG pump and a vaporizer feed the ME-GI with high pressure gas [12, 13]. Besides, a combined option based on the compressor and the LNG pump solution also offers a feasible configuration. For dealing with the BOG exceeds the capability of FGSS or the demand of the engines, a full or partial re-liquefaction system can be installed on board.
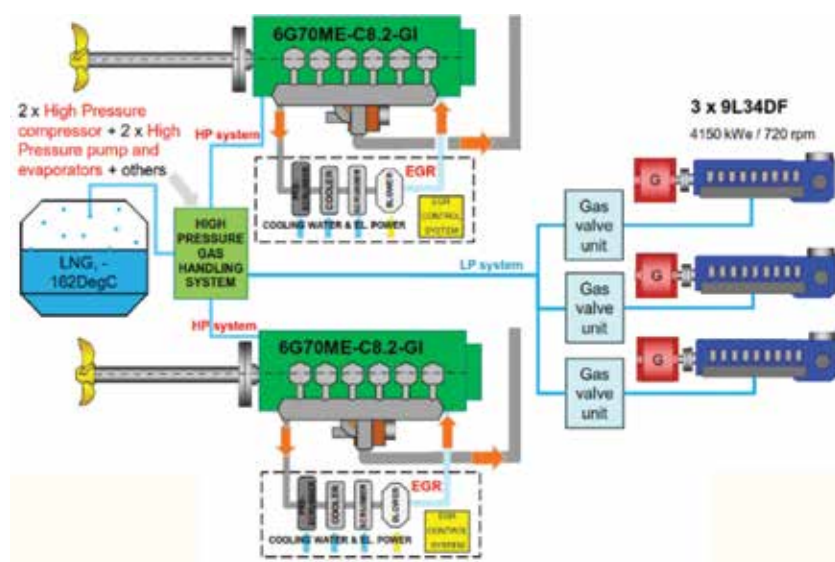

Figure 7.
Schematic main machinery of a ME-GI propulsion plant (high-pressure gas).

The high pressure gas is supplied from the FGSS to the engine room through a double wall piping system, where the gas fuel is contained in the inner pipe and space between the gas fuel piping and the wall of the outer pipe or duct shall be equipped with mechanical underpressure ventilation. This specific arrangement secures that the engine room is regarded as an ordinary engine room rather than a hazardous area, which complies with requirement of "inherently gas safe machinery spaces" specified in the IMO IGF code.

In terms of emissions, the high pressure two-stroke engines reduce the NOx emissions by 40% compared to HFO without exhaust gas treatment, which fulfills the IMO Tier II NOx limits. To achieve Tier III limits, ME-GI engine requires equipping with an EGR or SCR system. Furthermore, the CO_2 emissions are reduced by approximately 24% and methane emissions are at a very low level.

3.4.2 Low pressure

Figure 8 shows the schematic main machinery of an X-DF propulsion plant. The low pressure X-DF technology is based on the lean-burn Otto cycle, in which fuel and air are premixed and burned at a relatively high air-to-fuel ratio. When gas admission in the cylinder occurs, the piston is at about mid stroke of the compression phase and therefore the pressure in the combustion chamber is low. This allows the gas to be injected at low pressure, ranging from 5 to 16 bar. With the low-pressure gas injection, the gas-air mixtures need an ignition source to start the combustion. The most common ignition method is using a fuel oil pilot injection, with the amount of fuel as low as 0.5% of the total injected fuel [14].

The low pressure concept offers the possibility of applying a simple FGSS, since the fuel gas is mixed with the scavenge air at about mid stroke position, the required gas injection pressure is below 16 bar at any operating point. It is claimed that the FGSS is relatively simple, reliable and well-proven. In addition, low pressure gas supply means wider selection of system vendors and installation of less auxiliary engine power, thereby lowering the investment and operating costs.

The most significant advantage of the low-pressure X-DF engine is the low level of emissions of any exhaust gas element. As the low-pressure X-DF engine has a pre-mixed homogeneous lean mixture of gas and air in the combustion chamber, the
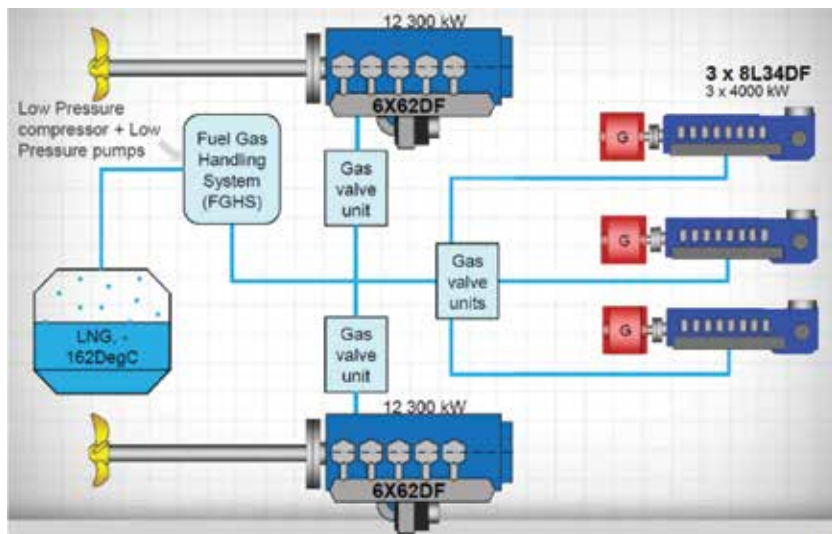

Figure 8.
Schematic main machinery of a X-DF propulsion plant (low-pressure gas).

flame temperatures are relatively low. This results in low levels of NOx production without any after treatment system, approximately 50% of the IMO Tier III limits. Besides, the weighted average of relative methane emission is about 3 g/kWh.

3.4.3 Comparison of the two options

Since WinGD X-DF and MAN ME-GI use distinct technical routes, each option has its own advantages and disadvantages in terms of power performance, emission and economy, as the comparison shown in **Table 2**. The low pressure engines have certain advantages in terms of NOx emissions, gas fuel supply systems and investment costs, while high pressure engines perform better in terms of power, thermal efficiency, gas compatibility and methane slip [15].

	Low pressure (WinGD X-DF)	High pressure (MAN ME-GI)
Power performance	• BMEP: 17.3 bar • Output: approx. 17% lower than the diesel engine counterpart • Dynamic response: poorer than diesel engine	• BMEP 21 bar • Output: comparable with the diesel engine counterpart • Dynamic response: comparable with diesel engine
Thermal efficiency	Approx. 47%	Approx. 50%
NOx emission	IMO Tier III	IMO Tier II
CH4 slip	3 g/kWh	0.2 g/kWh
Methane Number (MN)	MN ≥ 65 (DCC technology)	Adapt to various MN
Gas consumption	140–142 g/kWh @100%MCR	136–138 g/kWh @100%MCR
Pilot fuel consumption	• 0.8 g/kWh@100%MCR • 2.7 g/kWh@30%MCR	• 5 g/kWh@100%MCR • 12 g/kWh@30%MCR
Fuel gas supply system	• LNG pump: centrifugal pump, with simple structure and low maintenance requirement • Low pressure gas compressor: a large variety of products, small size and weight, low energy consumption • Low pressure vaporizer: low cost and mature technology	• Low pressure vaporizer: low cost and mature technology • High pressure gas compressor: few products, large size and heavy weight, high energy consumption
CAPEX	• For LNG fuelled vessels, the CAPEX of high pressure fuel and gas supply system is approx. 15% higher. • For LNG carriers, the CAPEX of high pressure fuel and gas supply system is approx. 40% higher.	
OPEX	The two options are comparable	

Table 2.
Comparison of the low pressure system and high pressure system.

3.5 COGES propulsion

Aircraft derivative gas turbine has been used as propulsion machinery for navy ships and electric power generator combined with steam or diesel generators for cruise vessels. The gas turbine is an innovative option introduced on LNG vessels because of their dual fuel (gas and diesel oil) burning capability, high reliability

derived from the aeronautical industry, high power/weight ratio, and excellent emission performance [16]. However, the relative low thermal efficiency along with the requirement of using MGO as a backup fuel which with a relative high price, hampers the gas turbines to be an attractive option to be applied on LNG carriers. The gas turbines combined with a steam turbine cycle for waste heat recovery, referred to as Combined Gas turbine Electric & Steam system (COGES), enable the overall efficiency increase to 40%.

With the COGES system, the gas turbine drives the generator, which feeds into the main switchboard in turn and provides the electric power and propulsion demand. The propeller is driven by a frequency-controlled electric motor. The exhaust gases from the gas turbine are used to raise steam in a heat recovery steam generator (HRSG). This steam drives the steam turbine generator in turn, which also feeds into the main switchboard.

The schematic main machinery of a COGES propulsion plant (Rolls-Royce) is illustrated in **Figure 9**. The COGES designed by the manufacturer Rolls-Royce has two GTs with different powers, one of 36 MW and another of 5 MW. In addition, a 10 MW steam turbine is coupled with a HRSG. During sailing, only the main GT, HSRG, and steam turbine would be in service, providing the electric power and propulsion demand. The purpose of the less powerful turbine (5 MW) is to generate power at port, hence avoiding running the main GT at high fuel consumption.

Another COGES configuration is designed by the manufacturer General Electric. The schematic main machinery of this COGES propulsion plant (General Electric) is illustrated in **Figure 10**. The COGES system has two 20 MW gas turbines, thereby increasing the reliability because the system could guarantee 50% of the electric power supply to continue with the voyage in case of a GT failures. However, as it does not have a low power auxiliary generator as in the case of the Rolls-Royce design, this will result in high consumption while at port. This system requires installing a more powerful steam turbine, approximately 15 MW, to meet the larger demand of waste heat recovery.

The primary disadvantage of gas turbines is the relatively high capital cost, stemming from the fact that the overall drive system is more complex and expensive than mechanical drives. For a 20–30 MW class gas turbine, its capital cost is approximately 15–20% higher than its diesel engine counterpart. Besides, gas turbines do not have their line-up of engine types for the customer's selection upon various power demands like diesel engines.
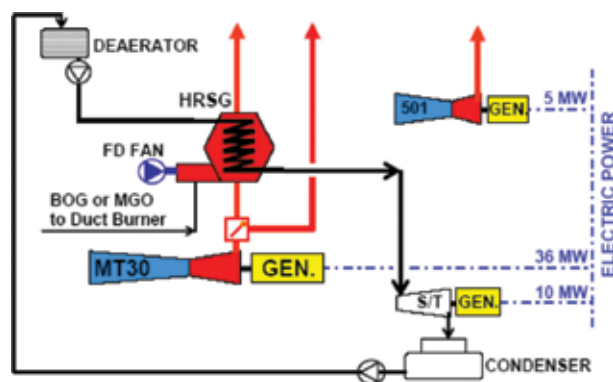
Figure 9.
Schematic main machinery of a COGES propulsion plant (Rolls-Royce).
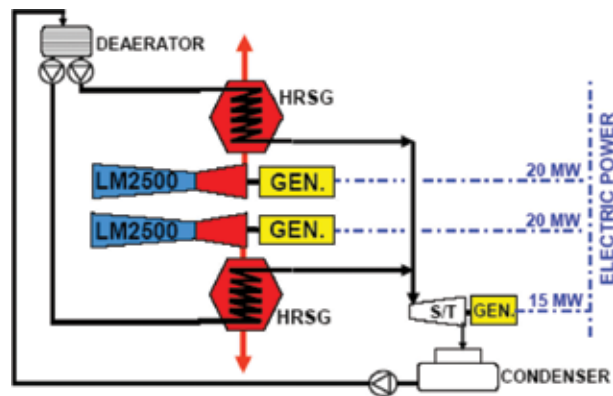
Figure 10.
Schematic main machinery of a COGES propulsion plant (General Electric) [20].

3.6 STaGE propulsion

STaGE is an abbreviation for Steam Turbine and Gas Engine, which is a hybrid propulsion system that comprises an ultra-steam turbine (UST) plant on the port side and a combination of a dual-fuel engine and a propulsion electric motor (DFE-PEM plant) on the starboard side [17]. The dual-fuel engine can work on both gas and oil. The configuration of a STaGE propulsion plant is shown in **Figure 11**.

By using a waste heat recovery system of STaGE plant, the exhaust gas and jacket waste heat from the dual-fuel engine are recovered to heat the feed water going toward the UST plant, achieving significant improvement in fuel efficiency. In the UST plant, the heated feed water flows to the boiler to generate steam to be used to drive the turbine. The electricity generated by the dual-fuel engine drives the propulsion electric motor. Typically, a huge amount of waste heat from the dual-fuel engine is dumped into the exhaust-gas and jacket cooling water. But the STaGE plant uses the waste heat to heat the boiler feedwater, enhancing the total
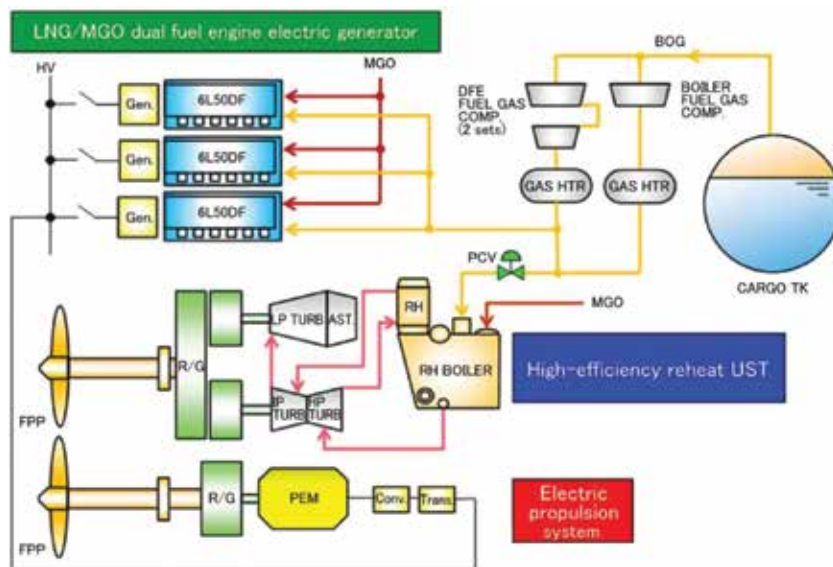
Figure 11.
Schematic main machinery of a STaGE propulsion plant (Mitsubishi Heavy Industries) [17].

efficiency of the propulsion plant. The waste heat from the dual-fuel engine is also recycled to generate auxiliary steam as well as the drive steam for the main turbine, also enhancing total efficiency. Instead of a turbine generator used in conventional steam turbine plants, the power generator of the dual-fuel engine supplies power to the ship, achieving a simpler plant configuration and higher efficiency. As such, the STaGE plant achieves significant efficiency enhancement by combining two different propulsion engines and by optimizing the waste heat energy.

A typical LNG carrier equipped with STaGE plant emits about 40% less CO_2 per cargo unit than conventional LNG carriers with a cargo capacity of 147,000 m^3 propulsed by a conventional turbine plant. Furthermore, gas burning is available in all operation modes, including in harbors, achieving high environmental performance that meets the IMO Tier III emission regulations implemented in the global ECA. The STaGE plant gains high-reliability by combining the proven turbine plant and DFE-PEM plant and high-redundancy by using different propulsion systems on both port and starboard sides.

4. Comparison and evaluations

4.1 Economic factors

Figure 12 indicates the trends of investment cost and delivery schedule of LNG carriers of different propulsion system. During the 2000s, the average construction cost of LNG carrier kept within a narrow scope. The swift increase in demand for vessels using new propulsion technologies starting from 2014, particularly DFDE propulsion based vessels, pushed average construction costs to rise from $1300/m^3 in 2005 to $1770/ m^3 in 2014. This increase was mainly due to the icebreaker vessels in Yamal LNG project. Nevertheless, the costs for TFDE and ME-GI vessels in 2017 reduced to $1072/m^3 and $1082/m^3, respectively [18].

In most cases, it takes 30–50 months to complete the construction of a vessel after the order is confirmed. However, the different type of propulsion system also affects the delivery schedule of the vessels. For example, when DFDE vessels were first ordered in the early 2000s, it takes longer time to delivery as shipyards need longer time to apply the new propulsion technology. The delivery time of DFDE
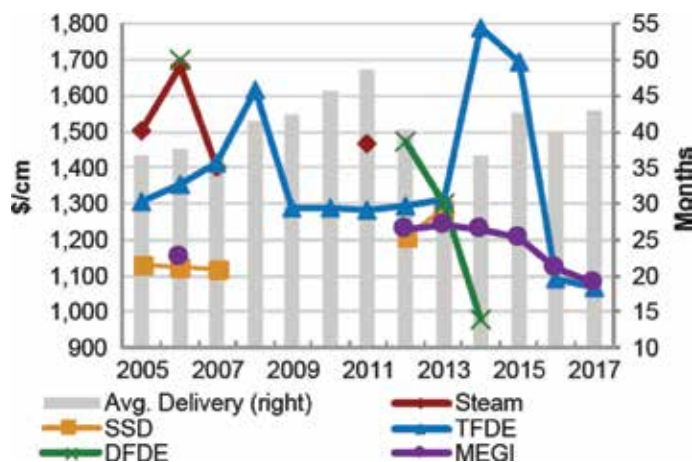

Figure 12.
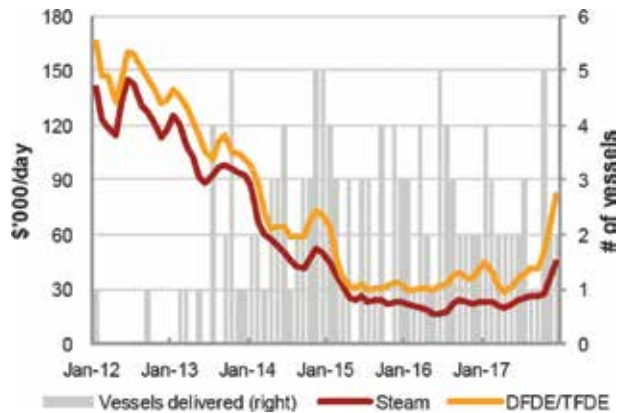*Trends of investment cost and delivery schedule [18].*

Figure 13.
Trends of LNG spot charter rates [18].

carriers between 2006 and 2010 reached an average length of 50 months, but cut down to 37 months after 2010. If a sister ship is ordered, the delivery time can be reduced to within 24 months, because few modifications are required in design.

Trends of LNG spot charter rates are illustrated in **Figure 13**. During the most of 2017, spot charter rates kept a low level, approximately $23,500/day for conventional steam carriers and $37,000/day for DFDE carriers. The gap between charter rates for conventional steam carriers and DFDE carriers has remained because the larger and more fuel-efficient carriers are more preferred by the charterers. The charter rates of vessels equipped with ME-GI and X-DF propulsion systems are even higher than that of DFDE carriers as the newer technologies can offer increased efficiency. Remarkably, toward the end of the year, there was a significant increase in the charter rates. For conventional steam carriers, the charter rates reached an average $44,300/day, while the charter rates for DFDE carriers reached an average $81,700/day.

4.2 Propulsion efficiency

The propulsion efficiency is calculated based on the thermal efficiency of the engine and the transmission efficiency of the components, as shown in **Table 3**. LSDF can achieve the efficiency nearly 50% owing to the high efficiency of 2-Stroke DF Engine and direct mechanical driving. The propulsion efficiency of UST, SSDR, DFDE and COGES has almost similar performance, ranging from 40 to 42%. The efficiency of SSD is reduced mainly due to extra power consumed by the re-lique-faction plant.

Propulsion Options	ST		DFDE		SSDR		LSDF		COGES	
Thermal efficiency of engines & transmission efficiency of components	• Fuel/BOG:	1.00	• Fuel/BOG:	1.00	• Fuel:	1.00	• Fuel/BOG:	1.00	• Fuel/BOG:	1.00
	• Boiler:	0.88	• DF engine:	0.45	• 2-Stroke Engine:	0.50	• Gas turbine(xxx):	0.48
	• Steam turbine:	0.35/	• Alternators:	0.97	• Shafting:	0.99	• 2-Stroke DF Engine	0.50/	• Alternators:	0.97
	(CST/UST)	0.41	• Converters:	0.98	• Re-liquefication		(HP/ LP):	0.49	• Converters:	0.98
	• Gearbox:	0.98	• E-Motors:	0.96	plant is		• Shafting:	0.99	• E-Motors:	0.96
	• Shafting:	0.99	• Gearbox:	0.98	considered				• Gearbox:	0.98
			• Shafting:	0.99					• Shafting:	0.99
Total efficiency	CST: 30%	UST: 35%	40%		40%		HP: 49%	LP: 48%	42%	

Table 3.
Propulsion efficiency of different propulsion options.

4.3 Emission performance

The comparison of emission performance of different propulsion system is illustrated in **Figure 14** and **Table 4**. In terms of SOx emission, SSDR and ST have higher SOx emission since they burn the HFO purely and partially, respectively. DF engine's SOx emissions are from sulfur in the pilot fuel and hence are much lower than SSDR and ST.

In term of NOx emission, SSDR and LSDF-HP have relatively higher NOx emission. DFDE, ST and COGES release lower NOx missions. GT produces approx. 2–3 times NOx in comparison to ST. COGES can comply with Tier III in both gas and MGO mode [19].

4.4 Development trends

By comparing the order book and the active fleet, as shown in **Figure 15**, we can see that the orderbook reflects a variety of new propulsion systems, including
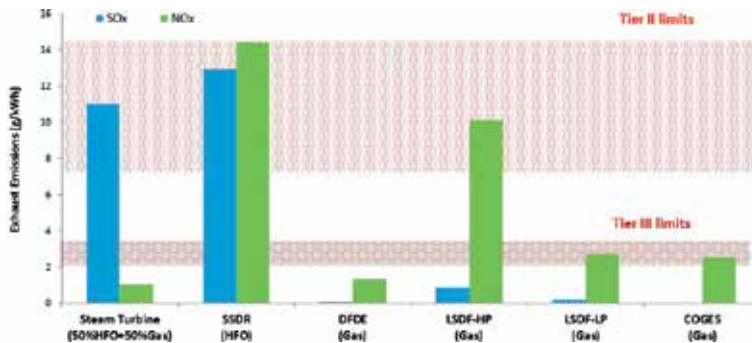
Figure 14.
Emission performance of different propulsion options.

Fuel	DFDE	ME-GI	X-DF	COGES	STaGE
LNG	IMO Tier III	IMO Tier II	IMO Tier III	IMO Tier III	IMO Tier III
MGO	IMO Tier II	IMO Tier II	IMO Tier II	IMO Tier III	IMO Tier II

Table 4.
Comparison of emission performance of different propulsion options [20].

Figure 15.
Development trends of propulsion system.

LSDF(HP), LSDF(LP), UST and STaGE. The preferred option is shifted from DFDE to slow speed dual fuel engine, LSDF accounting for 57% of the orders while DFDE accounting for 28%. MAN ME-GI high pressure engines have evolved into a popular propulsion choice. WinGD X-DF low pressure technology has been gradually gaining ground recently. Improved steam propulsion, including UST and StaGE, have entered into the commercial arena.

5. Conclusion

The economic market trends as well as global emission regulations are leading to diversified development of propulsion systems for LNG carriers.

- The UST, improved based on the conventional ST, substantially increase the thermal efficiency and emission performance (approx. 15%).

- LSDF(HP) featured with high fuel efficiency, free of knocking risk and negligible methane slip remains a popular propulsion option.

- LSDF(LP) can offer relatively less capital cost and Tier III compliance, and thus has been gaining ground recently.

- COGES can offer excellent emission performance and design & arrangement flexibility, the high capital cost, however, makes this technology being awaiting the first order.

- STaGE, as a hybrid propulsion system combining UST and DFDE and providing high reliability and improve efficiency, has entered into the commercial arena.

In conclusion, there is not a unique optimum solution for the propulsion of LNG carriers. Each option has its advantages and disadvantages that must be evaluated before the selection of the propulsion plant for a specific project. Therefore, the decision for which propulsion system to be utilized, must be examined case by case, based on the specific size of the vessel, the operating profile (speed, trade mode and distance, use of natural BOG and forced BOG or BOG and fuel oil as add-on, or fuel oil only and BOG re-liquefaction, etc.), the fuel oil and LNG price trends and the availability of bunkers of the correct grade in the operating route, the initial cost and maintenance cost, the emission regulation compliance, the crew availability and so on.

Nomenclature

ABS	American Bureau of Shipping
BOG	boil-off gas
BMEP	brake mean effective pressure
CCS	China Classification Society
COGES	combined gas turbine electric & steam system
CST	conventional steam turbine
DFDE	dual fuel (medium-speed) diesel electric propulsion
EEDI	energy efficiency design index
EGR	exhaust gas recirculation
FGSS	fuel gas supply system
GCU	gas combustion unit

GT	gas turbine
HFO	heavy fuel oil
HP	high pressure
HRSG	heat recovery steam generator
IACS	International Association of Classification Societies
IGC Code	international code for the construction and equipment of ships carrying liquefied gases in bulk
LNG	liquefied natural gas
LNGC	liquefied natural gas carrier
L_{OA}	length over all
LP	low pressure
LSDF	low speed dual fuel
MDO	marine diesel oil
MN	methane number
SCR	selective catalytic reduction
SSDR	slow speed diesel with re-liquefaction plant
ST	steam turbine
STaGE	steam turbine and gas engine
TFDE	tri-fuel diesel electric propulsion
UST	ultra steam turbine

Author details

Tu Huan*, Fan Hongjun, Lei Wei and Zhou Guoqiang
Wuhan Rules and Research Institute, China Classification Society, Wuhan, China

*Address all correspondence to: htu@ccs.org.cn

IntechOpen

References

[1] Fernández IA, Gómez MR, Gómez JR, et al. Review of propulsion systems on LNG carriers. Renewable and Sustainable Energy Reviews. 2017;**67**:1395-1411

[2] Attah EE, Bucknall R. An analysis of the energy efficiency of LNG ships powering options using the EEDI. Ocean Engineering. 2015;**110**:62-74

[3] Kosomaa J. The DF-electric LNG carrier concept. In: GASTECH. 2002

[4] MAN Diesel and Turbo. Propulsion Trends in LNG Carriers. Available from: https://www.mandieselturbo.com/docs/default-source/shopwaredocuments/propulsion-trends-in-lngb395958927f2417aa98957b04cbb684a.pdf?sfvrsn=4

[5] ABS (American Bureau of Shipping). Guide for Propulsion Systems for LNG Carriers. Houston: ABS Plaza; 2005

[6] CCS (China Classification Society). Guidelines for Design and Installation of Gas Fuelled Engines on Liquefied Gases Carriers. Beijing: China Communications Press; 2018

[7] Chang D, Rhee T, Nam K, et al. A study on availability and safety of new propulsion systems for LNG carriers. Reliability Engineering & System Safety. 2008;**93**(12):1877-1885

[8] Sinha RP, Nik WMNW. Investigation of propulsion system for large LNG ships. IOP Conference Series: Materials Science and Engineering. 2012;**36**(1):012004

[9] Class NK. Guidelines for Dual Fuel Diesel Engines. Chiba: Nippon Kaiji Kyokai; 2008

[10] Michael Wenninger and Sokrates Tolgos. LNG Carrier Power: Total Fuel Flexibility & Maintainability with 51/60DF Electric Propulsion. Augsburg, Germany: MAN Diesel SE; 2008. Available from: https://marine.mandieselturbo.com/docs/librariesprovider6/technical-papers/lng-carrier-power.pdf?sfvrsn=6

[11] LNG World Shipping. More LNG owners choose low-pressure, two-stroke engines. March/April 2018. Available from: https://www.lngworldshipping.com/news/view,lng-owners-choose-lowpressure-twostroke-engines_50482.htm

[12] Juliussen L. MAN B & W ME-GI engines recent research & results. In: ISME KOBE. 2011

[13] MAN Diesel and Turbo. LNG Carriers with ME-GI Engine and High Pressure Gas Supply System. Available from: https://marine.mandieselturbo.com/docs/librariesprovider6/technical-papers/lng-carriers-with-high-pressure-gas-supply-system.pdf?sfvrsn=16

[14] Nylund I, Alder R. The 2-stroke low-pressure dual-fuel technology: From concept to reality. In: CIMAC PAPER No. 233; CIMAC Congress; Helsinki. 2016

[15] Winterthur Gas & Diesel. Low- and High-Pressure Dual-Fuel Technology Evaluation Process. Interlaken: WinGD Low-Speed Engines Licensees Conference; 2015

[16] Marine propulsion & auxiliary machinery. Gas turbines bide their LNG carrier time. April/May 2018:33-34

[17] Hiramatsu SAI, Kuwahata K, Hirota K, et al. SAYARINGO STaGE-next generation MOSS-type LNG carrier with hybrid propulsion plant. Mitsubishi Heavy Industries Technical Review. 2016;**53**(2):3

[18] International Gas Union. 2018 World LNG Report; 2018

[19] Waney WS et al. A natural evolution of the modern LNG carriers—The application of gas turbines for LNG carrier propulsion systems. In: GASTECH. 2005

[20] General Electric Company. COGES for LNG Carrier; Shanghai: Power point provided by General Electric Company's branch; 2018

Overview of Main Electric Subsystems of Zero-Emission Vehicles

Adolfo Dannier

Abstract

The rapid growth of the electric vehicle market has stimulated the attention of power electronics and electric machine experts in order to find increasingly efficient solutions to the demands of this application. The constraints of space, weight, reliability, performance, and autonomy for the power train of the electric vehicle (EV) have increased the attention of scientific research in order to find more and more appropriate technological solutions. In this chapter, it proposes a focus on the main subsystems that make a zero-emission vehicle (ZEV), examining current features and topological configurations proposed in the literature. This analysis is preliminary to the various electric vehicle architectures proposed in the final paragraph. In particular, the electric drive represents the core of the electric vehicle propulsion. It is realized by different subsystems that have a single mission: ensure the requested power/energy based on the operating condition. Particular attention will be devoted to power subsystems, which are the fundamental elements to improving the performance of the ZEV.

Keywords: electric vehicle (EV), zero-emission vehicles (ZEV), battery electric vehicles (BEV), pure electric vehicles (PEV), vehicle to grid (V2G), electric drive, power train, energy storage system (ESS), battery management system (BMS), DC/AC converter, permanent magnet synchronous motor (PMSM), induction motor (IM), charging interface, EV architecture

1. Introduction

Until recently, electric cars were only small vehicles often designed with unusual shapes, able to move almost exclusively in the city area [1, 2]. Nowadays, electric cars are available in every size and style, often derived from the corresponding petrol models, so leading to the same internal and external fittings, load capacity, and passenger transport. Over the past few years, several legislative provisions aimed at encouraging electric mobility, pushing above all the administrations to create the boundary conditions so that the switch from a traditional vehicle to a *zero-emission vehicle* (*ZEV*) occurs with reduced discomfort [3]. Indeed, regarding the environmental impact, for assigning an optimal fuel/combustion ratio, about 85% of the combustion products in *internal combustion engines* (*ICE*) is represented by: carbon dioxide (CO_2), nontoxic but responsible for the greenhouse effect, carbon monoxide (CO), toxic and now constituting 2% of the air breathed, unburned hydrocarbons

(*HC*) and nitrogen oxides (*NOx*), toxic and responsible for acid rain. Therefore, the emissions of pollutants produced by traditional propulsion, multiplied by the number of vehicles in circulation, have a significant impact on our survival and life quality [4, 5]. As a consequence, the e-mobility role becomes crucial in the "green revolution," at least as much as that of the energy production from renewable sources. The transition to this new era of mobility is gradually increasing, passing through an intermediate phase, where there is also a fair presence of hybrid solutions that are progressively accustoming the user to the electric technology. After the transition period, the full electric propulsion will be destined to establish itself exclusively.

This revolution is accompanied by the parallel innovation in other sectors. The electric grid, for instance, is one of the fundamental elements to promote the development of electric cars; through a capillary presence of the charging stations to compensate the weak capacity of the onboard energy storage. The future is made of renewable sources and smart grids that manage power while taking into account both consumption and distributed generation, and electric cars can become a tool to strengthen efficiency and stability of the electric grid [6]. Several countries are already going down that route, with the so-called *vehicle to grid* (*V2G*) service: an innovative service, which allows electric vehicles to return energy to the grid when they are not in use, thus generating income for their owners [7]. Moreover, the spread of electric goes well with the sharing economy: electric car sharing is becoming increasingly common in all of the world's major cities.

Designing an electric car does not just mean replacing the *ICE* with an electric motor. Generally, electric car has no traditional transmission, no gear, and the engine size changes significantly (it can even be fitted in the wheels), but it needs space for the batteries, which are very heavy: the frame requires a new design; also materials change, shifting from aluminum to composite materials that are resistant but lighter, in order to increase battery capacity. The electric revolution thus opens up new opportunities regarding the areas of the design and manufacturing [8].

The *electric drive (ED)* represents the core of the electric vehicle propulsion. It is realized by different subsystems that have a single mission: to ensure the requested power/energy based on the operating condition. This chapter will show the characteristics of the individual subsystems that carry out a generic electric drive and the main architectures of electric drives suitable for *ZEVs*. Particular attention will be dedicated to state-of-the-art of the architectures and topologies employed for each power-subsystem in order to obtain the best performance on the market. This approach is fundamental to obtain an improving efficiency; nowadays, according to well-to-wheel (W2W) analysis [9], thermal engines have 17–19% efficiency scores, whereas the electric engine scores are at least equal to 36%.

2. Classification of electric vehicles

In recent years, hybrid and electric vehicles have always gained more market share [10]. These cars are equipped with an *energy storage system* (*ESS*, typically batteries), also integrating an *ICE* in the case of hybrid vehicle [11]. Despite the presence of an electric motor/generator and a battery, it is not possible to define a hybrid car a zero-emission vehicle. Therefore, before addressing the main issues of our topic, it is important to better define the different topologies of hybrid/electric cars, as briefly shown in **Figure 1**:

- *Plug-in hybrid electric vehicles (PHEVs)*: they are hybrid vehicles, that is, with double power source for propulsion, an electric and a combustion engine whose battery, normally designed for a range of a few tens of kilometers, and

can be recharged from the electric grid [12]. Once the battery is discharged or as soon as it reaches a minimum charge level (20–40% of its energy), the vehicle, according to the type of system management, enters in "normal" hybrid operation, similar to that of hybrid vehicles not rechargeable. With a battery sizing suitable for delivering a range of 30 km, it may meet to "zero emissions" most of the vehicles in the city. Several cars of this type have autonomy in electric operation even over 50 km.

- *Range-extended electric vehicles (REEVs)*: they have a plug-in battery pack and electric motor, as well as an internal combustion engine. The battery, normally sized for a range around hundred kilometers or more, can be recharged from the electric grid; once discharged, comes into action an electric generator powered by the onboard internal combustion engine which provides the battery charging [13]. The difference from a plug-in hybrid is that the electric motor always drives the wheels, with the internal combustion engine acting as a generator to recharge the battery when it is depleted. The *ICE* of a *REEV* works at an optimized regime and this allows to obtain better efficiency compared to a traditional vehicle.

- *Bimodal vehicles*: they are vehicles equipped with two completely independent engines, respectively, electric powered by a rechargeable battery from the electric grid and endothermic that can be used as an alternative to the electric
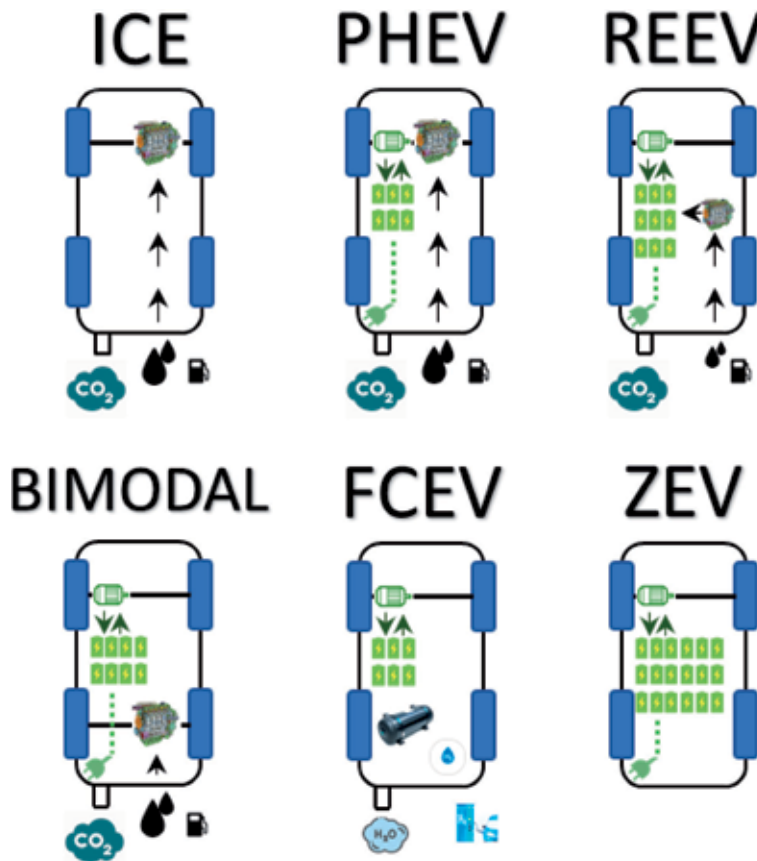

Figure 1.
Classification of the hybrid and electric vehicles.

one for long distances. Often, each of the engines is connected to an axis of the vehicle, which then operates with front or rear wheel drive depending on the activated motor.

- *Fuel cell electric vehicles (FCEVs)*: hydrogen fuel cell vehicles are a different topology of electric car and they have a fuel cell stack which uses hydrogen to produce energy that then powers the wheels of the vehicle [14]. The main difference between a fuel cell and a battery is the manner for supplying the source of energy. In the fuel cell, the production of the energy carries out thanks to hydrogen supply; in this way, it is not necessary to recharge in order to generate power. The products of the chemical reaction that occurs in a fuel cell are substantially heat and water; in particular, the latter is disposed of through the tailpipe. Differently from what happens for battery-powered vehicles, vehicles equipped with fuel cell can be recharged to appropriate filling stations in the same way as conventional vehicles. Charging times are comprised between 3 and 6 min. Typically, these vehicles have autonomy of about 500 km.

- *Zero-emission vehicles (ZEVs)*: full electric vehicles, otherwise known as *battery electric vehicles* (*BEV*) or *pure electric vehicles* (*PEV*), are wholly driven by an electric motor, powered by a battery that can be plugged to the grid [15]. There is no combustion engine.

Then, it will be evaluated and analyzed only the several solutions to realize the power train of a ZEV.

3. Basic ZEV architecture

The main elements on which ZEV architecture is built on are shown in **Figure 2**. Indeed, several subsystems can be identified and each of these performs a specific mission also interacting with one or more other subsystems. The main macroblocks identified are:

- *The energy storage system*: usually the battery pack with its management system (*battery management system* also called *BMS*), which is designed to accumulate and supply energy.

- *DC/AC converter*: it is the power interface between the storage and the electric motor. It not only has the task of adapting the power supply but it also play important control functions, as will be fully described later.

- *Motor*: the electric motor, which can also be operated as a generator in case of the adoption of the regenerative braking, has the task of carrying out the conversion of electric energy coming from the *ESS* into mechanical energy to be supplied to the mechanical transmission to allow the car motion.

- *Charging interface*: the charging interface is essential for a ZEV, as it must allow the batteries to be recharged onboard. The charging interface includes different kinds, depending on the type/types of recharge that it wants to adopt (even more types on the same vehicle).

- *Control layer*: the supervisor and data acquisition system is dedicated to processing driving information and transforming it into references for the aforementioned power subsystems.
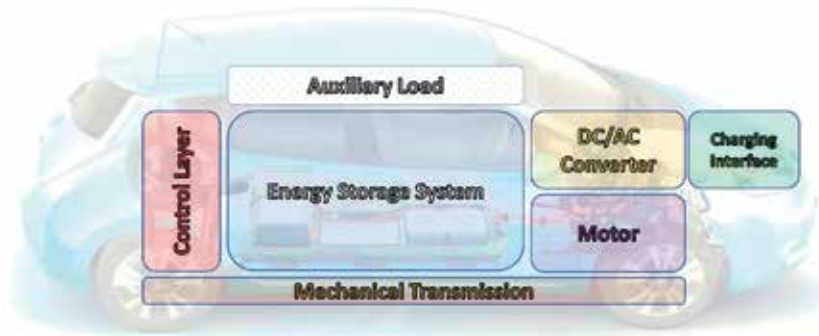
Figure 2.
Main subsystems of the basic ZEV architecture.

- *Auxiliary load*: the auxiliary loads, which will not be analyzed in this chapter, represent all the utilities onboard that need a power supply. Typically, the power of these loads occurs at a much lower voltage of the main voltage of the DC-bus, for example, 12 V, and must be galvanically insulated, for safety reasons, since this last. The power supply of the auxiliary load, therefore, is derived from the DC-bus through a DC/DC converter with electronic transformer (e.g., *flying bridge converter* or *isolated switch mode power supply*) which ensures the request insulation condition [16].

- *Mechanical transmission*: the mechanical transmission of an electric vehicle takes care of converting the energy coming from the electric motor into mechanical energy of movement, distributing it directly to the wheels of the car. This element has been borrowed from traditional vehicles and therefore has poor interest in carrying out its analysis here.

Next paragraphs are dedicated to the analysis of the technological solutions used and the technical characteristics regarding the main power subsystems of the power train previously indicated. In particular, we will provide the characteristics of the individual subsystems, identifying the performances achieved by the research in progress and their use/integration into the different proposed architectures.

4. Energy storage system

The storage system is becoming a key component in the electric vehicle. The panorama of energy storage devices can be divided into two main families: on one side *electromechanical* storage devices and on the other *electrochemical/electrostatic* devices. The first set fundamentally includes flywheels, while for the characteristics and the performances required of an electric vehicle, electrochemical systems are employed exclusively in order to guarantee the main propulsion; the classification is broader and more detailed [17], in particular, the main categories identified are:

- *Fuel cells*: it is an electrochemical system in which electric energy is produced through an oxidation–reduction chemical reaction. The storage difficulties are the main obstacle to the diffusion of systems based on hydrogen technologies, even if at the theoretical level, there are about several types of storage systems [18].

- *Electrochemical batteries*:

    1. *Lead-acid batteries*: they are commercially mature rechargeable batteries. Generally, they are made up of lead metal and lead dioxide electrodes immersed in a sulfuric acid electrolyte (in the charged state). Lead-acid batteries generally are used in stationary energy storage applications, especially as a DC auxiliary. The energy density of lead-acid batteries is 35–40 Wh/kg, whereas the power density is 250 W/kg; the cost is (battery system only) 150–200 $/kWh [19].

    2. *Nickel metal hydride batteries*: With reference to the positive electrode (cathode) of the nickel metal hydride (NiMH) batteries, it is made by nickel hydroxide ($Ni(OH)^2$). On the other hand, the anode uses the hydrogen as absorbing negative electrode. This latter is composed by metal hydrides, typically alloys of lanthanum and rare earths that work as a solid source of reduced hydrogen, which becomes oxidized to provide protons. As a rule, the electrolyte is alkaline (e.g., potassium hydroxide). These batteries have an energy density of 70–80 Wh/kg and a typical power density of 150–200 W/kg. The cost is around 400–450 $/kWh. Their main disadvantages are high self-discharge rates and a relatively low cycling capacity. Moreover, NiMH battery deteriorates during long time storage. This problem can be solved by charging and discharging the battery several times before reuse. This reconditioning also serves to overcome the problems of the "memory" effect [20].

    3. *Sodium/metal chloride batteries*: the sodium-nickel chloride battery is better known as *zero-emission battery research activities* (ZEBRA) battery. These batteries work at high temperature, about 300 °C; it is very similar to the sodium sulfur battery. The energy density of the considered battery is around 100–120 Wh/kg and the specific power is about 150 W/kg. The negative electrode is composed of molten sodium, while the positive electrode is nickel in the discharged state and nickel chloride in the charged state. The molten sodium salt is employed as electrolyte. Lately, there has been a growing attention in the sodium-nickel chloride batteries for EV application. These batteries are substantially being developed and manufactured by General Electric and Fiamm SoNick. $NaNiCl_2$ batteries have a much lower self-discharge rate and better cycling capabilities than the other nickel battery variants. Like lead-acid batteries, sodium-sulfur batteries have a limited cycle life; they are able to charge and discharge a limited number of times before significantly degrading. The cost is about 600–700 $/kWh [21].

    4. *Metal-air batteries*: metal-air batteries have a hypothetical energy density much higher than lithium-ion batteries and they are commonly sponsored as a solution toward next generation of ESS for electric vehicles or grid energy applications. This type of battery has a very high specific energy density; the reason is that these batteries are very performant because one of the reactants (the air) does not have to be stored in the battery. The metal-air battery is made by an exposed porous carbon electrode (called the air cathode) separated from the metal anode by an electrolyte. The exposed carbon electrode traps oxygen atoms from the air, which react with the positive metal ions from the anode. The scientific literature is investigating to substitute the nonaqueous electrolyte with solid, liquid, aqueous, and organic electrolytes but truth of facts demonstrate that the nonaqueous electrolyte is the most developed. The main advantage of this type of battery is the huge increase

in energy density over more conventional batteries; it is supposed that an energy density of up to 3 kWh/kg may be achievable although the actual maximum is 350 Wh/kg [22] in lab test. This is a developing technology that promises excellent results in the near future. It promises that the cost can reach 130–160 $/kW.

5. *Lithium polymer*: lithium polymer batteries use lithium metal and a transition metal intercalation oxide (MyOz) for the negative and positive electrodes, respectively. It has a specific energy of 155 Wh/kg and operates at a nominal voltage of 3 V with specific power of the 315 W/kg. A very low self-discharge rate, equal to 0.5% per month, is the main advantages together with capability of fabrication in a variety of sizes and shapes, and safe operation thanks to reduced activity of lithium with solid electrolyte. However, it has the low performance when works at a low temperature; this aspect is linked to the temperature dependence of ionic conductivity. The cost is about 200 $/kWh, a reduction to 100 $/kWh in 2025 is expected [23].

6. *Lithium ion batteries*: lithium ion batteries are now the leading type of batteries found in electric vehicles due to their high energy density, high efficiencies, and lightweight. The positive electrode is made by graphitic carbon with a layered structure, while the negative electrode in these batteries is a lithiated metal oxide. Typically, the electrolytes consist of lithium salts dissolved in organic carbonates. Lithium ion batteries are set to be the dominant battery for the electric vehicle market, and their development for this market is driving their costs down. The lithium-ion batteries are at the heart of technological development as it is currently the most promising technology. The current trend is to develop batteries in nanoscale and with vastly increased electrode surface areas. This approach provides significant improvements in terms of power, capacity, cost, materials, and sustainability. One other issue with Li-ion batteries is the lack of a viable recycling process. This is another topic of current research. There are many types of lithium-ion batteries. Those that have commercial relevance are lithium cobalt, lithium manganese, lithium nickel manganese cobalt, and lithium iron phosphate batteries. The energy density of actual L-ION batteries is 150–190 Wh/kg, whereas the power density is 500 W/kg; the cost is (battery system only) 150–200 $/kWh [24, 25].

• *Supercaps*: known as *electric double-layer capacitor* (*EDLC*); they are devices with a very high specific capacity when compared to the most common electrostatic capacitors. The electrochemical capacitor is characterized by a very similar construction to that of a battery; it has substantially two electrodes and an ion permeable separator, placed between the electrodes, which contains the electrolyte. The porous electrodes are immersed in an electrolytic solution and the area in which the charges are concentrated at the electrode/electrolyte interface is also called double-layer or "double layer." The electrochemical capacitors thus store energy in the double layer, or Helmholtz layer. The use of supercap in electric vehicles is linked to a demand for power rather than energy storage, indeed the frequent stop/go operation of EVs, the discharging/charging profile of the energy storage is vastly varied. The average power that the energy storage has to provide is very lower than the peak power; indeed, the peak power is required only for short time, for example, for fast acceleration and hill climbing. The ratio between peak power and average power can overcome 10:1. The energy involved in the acceleration and deceleration transients is roughly two-thirds of the total

amount of energy over the whole vehicle mission in urban driving. Since it is difficult to obtain at the same time an energy storage with high values of specific energy, specific power, and cycle life, a hybridization solution can be chased for EV/HEV applications. In particular, the energy storage can be fulfilled with combination of the high specific energy system together to high specific power system. The power source system can be recharged from the energy system during less demanding driving or regenerative braking [26].

In order to have a general overview, in **Figure 3**, the characteristics of the main storage technologies that can be used for the purpose are summarized.

Although there are different types of batteries, those with lithium ion dominate the most recent group of developing electric vehicles. This type of batteries, as known, has a high energy density and they have a low memory effect. Furthermore, in the technical comparison of the different systems, an element that plays a crucial role is certainly the stability of the system and the expected life both in terms of system availability over time and life cycles. The effective life of lithium-ion batteries can be carried out with two different criteria: calendar life and cycle life. The first one allows the estimation of the useful life span without considering the cyclical model of the battery. The other one, instead, allows evaluation of the number of charge/discharge cycles that the battery can undertake before its usable capacity falls below 80% of its nominal capacity [27]. Several research studies have investigated the degradation process of lithium-ion batteries, identifying the different factors contributing to it and parameterizing the de-rate according to the characteristics of battery use, such as charge/discharge cycles, discharge depth (*DOD*), state of charge (*SOC*), operating temperature, charge/discharge rate, end-of-charge voltage (*EOCV*), etc. [28]. The loss of the cell capacity depends on a nonlinear way by the retention time, with a tendency to slow down while the aging process evolves. Conversely, the reduction of the power of the cell follows a linear dependence.

Table 1 shows the characteristics of the main accumulators examined previously, with particular attention to the energy density and power density.

4.1 Battery management system

The battery represents a time-varying system with a heavy nonlinear behavior due to the complex electrochemical process and to its inherent parameters: equivalent
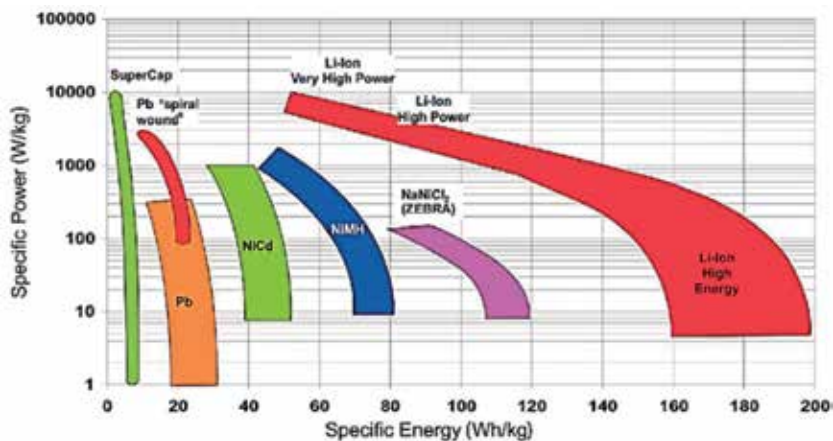

Figure 3.
Ragone diagram for the main storage technologies.

Type	Energy density (Wh/kg)	Power density (W/kg)	Efficiency (%)	Cost ($/kWh)	Cycling capacity
Fuel cell	1850[1]	—	50–55	—	—
Pb-A	35–40	250	75–90	150–200	500–2000 cycles
NiMH	70–80	150–200	72–78	400–450	1500–3000 cycles
NaNiCl$_2$	100–120	150	75–85	600–700	300–500 cycles
Metal-air	350	—	50	130–160	100–300 cycles
Lithium polymer	155	315		200	300–2000 cycles
Li-ion	150–190	500	75–90	150–200	3000 cycles at 80% D.O.D.
EDLC	5–15	up to 20.000	90–95	up to 10.000	up to 20.000.000 cycles

[1]*Hydrogen tank at 700 Bar and 10 kg of H$_2$.*

Table 1.
Energy and power density for ESS.

series resistance, open circuit voltage (OCV), and available capacity. The stable battery behavior in harsh environments represents a relevant issue regarding the safety and the utilization efficiency. Moreover, another objective is to increase the lifetime of the battery by suitably controlling the charging/discharging process. The latter means that it is recommended to avoid wide temperature excursion as well as a high frequency of charging cycles and/or deep discharging. Therefore, a *battery management system* (BMS) becomes an essential component to properly supervise the battery state [29]. The BMS represents a separate part, with its own hardware and firmware, which can usually be adapted to different battery categories by also allowing a safe battery operation. The battery state of charge (SOC) is the ratio between the available and the maximum capacity and its estimation is not very simple, because of the nonlinear nature of the battery itself. Nevertheless, a careful SOC evaluation is useful to prevent a battery fault, while also avoiding a premature aging, due to undesired undercharging/overcharging [30]. The above discussion highlights that an accurate battery model is crucial to guarantee an adequate dynamic behavior and to improve performance in terms of lifetime [31–33]. In fact, an accurate battery modeling should allow predicting the battery behavior in steady-state condition as well as during transient operation. Therefore, the main goal is to provide an accurate SOC estimation method, able to precisely track the SOC also during the charge/discharge transient operation, so that the residual vehicle autonomy is properly evaluated. In the current literature [34, 35], different approaches are proposed to model the battery behavior. The obtained models can be divided in three main categories: experimental, mathematical, and electrochemical equivalent circuit-based. The mathematical modeling is based on the evaluation of the battery voltage as a function of SOC, current and dc gain, while the equivalent circuit-based one neglects the internal electrochemical processes. The aforementioned models endorse good results in terms of accuracy and can be implemented in BMS for battery voltage prediction. Indeed, the model implementation inside the BMS is mandatory to suitably manage the energy flow both in case of charge and discharge process. Usually, in underperforming applications, one of the most used models is the simplified circuit model, which does not take into account the SOC as well as the battery dynamics: it consists of an ideal voltage source with a series resistance (i.e., internal resistance). On the other hand, an equivalent circuit, which also considers the battery dynamic behavior, consists of an OCV with voltage depending on SOC, an internal resistance and a number *n* of *RC* branches that take into account the effects of hysteresis and polarization, which occur

inside the cells [36]. The model parameters are not constant but their behaviors vary with the SOC, the temperature, the lifetime, and the history (i.e., number and depth of cycles) of the cells. In order to evaluate the model parameters, it is possible to implement several series of charge/discharge cycles, monitoring the terminal voltages and currents at controlled temperature. The evaluation of the model parameters is a difficult task, since, either at the time of manufacturing or during their operation, a slightly variation of capacity occurs. In order to minimize the effects caused by cell parameter differences, it is very important to keep the cells at the same SOC. Thus, the equalization of the cell voltage and relative capacity is mandatory. Passive and active cell balancing action allows to maintain a suitable battery SOCs by monitoring individual cells in the stack. Consequently, the battery lifetime increases [37], while also assuring an extra protection against possible damage arising from deep discharging and/or overcharging. The passive balancing acts in a simple manner by dissipating the surplus of charge in a bleed resistor, so maintaining balanced SOCs. Nevertheless, this method does not extend the system run time. On the contrary, the active balancing represents a more effective method, able to equally distribute the energy among the cells both during charge and discharge cycles. This allows an increase of the available charge in the battery stack, so resulting in higher run time, while reducing the charging time and the heat generation, with respect to passive balancing.

5. DC/AC converter

In the architecture of an EV, the presence of the DC/AC converter is fundamental both for storage management and for the operation of the electric motor. Its main goal is to promote the transfer of energy from the batteries to the engine. Compared to the first versions of electric cars, currently, the best technological solution employs as a traction motor an AC type: *permanent magnet synchronous machine* (PMSM) or alternatively an induction motor (IM), for the relative details, see next section. This choice requires the adoption of a converter that must convert from DC to AC to supply the traction motor. Torque and speed of the motors can be controlled accurately by converter's control, improving the handling of the EV and maximizing the traction effort. Variable-speed, variable-frequency operations are essential features of traction drives and, therefore, electric motors and power converters are intimately connected in terms of design and performances [38, 39]. Future electric drives can improve the present state-of-the-art with an optimization of all the subsystems. Therefore, it is evident how the topology of this converter affects all the power train of an EV. It is possible to discriminate three topological configurations for the considered converter:

1. a single-stage DC/AC converter

2. a double-stage DC/AC converter

3. an integrated DC/AC converter

Each of the previously mentioned types has advantages and disadvantages and can be implemented with different circuit topologies, extending the realization possibilities and the achievable performances.

5.1 Single-stage DC/AC converter

The direct conversion from DC to AC current can be realized with converters as H-bridge and neutral point clamped (NPC) [40, 41]. The aim is to obtain an output

AC, which appropriately performs the motor control consistent with the assigned reference, starting from DC in output from the batteries. However, given the dependence of the voltage of the battery pack from the SOC, it is appropriate to balance the operation just as the DC input voltage changes. This can be achieved by acting appropriately on the modulation index of the traction control. However, the performance of this solution might be affected by their state of charge. Therefore, compared to a simple construction, a reduction in weight and dimensions, the solution examined certainly has significant performance limitations and in any case variable with the SOC. For example, the classic diagram of a three-level NPC inverter is shown in **Figure 4** with the correspondent voltage space vectors (18 active and 1 zero-voltage vectors). Large, medium, and small voltage magnitudes are identified by subscripts "*L,*" "*M,*" and "*S*" while with "*Z*" refers to zero-voltage vectors. The complex plane can be split in six sectors each of which up into two regions (region 1, region 2), in order to accurately modulate the reference to be followed.

The most high-performance converters are those multilevel, who provide a large number of voltage space vectors. In fact, this allows to follow with a good degree of accuracy the reference imposed by the control logic. However, in multilevel converters, the problem of capacitor voltage balancing leads to limitations in selecting the converter output voltage vector, and suitable corrections are introduced in the control technique. The voltage balancing method is strongly linked to the converter topology used. In the literature, it is possible to find different solutions that propose complex algorithms based on analytical methods, coordinate transformation, pulse width (PWM), or space vector (SVM) modulation, among others [42]. The issue of balancing becomes even more critical when there is a direct connection to the storage system.

5.2 Double-stage DC/AC converter

In this case, as can be seen from the architecture shown later (**Figure 12**), the battery pack must be interfaced with the DC-bus through a DC/DC converter that can manage the flow of power both during charging (regenerative break) and during the discharge phase. The type of converter is bidirectional for the flow of energy [43, 44]. Its characteristics are closely linked to the voltage levels chosen for the DC-bus and the battery string. Typically, this is a buck-boost chopper that can also accommodate the option of interfacing with a fast and/or ultrafast charging system for charging the whole battery pack. Many topologies of this converter are proposed in the literature, borrowing the configuration by the application of steady
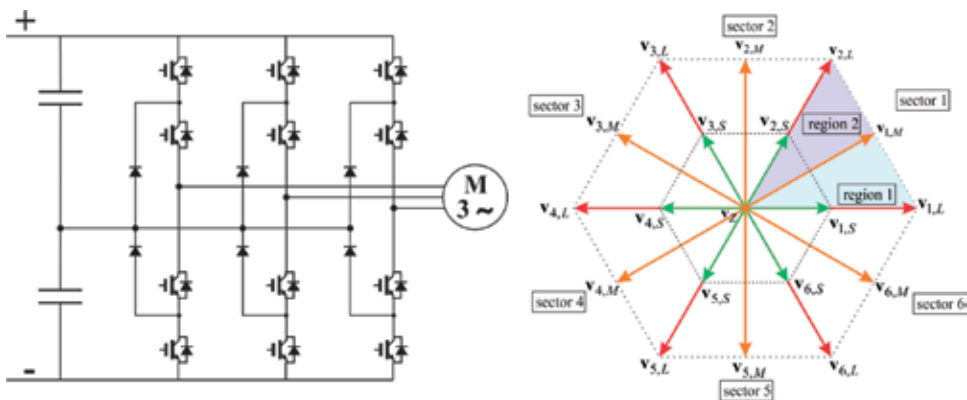

Figure 4.
Neutral point clamped topology with correspondent voltage vectors.

storage that is already established, for example, in order to highlight the differences compared to abovementioned converter, one of the double-stage topologies consists of the interleaved DC/DC chopper [45] before the NPC, as shown in **Figure 5**.

5.3 Integrated DC/AC converter

Solutions worthy of note, instead, refer to the DC/AC topologies that are trying to integrate, in a single converter, both the battery management system and the interface toward the DC-bus [46]. Indeed, as it is shown in **Figure 6**, the onboard storage systems must be managed very carefully, ensuring constant balancing, in different operation conditions, in order to preserve the declared performances for lifetime. The lifetime of the batteries is strictly dependent on the use of the batteries and the management capacity. In a traditional method, all the battery cells are connected in series/parallel to reach the desired DC-bus voltage and to obtain required energy. The charge/discharge phase is carried out with the same current but, due to the different
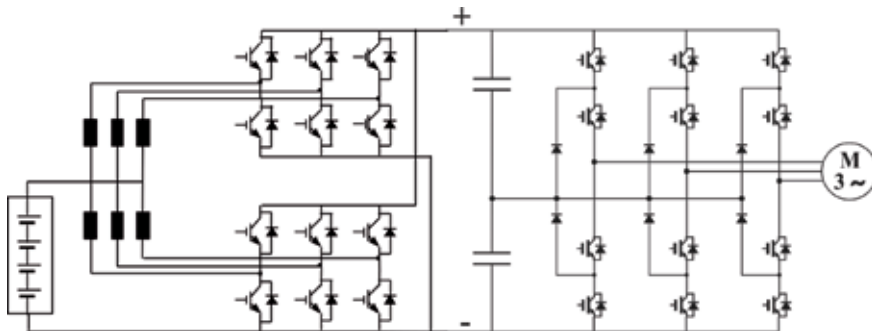
Figure 5.
Double-stage converter topology: interleaved DC/DC chopper with NPC inverter.
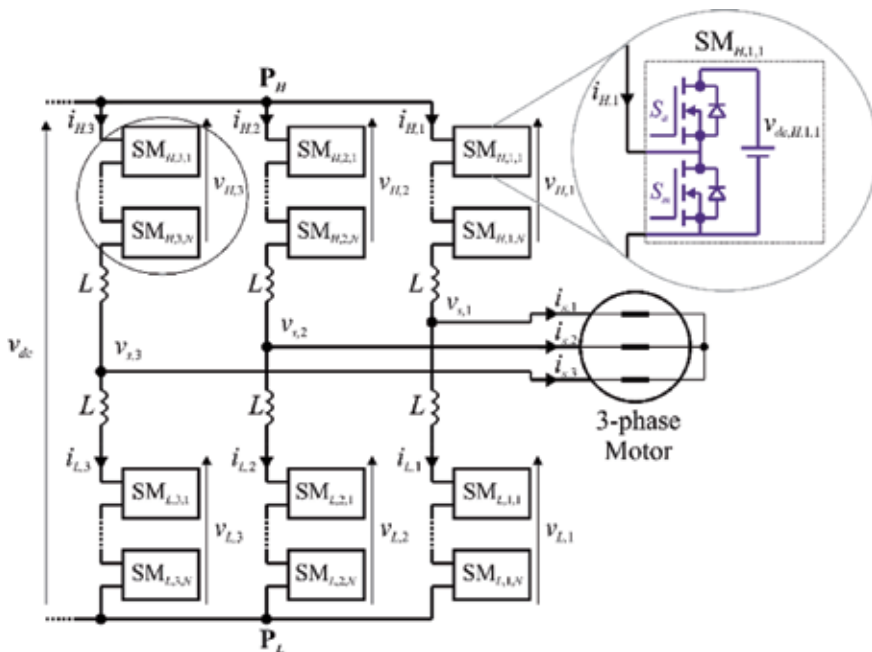
Figure 6.
Modular multilevel converters power topology.

electrochemical characteristics of the batteries, different voltages and different SOCs will be obtained for each cell. Therefore, the charge/discharge phase must be stopped as soon as even one of the cells reaches its cutoff voltage. The inequality of chemical characteristics among the cells affects load current and determines an unbalanced power contribution. Unbalancing of the cells can cause premature failure of the pack over extended cycling due to the overhanging/undercharging of cells. This aspect introduces a progressive damage of battery cells and consequently reduction of their service lifetime. For this reasons, passive or active battery management systems (BMSs), as described above, are usually added to the battery pack. The BMS has the main purpose of dynamically minimizing the imbalance of the battery pack during normal operations in order to preserve the cells' lifetime. In this traditional approach, the traction power unit is equipped with an AC converter that allows the connection with AC-motor and/or AC-grid for recharge. In some cases, it is possible to find ZEVs that host onboard another converter, which has the task of allowing the charging of the battery from the grid. More and more widespread are the solutions that integrate in one *integrated DC/AC converter* the features that individual converters offer separately. Different converter solutions have been considered to obtain high performance, especially from the point of view of the conversion efficiency. Among them, multilevel converter is one of the most accredited topologies to achieve good performance. The most promising one is definitely the modular multilevel converter (MMC), where each individual submodule (SM), in half- or full-bridge configuration, is directly fed by an elementary cell. Generally, this converter topology is used for high-voltage application, where the main advantages over conventional ones and the most significant features are: simple realization of redundancy, low device ratings, easy scalability and a possibility of common DC-bus configuration for multidrive applications, low THD of the output voltage, good fault-tolerance capability, and enhanced motor efficiency/performance in comparison with the traditional two-level voltage source inverter (VSI). The converter plays a double role: in fact, it can work as traction converter as well as a charger, which increases the power density and reduces the cost by combining the traction and charger converters. This solution allows to obtain both the BMS functionality and the power interface to AC utilities. However, this type of converter has also some drawbacks. The main disadvantage is substantially linked to the conversion efficiency: the presence of a high number of switching devices generates power losses that penalize the overall efficiency of the power train. Moreover, each cell delivers a current waveform not only dependent on the load active power request. The difference between the RMS and DC value of the current increases the losses of the battery cells [47].

6. Motor

The quick growth of road electric traction applications (i.e., zero-emission electric vehicle, hybrid electric vehicle, E-motorcycle, E-bike, aerospace taxing driving, and so on) drew the attention of the world of electric machines exposing several critical issues, so far ignored for industrial applications. This aspect is strictly related to the different needs that characterize the traction chain of a road electric vehicle. Therefore, the design of an electrical drive for such applications requires an adaptation of the external characteristics of the system, especially in terms of torque vs. speed ratio in the whole speed range. In fact, the performance of the drive system (motors + power converter) is strongly limited by the current rating of the ESS. Consequently, the effective torque output of the system is heavily reduced in low-speed range with respect to the potentially available torque by the electric motor. Actually, in order to follow the constraints that a road electrical

traction system has to satisfy, three-phase brushless/induction motors are generally used. These solutions require high-frequency switched power converters and suitable control strategy, in order to ensure dynamic performance in line with the expectations of the end user. In a conventional traction drive, the motor current limit vs. the motor speed is practically constant until the nominal motor speed. As a consequence, in order to increase the torque-speed ratio of the drive in the low speed range, two solutions are generally adopted:

1. The motor current limit is increased in the low speed range;

2. A different gear ratio is used in low-speed range.

In the first case, an oversizing of the power converter is needed. Of course, the employed converter will never be used at its full power capability, resulting in a worst cost/benefits ratio. In the second case, additional mechanics are required resulting in a worst system efficiency in the low speed range. Different solutions in order to overcome the previous limits are being investigated by the scientific world [48–50]. Such studies, although different in the substance, try to increase the torque-speed ratio of a given motor by *modifying the stator-winding configuration* of the motor in order to obtain a different behavior of the torque/speed ratio for a fixed motor current. This approach allows avoiding the oversize of the power converter and/or the need of a variable gear ratio [51, 52]. In EV automotive applications, the torque/weight ratio value for PM machines is typically less than 10 Nm/kg (Nissan Leaf 6.52 Nm/kg; Toyota Prius 7.84 Nm/kg) [53], while for induction machine, it is problematic to reach 5 Nm/kg (TeslaS).

In the last few years, the use of permanent rare earth magnets has made feasible use of *permanent magnet synchronous motors* (PMSM) in all those applications where it was customary to use direct current or induction machines [54]. One of the fundamental characteristics of the synchronous realized with permanent magnets is that of having a high specific torque; this makes them particularly suitable in EV applications where compactness, lightness, and high mechanical shaft power are requests. The permanent rare earth magnets have a high residual induction value and a high coercive field value, in addition to the possibility of being able to work at very high temperatures (up to 350°). Compared to the induction machine, the permanent magnet synchronous loses reliability due to the magnets that can be subject to demagnetization, but it has the possibility of being built with a high number of pole pairs and it works well with single-layer and concentrated-type windings, which are preferred in traction applications as they ensure a longer lifetime. With regard to the magnets, the types of rare earth magnets used are mainly two [55]:

- *Neodymium-iron-boron (NdFeB) magnets*: characterized by a high residual induction field (1.2–1.4 T), high value of the coercive field (higher than 1000 kA/m), maximum operating temperature without undergoing a strong decay of the magnetic characteristic of 150 °C;

- *Samarium-cobalt magnets (SmCo)*: characterized by a high residual induction field (1.0–1.2 T), high value of the coercive field (greater than 850 kA/m), maximum operating temperature without undergoing a strong decay of the magnetic characteristic, about 350 °C.

In view of the moldability of the rare earth magnets (they are generally made using powder metallurgy techniques), different types and geometric configurations of permanent magnet motors have been developed, see **Figure** 7.
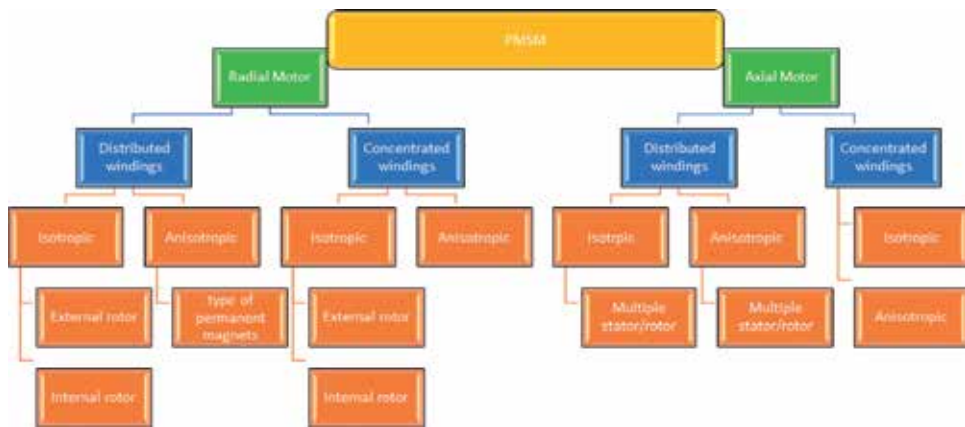
Figure 7.
Classification of permanent magnet electric motors.

As can be seen from the figure, the main classification of PMSM is made according to the direction of the magnetic flux with respect to the rotation axis: the distinction between *axial motors* and *radial motors*. In the first type of motor, the flux lines of the magnetic field to the air gap generated by the permanent magnets are parallel to the axis of the motor, while in the second case, the magnetic flux is parallel to the radial direction of the machine. Constructively, the axial flow motors have a greater radial development (they are sometimes also referred to as pancake motors), they are composed of multiple stacks (i.e., repeated parts composed of stator and rotor, or several stators and rotors assembled together) and it can be used in those applications in which the motor is thought to be integrated directly into the drive (e.g., motor wheel, or in general, for gearless applications) [56]. The axial motors are used for low-speed applications, and therefore, they are built with a high number of pole pairs (also because the high radial extension would cause problems of mechanical stress at high speeds). The radial motors are characterized by a greater axial length and they can be used both for standard applications and for special applications [57]. The two types of motors can be built with windings concentrated at the tooth or with distributed windings. For each of the types of winding, it is can think of realizing the motor with a magnetic configuration isotropic or anisotropic, that is characterized by an inductance constant magnetization in all directions or variable.

The isotropic and anisotropic motors have different magnetic and constructive characteristics, which affect their operation. The isotropic motors are made with the magnets arranged on the rotor surface (the rotor can be internal or external), and can be characterized by the use of magnets of different shapes adapted to optimize the field of magnetic induction provided by the magnets themselves. The anisotropic motor consists of magnets, partially or totally, drowned in the iron, arranged perpendicular to the radial direction or rotated by a certain angle with respect to the main machine axes; the isotropic and anisotropic motors allow to obtain high specific power density with also high torque or speed. In particular, the anisotropic motor can reach higher specific power density thanks to contribution of reluctance torque component; it is usually employed in lower speed performance when the asymmetric rotor configuration is adopted or rather, when drowned magnets are used, it is generally preferred for operation in field weakening. The main electrical faults that may affect the electrical machines are divided into three main categories:

- opening of a winding;

- short circuit between phase and ground or between phase and phase;

- short circuit at the motor terminals.

In order to minimize the occurrence of faults and their effect on mechanical performance, constructive measures are used to make the motor fault tolerant [58]. The fault tolerant characteristics of an electric machine are obtained by suitably modifying the winding [59]. Normally, in most electric machines in alternating current, a distributed multilayer winding is used, capable of generating an almost sinusoidal air gap induction field. From the constructive point of view, a multilayer winding can submit within a slot of the coil sides belonging to different phases, and therefore between the insulators of the two sides would impose a potential difference capable of creating discharges inside the insulating. Moreover, a possible short circuit that would affect a phase, besides damaging the insulator of the phase itself, could cause the failure to propagate also to the insulation of the other phase present in the same slot. To avoid this, a first fault tolerant feature is obtained by using the single-layer windings concentrated on the tooth: in this way, it is possible to avoid the overlapping of the coils of the various phases, and in each slot, there will be a single winding relative to a determined phase. The use of single-layer winding concentrated on the tooth allows to reduce the length of the heads, also bringing a considerable advantage for the machine's overall dimensions [60–63]. An innovative solution to extend the drive operating range in EV would be to use *multiphase motor* and to dynamically modify its torque-speed ratio by changing the stator-winding configuration. This approach would give also the multiphase motor advantages: *greater fault tolerance*, *smaller torque ripple*, *less phase power rating,* and so on.

6.1 Control strategy

Since many years, field-oriented control (FOC) and direct torque control (DTC) are the most popular control methodologies for AC motor drives. The FOC strategy, see **Figure 8**, is strictly dependent on the motor electrical parameters, requires long computation time and high switching frequency of the inverter. Instead, the DTC strategy (see **Figure 9**) is a more robust technique that needs very low computation time and ensures acceptable results even at low switching frequency [64]. A fast torque response can be obtained by means of DTC, due to "direct" interaction of machine electromagnetic quantities (torque and flux) and selected voltage space-vector [65]. Despite these important benefits, DTC has several drawbacks as variable switching frequency (strongly dependent on hysteresis band and motor speed) and large torque ripple in the low-speed region.

The rapid development of multilevel converters for drive systems has strongly improved DTC performance with regards to the torque ripple especially when a high number of levels are used [66]. Applying the DTC for converters with more levels, a larger number of voltage vectors can be exploited in order to better control stator flux and torque in induction motors. In this case, the identification of the proper voltage space-vector to be applied has a number of solutions increasing with the number of inverter levels, and consequently, a more complex voltage selection criterion is needed. On the contrary, the increased freedom degrees can be exploited by minimizing the switching frequency, while keeping uniform both the conduction and switching losses of the electronic devices. These methods allow to solve problems of torque ripples, difficulty to control torque at very low speed, variable switching frequency, high values of total harmonic distortion (THD) contents in
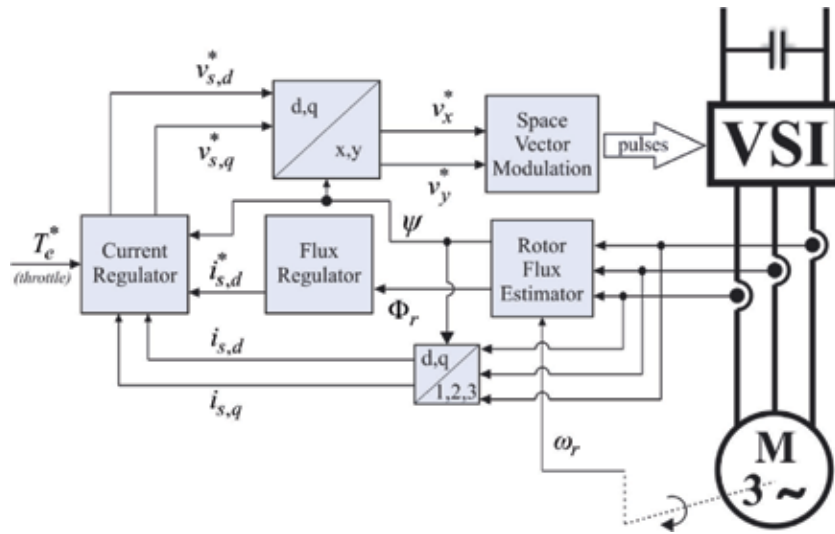
Figure 8.
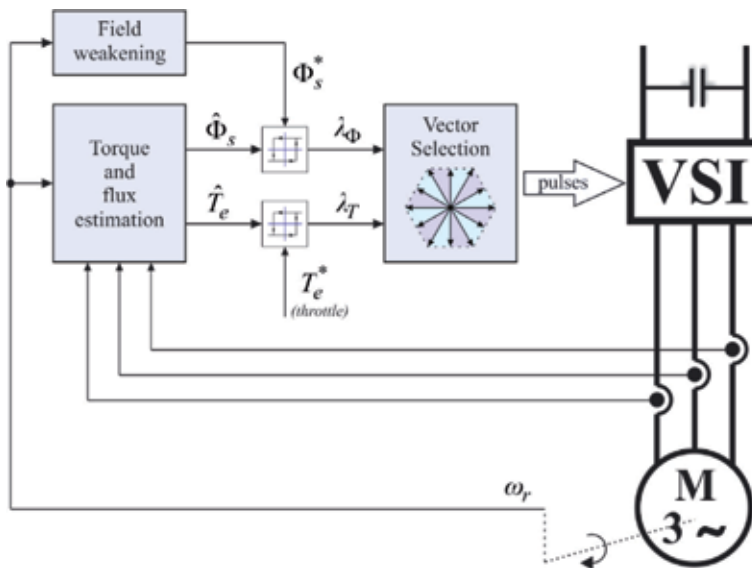*General block diagram of the field oriented control (FOC).*

Figure 9.
General block diagram of the direct torque control (DTC).

armature currents. In DTC induction drives supplied by multilevel inverters, usu-
ally not all the available converter voltage vectors are used by the selection criterion,
due to the aforementioned freedom degrees. This could negatively influence steady-
state and/or dynamic drive behavior.

7. Charging interface

The charging infrastructure is essential to "refuel" the ESS of an electric vehicle.
They are classified and configured according to the type of power supply, whether
in alternating current (AC) or in direct current (DC), of the operating power and of

the charging time, of the type of connection by cable (plug) between the fixed part (station) and moving part (vehicle) both for the power and signal part [67–69].

A first distinction between the alternating current and direct current infrastructures as well as the type of power supply is based on the position of the battery charger, i.e., the converter that manages the charge profiles required by the battery pack. The alternating ones in most cases have the battery charger onboard the vehicle. In the case of direct current charging, however, the converter is integrated into the charging station. Obviously, the management of the recharging process in the case of AC recharges is simplified compared to the DC case, because the charging infrastructure is limited to providing energy to the vehicle and to guarantee the safety requirements prescribed by the IEC 61851 standard.

In the case of DC recharges, the infrastructure is called to check the current and voltage profiles supplied to the vehicle that may vary according to the battery packs onboard. Therefore, they are exchanged during the connection of the vehicle, and during the charging phase, a whole series of information with the battery management system (BMS) onboard the vehicle. The main advantage of DC charging regards to lighten the vehicle of a conversion unit, and therefore, to reduce the weights, the overall dimensions, and the costs. Furthermore, since the external converter to the vehicle, it is easy to increase the power when charging the battery if pack so permits. The charging time is strictly dependent on the energy of the battery pack and the power of the charging station. In an electric car, a "full" of energy is of the order of 20/30 kWh and requires 20–30 min to 100 kW (80% of the SOC).

The possibility of reducing the charging time is therefore linked, on the one hand, to the increase in the maximum power of supply of the charging point, and on the other hand to the increase in the maximum charging current of the battery without reducing the useful life cycles [70, 71]. However, the excessive increase of the installed power in a charging point leads to an unjustified increase in the installation and maintenance costs of the plant as a function of the reduction in recharge time. Based on these preliminary remarks, the IEC 61851 classifies charging points accessible to the users:

- *standard power recharge point "Normal Power" (≤22 kW)*: this is a recharging point that allows the transfer of electric energy to an electric vehicle with a power rating of 22 kW or less, excluding devices with a power rating of less than or equal to 3.7 kW, which are installed in private homes or whose main purpose is not to recharge electric vehicles, and which are not accessible to the public. The standard power recharge is detailed in the following types:

  1. *slow* = equal to or less than 7.4 kW;

  2. *quick* = more than 7.4 kW and equal to or less than 22 kW;

- *high power recharge point "High Power" (> 22 kW):* this is a recharging point that allows the transfer of electric energy to an electric vehicle with a power greater than 22 kW. The high power recharge is detailed in the following types:

  1. *fast*: more than 22 kW and equal to or less than 50 kW;

  2. *ultrafast*: more than 50 kW.

The standards EN 62196-2 and EN 62196-3 define the types of connectors and the "mode" to allow the charging of the vehicle from the mentioned charging stations:

- *Mode 1*: the vehicle is connected to the AC grid with domestic connectors up to 16 A and with 30 mA differential protection type A.

- *Mode 2*: the connection of the electric vehicle to the power supply is carried out with household or industrial connectors up to 32 A, with 30 mA differential protection type A and a control test on the cable.

- *Mode 3*: the connection of the electric vehicle to the power supply is carried out with dedicated connectors, with 30 mA differential protection type A. The connection must also have a connecting cable with some extra conductors suitable for a maximum current of 250 A or a cable compatible with the Mode 2 suitable for a maximum current of 32 A.

- *Mode 4*: it is a direct current (DC) connection for fast recharging. Practically, the connection of the electric vehicle to the power supply is made via an external charger to the vehicle. Control and protection functions and the vehicle charging cable are installed always in the charging station.

The sockets and plugs, for charging electric vehicles in AC, are defined and regulated by IEC 62196-2, while accessories for DC charging are regulated by the IEC 62196-3 standard.

In particular, the standard defines the following types for AC charging:

- *Type 1*: single-phase plug socket with two pilot contacts. Maximum current up to 32 A, maximum voltage 250 V, and IPXXB protection degree.

- *Type 2*: single-phase or three-phase plug socket up to 63 A 500 V. Required degree of protection IPXXB with interlocking requirement to avoid disconnection under load.

- *Type 3A*: *for light vehicles*: single-phase plug socket up to 16 A 250 V. Required degree of protection IPXXD. This standard requires that the plug can be disconnected under load.

- *Type 3C: for all vehicles*: both three-phase and single-phase plug socket with two pilot contacts up to 63 A 500 V and IPXXD protection degree with the option of disconnecting the plug even under load up to 32 A.

With reference to the four types of charging, the standard IEC 62196-2 specifies four types of electrical connectors:

i. *Type 1—SAE J1772-2009 (Yazaki)*: it is a single-phase connector with two power contacts + PE and two pilot contacts for the control, max 32 A 230 V (7.4 kW), is adopted by Japanese and American vehicles. The specifications of the connector, referred to by the previous standard. The connector is equipped with mechanical interlock.

ii. *Type 2—VDE-AR-E 2623-2-2 (Mennekes)*: it is a single/three-phase connector, with two pilot contacts for control, max 32 A—7.4 kW (63 A—43.5 kW), 230/400 V, is adopted on European vehicles. Initially, there was no mechanical interlocking that was introduced only from 2012.

iii. *Type 3A—EV Plug Alliance (Scame)*: single-phase, two power contacts + PE and one pilot contact for the control, max 16A, 230 V, is used only for light vehicles (scooters and quadricycles) and refills up to 3.7 kW.

iv. *Type 3C—EV Plug Alliance (Scame)*: single/three-phase, two/three power contacts + PE and two pilot contacts for control, max 32A—230/400 V, 7.4 kW/21 kW, it is scarcely widespread.

For direct current charging, the standard defines two types of connectors:

• *CHAdeMO*: it's connector for DC charging with additional pins for communication with the vehicle;

• *Combo combined charging system (CCS)*: it's connector for DC charging that integrates also the Type 2 AC inside to allow both AC and DC charge through a single connector;

The CHAdeMO standard is the standard for fast charging in direct current (DC) [72]. This standard is adopted for Nissan, Mitsubishi, Peugeot, Citroen vehicles. Vehicles equipped with this standard have two connectors:

• CHAdeMO for fast DC charging

• Connector for AC charging (normally Type 1)

Its specifications are defined by the Japan Automobile Research Institute (JARI) G105-1993 standard and use a CAN-BUS communication protocol. With reference to the combined charging system (CCS), however, it provides a unique charging connector on the electric vehicle, which allows both the fast charge current (DC) and the slow charging alternating current (AC). The CCS is made from Type 2 connector, so the system is called Combo2. This system is now adopted by some European car manufacturers (for example, BMW and Volkswagen). **Figure 10** shows the previously defined connectors.

With reference to the previous power classification, the "normal power" charging systems must be equipped with a Type 2 socket compliant with the IEC 62196-2 standard for each charging point dedicated to passenger cars and four-wheel commercial vehicles; a socket type 3A conforms to the IEC 62196-2 standard for each charging point dedicated to mopeds, motorcycles, and quads. The "high-power" charging systems, on the other hand, must be equipped with at least one connector of the CCS Combo 2 type and of the CHAdeMO type, according to the IEC 62196-3 standard for direct current charging; and finally, a charging connector/socket with standard Type 2, according to the IEC 62196-2 standard, for charging in alternating current. Finally, the charging systems must be connected to a control system that allows carrying out at least the following functions in real time:

• verification of correct operation (availability);

• verification of the employment status;

• user recognition;

• enabling/inhibition of the charge;

• reading of the electrical parameters during charging.

In conclusion, it is possible to synthesize the main characteristics of the different charging points in **Table 2**.
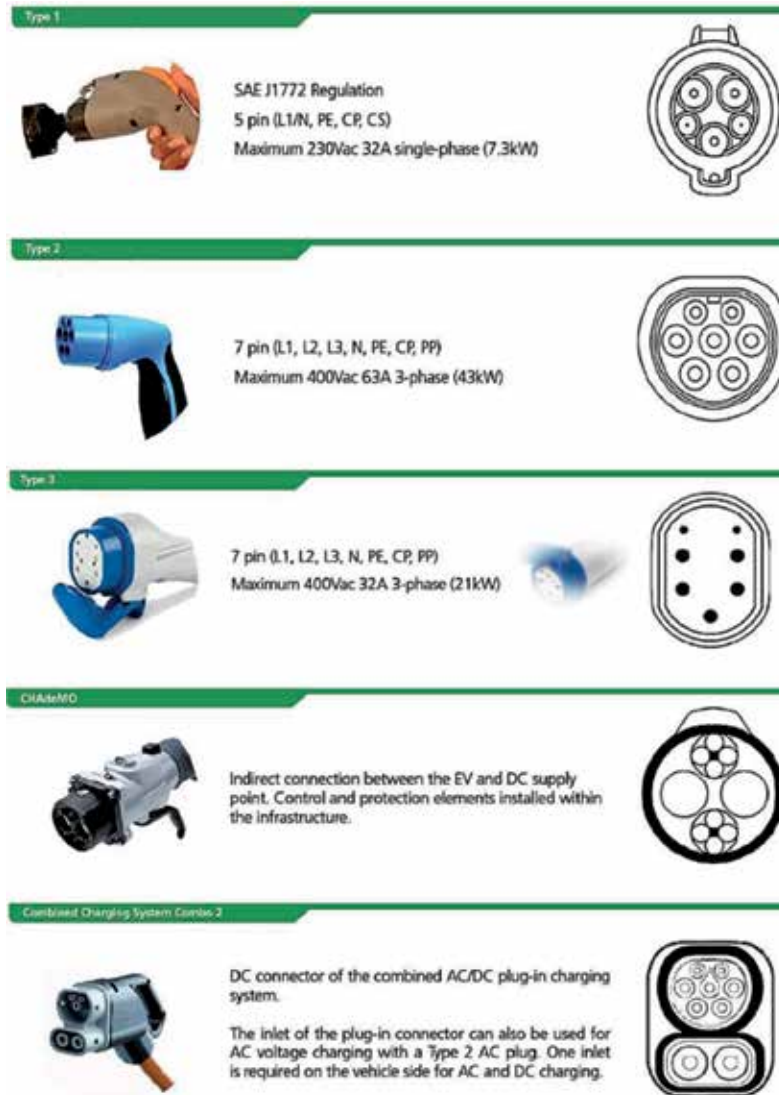
Figure 10.
Standard connectors for AC and DC charging.

Classification	Normal power (slow)	Normal power (quick)	High power (fast)	High power (ultrafast)
Categories	1	2	3	4
Supply	Single-phase AC	Single-phase or three-phase AC	three-phase AC	DC
Power	<3.7 kW	3.7–22 kW	>22 kW	>50 kW
Charging time	>6 h	1–3 h	20–60 min	20–30 min
Connector	Type 1	Type 2/Type 3	Type 2/Type 3	ChadeMO Combo
Standard communication protocol	—	IEC 81851-1 PWM	IEC 81851-1 PWM	Digital communication

Table 2.
Main characteristics of the different charging points.

However, charging via a physical connection to a charging station is not the only possibility that can be used to supply the ESS. In fact, the research is very hot to allow an inductive or wireless charging [73, 74]. The latter allows to recharge an electric vehicle without connecting it to the charging station via cables, but by exploiting the magnetic field for transferring power from a transmitter toward a receiver coil. This solution currently involves high manufacturing costs, and therefore, not to make it competitive on the market.

8. State of art ZEV architectures

Based on the considerations made previously, it is possible to identify different architectures for a ZEV. Each of the proposed architectures differs, substantially,
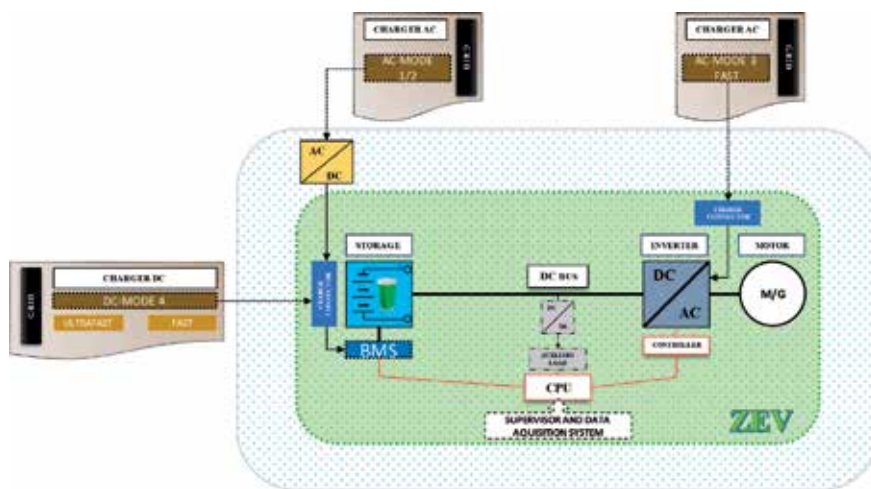

Figure 11.
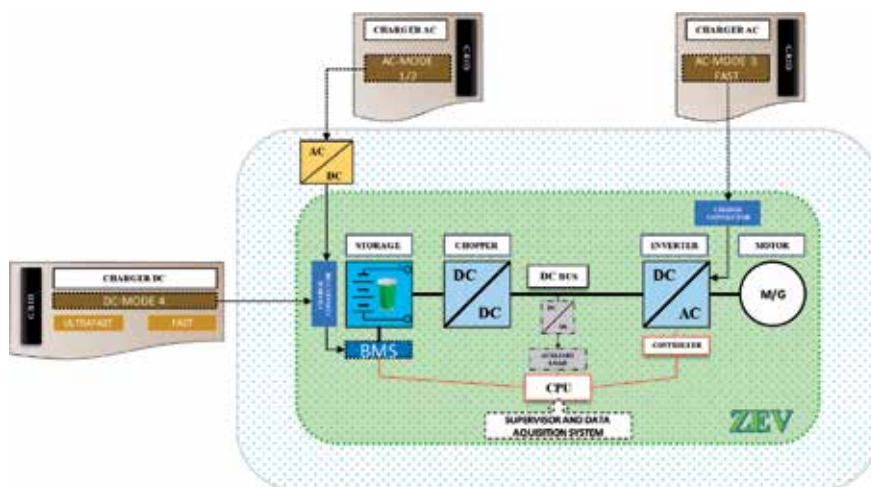*Electric drive architecture for ZEV: single-stage converter/single motor.*

Figure 12.
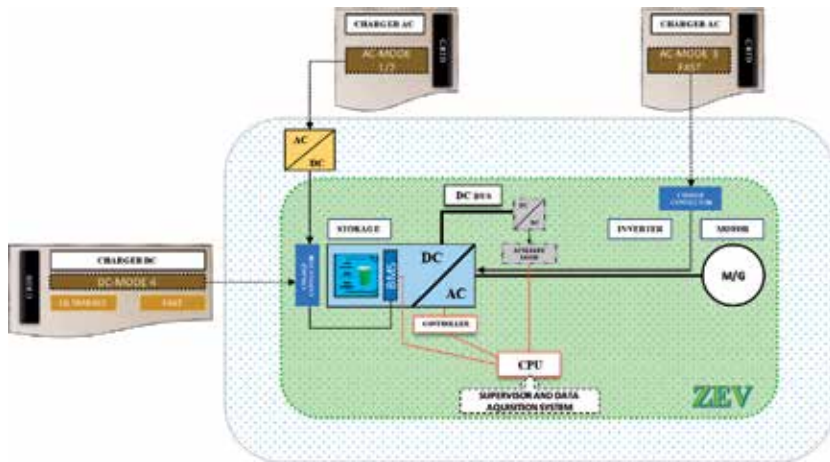*Electric drive architecture for ZEV: double-stage converter/single motor.*

Figure 13.
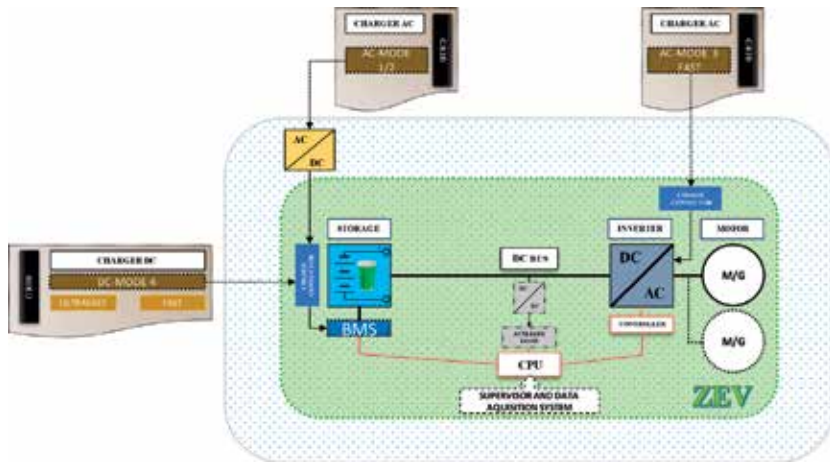*Electric drive architecture for ZEV: integrate converter/single motor.*

Figure 14.
Electric drive architecture for ZEV: single-stage converter/multiple motor.
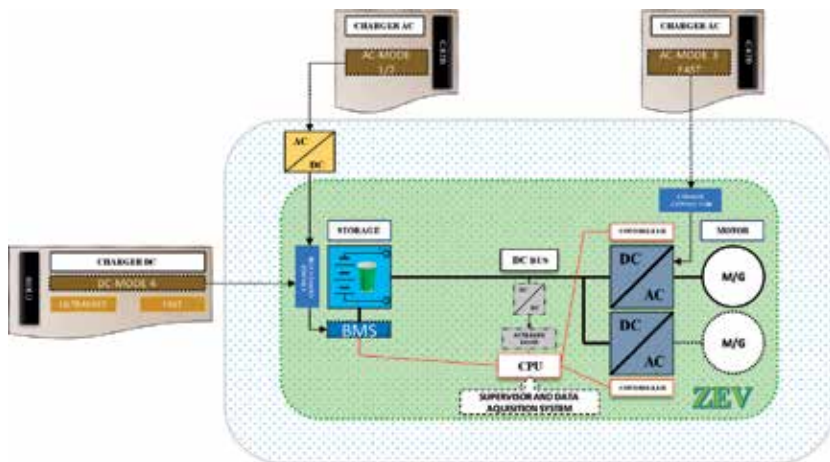

Figure 15.
Electric drive architecture for ZEV: multiple-stage converter/multiple motor.

by the choice of the DC/AC conversion stage and by the number of motors that constitute the electric drive. In each of the proposed configurations, the adoption of any of the charging modes was assumed. It is clear that every embodiment may implement one or more of the charging modes indicated. **Figure 11** shows the configuration with a single-stage converter and a single electric motor for traction. By replacing the previously described double-stage solution to the DC/AC converter, the architecture shown in **Figure 12** can be obtained. An innovative solution, on the other hand, can be achieved by using a DC/AC converter that interfaces directly with the batteries; in this case, the converter can also perform the BMS function, managing the charge and discharge of the battery pack, see **Figure 13**.

Alongside the proposed solutions, it is possible to derive new configurations depending on the use of several traction motors. The presence of multiple motors determines a change once again in the AC side converter. In this case, it is possible to adopt "dual motor" solutions where only one converter is used to supply two motors or solutions where each converter supplies its motor, see **Figures 14** and **15**.

9. Conclusions

In this chapter, it has been presented the main subsystems that making up the electric drives for a ZEV. In particular, analyzing each of one, it is evident that there are different solutions to carry out the assigned task in the whole system. Matching all possible alternatives for the realization of each subsystem, different architectures for the power train are obtained. In each of the architectures, the substantial difference is linked to the DC/AC converter, thanks to which it is possible to transfer energy from and/or toward the battery pack. Indeed, the identified configurations differ precisely in function of the choice of the latter: single-stage, double-stage, or integrated DC/AC converters generate the respective solutions examined. A further difference is related to employ one or more traction motors coupled with one or more inverters to produce the respective last two configurations.

Author details

Adolfo Dannier
Department of Electrical Engineering and Information Technologies,
University of Naples, Napoli, Italy

*Address all correspondence to: adolfo.dannier@unina.it

IntechOpen

References

[1] Rajashekara K. History of electric vehicles in general motors. IEEE Transactions on Industry Applications. 1994;**30**(4):897-904

[2] Chan CC. The rise & fall of electric vehicles in 1828-1930: Lessons learned [scanning our past]. Proceedings of the IEEE. 2013;**101**(1):206-212

[3] Explaining Road Transport Emissions, European Environment Agency. ISBN: 978-92-9213-723-6, ORDER ID (Catalogue Number): TH-04-16-016-EN-N

[4] Energy, Transport and Environment Indicators - 2014 edition, Product Code: KS-DK-14-001, ISBN: 978-92-79-41256-1, ISSN: 2363-2372, the Eurostat website at http://ec.europa.eu/eurostat

[5] Lorf C, Martínez-Botas RF, Howey DA, Lytton L, Cussons B. Comparative analysis of the energy consumption and CO_2 emissions of 40 electric plug-in hybrid electric hybrid electric and internal combustion engine vehicles. Transportation Research Part D: Transport and Environment. 2013;**23**:12-19

[6] Khan A, Memon S, Sattar TP. Analyzing integrated renewable energy and smart-grid systems to improve voltage quality and harmonic distortion losses at electric-vehicle charging stations. IEEE Access. 2018;**6**:26404-26415

[7] Monteiro V, Pinto JG, Afonso JL. Operation modes for the electric vehicle in smart grids and smart homes: Present and proposed modes. IEEE Transactions on Vehicular Technology. 2016;**65**(3):1007-1020

[8] Saju C, Lydia M. A comprehensive review on hybrid electic vehicles: Power train configurations, modelling approaches, control techniques. In: 2018 Second International Conference on Inventive Communication and Computational Technologies (ICICCT), Coimbatore. 2018. pp. 925-930

[9] Karimi H, Ansari J, Gholami A, Kazemi A. A comprehensive well to wheel analysis of plug-in vehicles and renewable energy resources from cost an emission viewpoints. In: 2014 Smart Grid Conference (SGC), Tehran. 2014. pp. 1-6

[10] Global EV OUTLOOK 2018 – IEA WEBSTORE: https://webstore.iea.org/

[11] Chan CC. The state of the art of electric, hybrid, and fuel cell vehicles. Proceedings of the IEEE. 2007;**95**(4):704-718

[12] Millner A, Judson N, Ren B, Johnson E, Ross W. Enhanced plug-in hybrid electric vehicles. In: 2010 IEEE Conference on Innovative Technologies for an Efficient and Reliable Electricity Supply, Waltham, MA. 2010. pp. 333-340

[13] Liu D, Wang Y, Zhou X, Lv Z. Extended range electric vehicle control strategy design and muti-objective optimization by genetic algorithm. In: 2013 Chinese Automation Congress, Changsha. 2013. pp. 11-16

[14] Bauman J, Kazerani M. A comparative study of fuel-cell-battery, fuel-cell-ultracapacitor, and fuel-cell-battery-ultracapacitor vehicles. IEEE Transactions on Vehicular Technology. 2008;**57**(2):760-769

[15] Yong JY, Ramachandaramurthy VK, Tan KM, Mithulananthan N. A review on the state-of-the-art technologies of electric vehicle, its impacts and prospects. Renewable and Sustainable Energy Reviews. 2015;**49**:365-385. ISSN 1364-0321

[16] Gallo CA, Tofoli FL, Correa Pinto JA. Two-stage isolated switch-mode power supply with high efficiency and high input power factor. IEEE Transactions on Industrial Electronics. 2010;**57**(11):3754-3766

[17] Gerssen-Gondelach SJ, Faaij APC. Performance of batteries for electric vehicles on short and longer term. Journal of Power Sources. 2012;**212**:111-129. ISSN 0378-7753

[18] Guaitolini SVM, Yahyaoui I, Fardin JF, Encarnação LF, Tadeo F. A review of fuel cell and energy cogeneration technologies. In: 2018 9th International Renewable Energy Congress (IREC), Hammamet. 2018. pp. 1-6

[19] May GJ, Davidson A, Monahov B. Lead batteries for utility energy storage: A review. Journal of Energy Storage. 2018;**15**:145-157. ISSN 2352-152X

[20] Fotouhi A, Auger DJ, Propp K, Longo S. Electric vehicle battery parameter identification and SOC observability analysis: NiMH and Li-S case studies. IET Power Electronics. 2017;**10**(11):1289-1297

[21] TM O'Sullivan, CM Bingham, RE Clark. Zebra battery technologies for all electric smart car. In: International Symposium on Power Electronics, Electrical Drives, Automation and Motion, 2006. SPEEDAM 2006, Taormina; 2006. pp. 243-249

[22] Kraytsberg A, Ein-Eli Y. Review on Li-air batteries—Opportunities, limitations and perspective. Journal of Power Sources. 2011;**196**(3):886-893. ISSN 0378-7753

[23] Scrosati B, Croce F, Panero S. Progress in lithium polymer battery R&D. Journal of Power Sources. 2001;**100**(1-2):93-100. ISSN 0378-7753

[24] Silva FA. Lithium-ion batteries: Fundamentals and applications [Book News]. IEEE Industrial Electronics Magazine. 2016;**10**(1):58-59

[25] Divya KC, Østergaard J. Battery energy storage technology for power systems—An overview. Electric Power Systems Research. 2009;**79**(4):511-520. ISSN 0378-7796

[26] Kouchachvili L, Yaïci W, Entchev E. Hybrid battery/supercapacitor energy storage system for the electric vehicles. Journal of Power Sources. 2018;**374**: 237-248. ISSN 0378-7753

[27] Farzin H, Fotuhi-Firuzabad M, Moeini-Aghtaie M. A practical scheme to involve degradation cost of lithium-ion batteries in vehicle-to-grid applications. IEEE Transactions on Sustainable Energy. 2016;7(4):1730-1738

[28] Millner A. Modeling lithium Ion battery degradation in electric vehicles. In: 2010 IEEE Conference on Innovative Technologies for an Efficient and Reliable Electricity Supply, Waltham, MA. 2010. pp. 349-356

[29] Lu L, Han X, Li J, Hua J, Ouyang M. A review on the key issues for lithium-ion battery management in electric vehicles. Journal of Power Sources. 2013;**226**:272-288. ISSN 0378-7753

[30] Cheng KWE, Divakar BP, Wu H, Ding K, Ho HF. Battery-management system (BMS) and SOC development for electrical vehicles. IEEE Transactions on Vehicular Technology. 2011;**60**(1):76-88

[31] Peterson SB, Apt J, Whitacre JF. Lithium-ion battery cell degradation resulting from realistic vehicle and vehicle-to-grid utilization. Journal of Power Sources. 2010;**195**(8):2385-2392

[32] Majeau-Bettez G, Hawkins TR, Strømman AH. Life cycle environmental assessment of lithium-ion and nickel metal hydride batteries for plug-in

hybrid and battery electric vehicles. Environmental Science and Technology. 2011;**45**(10):4548-4554

[33] Ager-Wick Ellingsen L, Majeau-Bettez G, Singh B, Kumar Srivastava A, Ole Valøen L, Strømman AH. Life cycle assessment of a lithium-ion battery vehicle pack. Journal of Industrial Ecology. 2014;**18**(1):113-124

[34] Hussein AA, Batarseh I. An overview of generic battery models. In: Power and Energy Society General Meeting, 2011. IEEE; 2011. pp. 1-6

[35] Tremblay O, Dessaint L. Experimental validation of a battery dynamic model for EV applications. World Vehicle Journal. 2009;**3**. ISSN 2032-6653

[36] Dannier A, Ferraro L, Miceli R, Piegari L, Rizzo R. Numerical and experimental validation of a LiFePO battery model at steady state and transient operations. In: 2013 Eighth International Conference and Exhibition on Ecological Vehicles and Renewable Energies (EVER), Monte Carlo. 2013. pp. 1-6

[37] Daowd M, Omar N, Van Den Bossche P, Van Mierlo J. Passive and active battery balancing comparison based on MATLAB simulation. In: 2011 IEEE Vehicle Power and Propulsion Conference, Chicago, IL. 2011. pp. 1-7

[38] Rind SJ, Ren Y, Hu Y, Wang J, Jiang L. Configurations and control of traction motors for electric vehicles: A review. Chinese Journal of Electrical Engineering. 2017;**3**(3):1-17

[39] Çağatay Bayindir K, Gözüküçük MA, Teke A. A comprehensive overview of hybrid electric vehicle: Powertrain configurations, powertrain control techniques and electronic control units. Energy Conversion and Management. 2011;**52**(2):1305-1313

[40] Brando G, Dannier A, Del Pizzo A, Rizzo R. A generalized modulation technique for multilevel converters. In: 2007 International Conference on Power Engineering, Energy and Electrical Drives, Setubal, Portugal. 2007. pp. 624-629

[41] Brando G, Dannier A, Del Pizzo A. An optimized control of PWM-rectifiers with predicted variable duty-cycles. In: 2008 IEEE International Symposium on Industrial Electronics. Cambridge; 2008. pp. 68-73

[42] Brando G, Dannier A, Del Pizzo A, Rizzo R. Power quality problems in unbalanced operations of fault tolerant H-bridge multilevel active front-ends. In: 2007 9th International Conference on Electrical Power Quality and Utilisation, Barcelona. 2007. pp. 1-6

[43] Karimi R, Koeneke T, Kaczorowski D, Werner T, Mertens A. Low voltage and high power DC-AC inverter topologies for electric vehicles. In: 2013 IEEE Energy Conversion Congress and Exposition, Denver, CO. 2013. pp. 2805-2812

[44] Chen CH, Cheng MY. Design and implementation of a high-performance bidirectional DC/AC converter for advanced EVs/HEVs. IEE Proceedings - Electric Power Applications. 2006;**153**(1):140-148

[45] Dannier A, Guerriero P, Coppola M, Brando G. Interleaved converter for fast charge of battery system. In: 2018 International Symposium on Power Electronics, Electrical Drives, Automation and Motion (SPEEDAM), Amalfi. 2018. pp. 425-430

[46] Brando G, Dannier A, Spina I, Tricoli P. Integrated BMS-MMC balancing technique highlighted by a novel space-vector based approach for BEVs application. Energies. 2017;**10**(10). art. no. 1628

[47] Dannier A, Brando G, Spina I, Iannuzzi D. Battery Losses In a MMC for BEVS Application. The Open Electrical & Electronic Engineering Journal. 2018;**12**:98-109

[48] Miller JM, Ostovic V. Pole phase modulated toroidal winding for an induction machine. U.S. Patent 5977679, Nov 2, 1999

[49] Gautam A, Ojo JO. Variable speed multiphase induction machine using pole phase modulation principle. In: IECON 2012 - 38th Annual Conference on IEEE Industrial Electronics Society. pp. 3659-3665

[50] Sun D, Ge B, Bi D. Winding design for pole-phase modulation of induction machines. In: 2010 IEEE Energy Conversion Congress and Exposition (ECCE). pp. 278-283

[51] Edelson JS, Cox IW, Magdych JS. The Chorus Meshcon solution for starter-generators Electric Machines and Drives. In: IEEE International Conference on IEMDC. 2005. pp. 1720-1724

[52] Miller JM, Stefanovic V, Ostovic V, Kelly J. Design considerations for an automotive integrated starter-generator with pole-phase modulation. In: Conference Record of the 2001 IEEE Thirty-Sixth lAS Annual Meeting. Vol. 4. pp. 2366-2373

[53] Hayes JG, Davis K. Simplified electric vehicle power-train model for range and energy consumption based on EPA coast-down parameters and test validation by argonne national lab data on the Nissan Leaf. In: 2014 IEEE Transportation Elec-trification Conference and Expo (ITEC). IEEE; 2014

[54] Yang Y, Castano SM, Yang R, Kasprzak M, Bilgin B, Sathyan A, et al. Design and comparison of interior permanent magnet motor topologies for traction applications. IEEE Transactions on Transportation Electrification. 2017;**3**(1):86-97

[55] https://www.stanfordmagnets.com/samarium-cobalt-magnet-motor-vs-ndfeb-magnet-motor.html

[56] Profumo F, Zheng Z, Tenconi A. Axial flux machines drives: A new viable solution for electric cars. IEEE Transactions on Industrial Electronics. 1997;**44**(1):39-45

[57] Sitapati K, Krishnan R. Performance comparisons of radial and axial field, permanent-magnet, brushless machines. IEEE Transactions on Industry Applications. 2001;**37**(5):1219-1226

[58] Mecrow BC, Jack AG, Haylock JA, Coles J. Fault-tolerant permanent magnet machine drives. IEE Proceedings Power Applications. 1996;**143**(6)

[59] Tong C, Wu F, Zheng P, Sui Y, Cheng L. Analysis and design of a fault-tolerant six-phase permanent-magnet synchronous machine for electric vehicles. In: 2014 17th International Conference on Electrical Machines and Systems (ICEMS), Hangzhou. 2014. pp. 1629-1632

[60] Dajaku G, Gerling D. A novel tooth concentrated winding with low space harmonic contents. In: 2013 International Electric Machines & Drives Conference, Chicago, IL. 2013. pp. 755-760

[61] Dajaku G, Xie W, Gerling D. Reduction of low space harmonics for the fractional slot concentrated windings using a novel stator design. IEEE Transactions on Magnetics. 2014;**50**(5):1-12

[62] Dajaku G, Hofmann H, Hetemi F, Dajaku X, Xie W, Gerling D. Comparison of two different IPM traction machines with concentrated winding. IEEE

Transactions on Industrial Electronics. 2016;**63**(7):4137-4149

[63] Le Besnerais J et al. Analysis of noise reduction in a low speed and high torque PMSM with tooth concentrated windings. In: 2016 Eleventh International Conference on Ecological Vehicles and Renewable Energies (EVER), Monte Carlo. 2016. pp. 1-6

[64] Abassi M, Khlaief A, Saadaoui O, Chaari A, Boussak M. Performance analysis of FOC and DTC for PMSM drives using SVPWM technique. In: 2015 16th International Conference on Sciences and Techniques of Automatic Control and Computer Engineering (STA), Monastir. 2015. pp. 228-233

[65] Martins CA, Roboam X, Meynard TA, Carvalho AS. Switching frequency imposition and ripple reduction in DTC drives by using a multilevel converter. IEEE Transactions on Power Electronics. 2002;**17**(2):286-297

[66] Brando G, Dannier A, Del Pizzo A, Rizzo R, Spina I. Torque derivative control in induction motor drives supplied by multilevel inverters. IET Power Electronics. 2016;**9**(11):2249-2261

[67] Shareef H, Islam MM, Mohamed A. A review of the stage-of-the-art charging technologies, placement methodologies, and impacts of electric vehicles. Renewable and Sustainable Energy Reviews. 2016;**64**:403-420

[68] Veneri O. Technologies and Applications for Smart Charging of Electric and Plug-in Hybrid Vehicles. Springer; 2016. pp. 1-307. DOI: 10.1007/978-3-319-43651-7

[69] Rubino L, Capasso C, Veneri O. Review on plug-in electric vehicle charging architectures integrated with distributed energy sources for sustainable mobility. Applied Energy. 2017;**207**:438-464

[70] Vasiladiotis M, Bahrani B, Burger N, Rufer A. Modular converter architecture for medium voltage ultra fast EV charging stations: Dual half-bridge-based isolation stage. In: 2014 International Power Electronics Conference, IPEC-Hiroshima - ECCE Asia 2014, art. no. 6869766. pp. 1386-1393

[71] Tsirinomeny M, Hõimoja H, Rufer A, Dziechciaruk G, Vezzini A. Optimizing EV driving-recharge time ratio a under limited grid connection, 7th IET International Conference on Power Electronics, Machines and Drives (PEMD 2014), Manchester. 2014. pp. 1-6

[72] Jampeethong P, Khomfoi S. An EV quick charger based on CHAdeMO standard with grid-support function. In: 2015 18th International Conference on Electrical Machines and Systems (ICEMS), Pattaya. 2015. pp. 531-536

[73] Madawala UK, Thrimawithana DJ. A bidirectional inductive power interface for electric vehicles in V2G systems. IEEE Transactions on Industrial Electronics. 2011;**58**(10):4789-4796

[74] Li S, Mi CC. Wireless power transfer for electric vehicle applications. IEEE Journal of Emerging and Selected Topics in Power Electronics. 2015;**3**(1):4-17

Chapter 3

Wetland Monitoring Using Unmanned Aerial Vehicles with Electrical Distributed Propulsion Systems

Esteban Valencia, Víctor Alulema and Darío Rodríguez

Abstract

The inspection of wetlands in the Ecuadorian highlands has gained importance due to the environmental issues linked to the growth of human activities and the expansion of the agricultural and livestock frontiers. In this sense, unmanned aerial vehicles (UAVs) have been amply used in monitoring activities such as the supervision of threatened ecosystems, where cyclic measurements and high-resolution imagery are needed. However, the harsh operating conditions in the Andean highlands and sensitive ecosystem restrictions demand efficient propulsion configurations with low environmental impact. Electrical distributed propulsion (EDP) systems have surged as a forefront alternative since they offer benefits in both the propulsive and aerodynamic performance of fixed-wing UAVs. In this chapter, an EDP system is sized for a design point at the Andean operating conditions. Thereafter, two propulsion configurations were established based on off-the-shelf components, and their performance was characterized through analytical approaches. These results highlight the trends in power consumption and performance when the number of propulsors is increased. A significant contribution of this work is to exhibit important patterns in the performance of electric propulsion by using commercial components, and to set the operating limitations that can be further explored for analogous configurations in larger UAVs.

Keywords: unmanned aerial vehicles, distributed propulsion, electrical propulsion, blended wing body, wetland monitoring

1. Introduction

The Andean region, which comprises paramos[1] [1] and wetlands, is considered a biodiversity hotspot that contains about one-sixth of earth's plant life [2, 3]. This extension of land is of great importance, since it represents the main water reservoir for major cities in Colombia, Ecuador, and Peru [4, 5]. Both wetlands and paramos

---

[1] A paramo is a Neotropical high mountain biome with a vegetation composed mainly of giant rosette plants, shrubs, and grasses.

are endangered ecosystems, and, hence, efficient and suitable monitoring solutions are urgently needed. In this way, different monitoring techniques including satellite imagery and the use of high-resolution cameras mounted on manned airplanes have been utilized. Nonetheless, the aforesaid methods are not commonly affordable because they are costly and require long setup times.

The advent of unmanned aerial vehicles (UAVs) has encouraged periodical and low-cost management of threatened ecosystems through real-time data acquisition. The incursion of aerial platforms into forestry remote sensing [6] has had a positive impact thanks to the usage of high-resolution sensors [7, 8] to gather data regarding flora health, species inventory, or mapping in a periodic way. In this respect, multicopters have been seen as the first option for monitoring; however, their low autonomy limits the area covered per flight. Conversely, fixed-wing UAVs have been introduced to overfly larger areas. The imagery provided by these tools has been collected using different payloads, ranging from basic RGB cameras to sophisticated radars. Nevertheless, the time employed for a specific mission profile is higher when operating at the Andean highlands because of the harsh atmospheric conditions, which constrain the UAV autonomy and performance.

Commercial UAVs usually perform under sea level conditions with low wind gusts (lower than 16 m/s) and higher air density. This denotes that an improvement in some UAV subsystems is required to tailor them for high-altitude monitoring applications [9, 10]. Among the different characteristics that need to be upgraded to enhance the UAV performance, the following can be summarized: robust flight control system able to withstand the strong wind gusts (18 m/s), aerodynamic and high volumetric fuselage to store the avionics and payload, and high-efficient and eco-friendly propulsion system, which reduces energy consumption. The two latter options are linked, and, thus, their implementation into the conceptual design requires the assessment of their suitability to explore synergies for a more efficient UAV configuration.

The purpose of the present chapter is to investigate the performance of an electric-powered blended wing body (BWB)[2] UAV deployed on the aforesaid ecosystems. This baseline configuration has been selected based on previous research [11], where it has been found that BWB configurations offer high volumetric efficiency while providing good aerodynamic performance [12] as a result of the elliptical lift distribution improvement over the whole airframe [13–15]. Furthermore, the BWB model facilitates the integration of different propulsion architectures, which results in a broader spectrum of configurations for distributed propulsion [16].

Regarding the power source, the electric option has been seen attractive because of the reduction of polluting gas emissions, moderate cost, lighter weight, and high reliability. In the next section, a deeper explanation about the propulsion configuration for this conceptual design is described.

2. UAV design methodology

2.1 Distributed electric propulsion

Reconnaissance and surveillance of endangered environments through overflight missions require short setup time, versatility, and noise mitigation. In this sense, electric propulsion has emerged as a reliable and potential solution to

---

[2] A BWB is a tailless aircraft design that integrates the fuselage and the wings through blended cross sections in a single body.

accomplish the aforesaid requirements thanks to its high-efficiency, moderate cost, and eco-friendly essence. Nonetheless, the capacity of commercial batteries remains to be an issue because of their lower energy density compared with their counterpart, the fossil fuels [17, 18].

The distributed propulsion is a revolutionary technology that seeks to reduce the noise and weight of an aircraft by means of replacing large propulsors with a moderate amount of small ones along the airframe [16] as depicted in **Figure 1**. This offers the possibility of increasing the propulsive efficiency because a larger propulsive area is considered, which in turn, implies a lower jet velocity. Its application on small fixed-wing UAVs has not been formally studied[3] [19], and, consequently, the present chapter aims to assess the performance of small UAV configurations with electric distributed propulsion. The study will focus mainly on power consumption and performance improvements to demonstrate the feasibility of employing this technology in small UAVs. Propulsive efficiency has not been considered as a figure of merit in the present study, because of the low operating speeds and the electrical propulsion system, where the use of this parameter does not capture well the improvement in the aircraft performance, as it does for turbofan engines.

It is important to note that distributed propulsion may offer other numerous benefits such as the elimination of the aircraft control surfaces (thrust vectoring), flexible maintenance, decrease in noise, and reduction in aircraft weight through inlet-wing integration [20]. The study of these advantages is beyond the scope of the present work, since this chapter is aimed at setting the basic conceptual configurations and assessing their suitability for the case study. Nonetheless, these various features will be implemented in further research, where the selected conceptual configurations will be assessed using a more holistic perspective.

For the assessment of suitable UAV configurations for wetland monitoring, parametric sizing and aerodynamic assessment approaches were implemented into the conceptual design stage. Then, a brief insight about the influence of electric distributed propulsion into the performance of the UAV configuration using a semiempirical approach is exposed. In the next sections, initial sizing and modelling of the UAV systems are further explained.

2.2 Initial sizing

The design procedure starts by defining the mission requirements such as flight altitude, velocities, and payload sensors. In this sense, a precise study of wetlands and paramos demands the usage of special sensors applied in monitoring activities such as crop scouting, precision agriculture, surveillance, and air quality
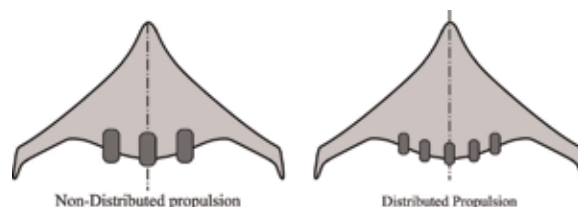

Figure 1.
Difference between distributed and non-distributed propulsion in a BWB.

---

[3] Distributed propulsion configurations have been explored by hobbyists using mainly empirical assessments.

Main camera	Mass [g]	Resolution [MP]
Logitech C510	225	8
Canon PowerShot S60	230	5
Kodak Professional DCS Pro Back	770	16
Sony DSC-R1	929	10.3

Table 1.
Monitoring sensors applied for wetlands and forestry [21–25].

monitoring. Some sensors used in these monitoring tasks are listed in **Table 1**. In this work, the payload's weight was assumed to be 1 kg for practical purposes

Next, the UAV layout is carried out, and main aircraft characteristics such as preliminary weight (W_{TOp}), wing planform area (S), and preliminary power required (P_{Rp}) are delineated through the constraint analysis technique [26, 27]. This method consists of a matching plot that allows defining the design space of the aircraft depending on their performance requirements such as stall speed, maximum speed, takeoff run, and ceiling altitude [28]. The outcomes of this design stage represent the general characteristics of a preliminary aircraft architecture and will be employed to size other parts.

Afterwards, the wing shape is outlined by defining its geometrical parameters and sectional airfoils [26, 29]. The wing geometry was set according to technical and semiempirical correlations [18], and then, the obtained results were contrasted with corresponding data of commercial UAVs with similar characteristics [6]. In this way, the aerodynamic assessment was accomplished through the employment of the open-source Athena Vortex Lattice (AVL) software which incorporates the vortex lattice method (VLM) [30]. On the other hand, due to the lack of suitable analytical methods to calculate the weight of small UAV configurations, the preliminary weight was estimated as a function of the internal volume and the structural material's density of the aircraft [26].

At the end of this stage, the external shape of a conceptual model is obtained. Thereafter, it is necessary to define a proper propulsion system through the match of the thrust required and the thrust available. Finally, the weight of the resulting architecture is assessed through a refined model that takes into account the propulsion system and the power source weight. **Figure 2** depicts the road map of the methodology employed to generate and characterize a conceptual BWB UAV model. It is worth to mention that all the symbols utilized along the chapter are reported in the nomenclature section at the end.

2.3 Propulsion modeling

The main function of aircraft propulsion systems is to generate enough thrust to overcome the drag and maintain a steady flight. For this work, firstly, suitable propellers were selected based on operating conditions and performance requirements of the UAV model. Then, the rest of propulsion elements (motor, electronic speed control and battery) was outlined based on propeller's characteristics. Finally, the established propulsion set is evaluated to verify that both the power and the thrust available satisfy the requirements for cruise condition. It is important to mention that, at this conceptual stage, the distortion and momentum drag reduction of the incoming flow to the propeller has not been considered and will be studied in future work.

The propellers are commonly characterized by the thrust (C_T) and power (C_P) coefficients through semiempirical models at early stages of design [31]. For this
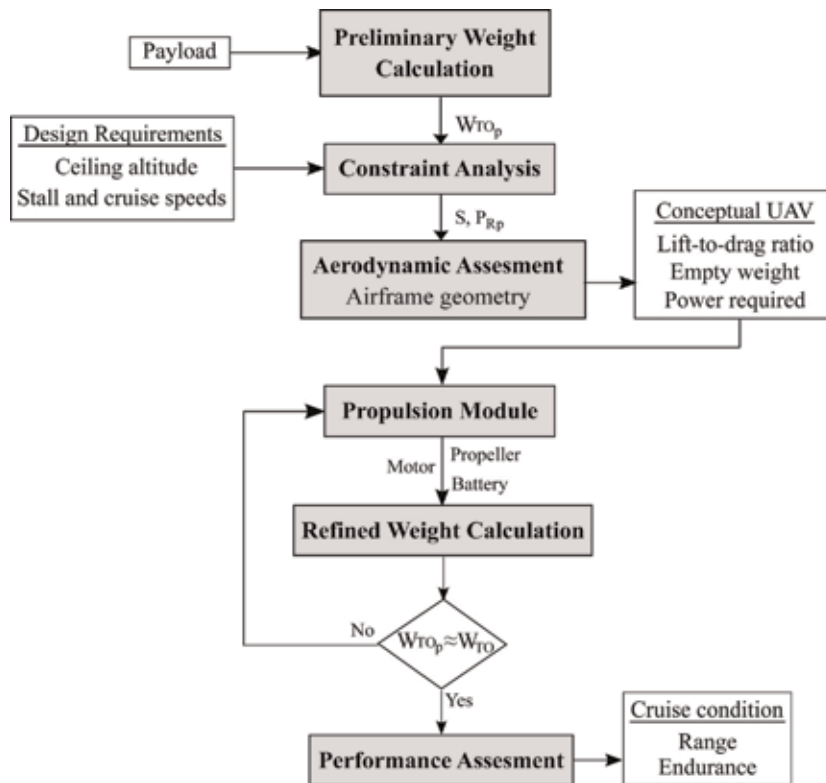
Figure 2.
General methodology of initial aircraft sizing.

study, the aforesaid parameters were obtained from an experimental database of low Reynolds propellers [32] by using the advance ratio (J) as the key driver for the selection routine. This latter parameter relates the freestream velocity, the propeller diameter (ϕ_{prop}), and its rotational speed (ω). For this work, the freestream velocity was set according to the desired cruise speed. In this way, the proposed method involves an iterative scheme that consists of estimating the thrust and power generated by a preselected propeller through the variation of ϕ_{prop} and ω for the desired freestream velocity (V_c). The iterative loop stops when the thrust and power required are met by a certain configuration. Finally, these results were used to select appropriate electric motors and batteries which can adapt well to the design requirements. This semiempirical scheme was preferred since most of the available techniques [34, 35] are focused on large propeller assessment and, hence, they present limitations for their implementation into small aerial platforms.

Brushless electric motors are commonly employed for small UAVs considering their simple design, potential to downsize, little maintenance, and independent performance of the flight altitude. In addition, their purely inductive nature and their outrunner configuration (rotor with magnets that surrounds the fixed coils of the stator) enable them to generate high torque at a low rotational speed, eliminating the need of a gearbox and facilitating their integration and test at early stages of UAV design [18, 36]. In this context, appropriate motors were outlined based solely on basic parameters provided by manufacturers like rotational speed and torque. The selected motor must be able to generate the torque required by the propeller for its adequate functioning at a certain rotational speed [37]. Once a motor has been

selected, various operating parameters like no-load current, voltage constant, and internal resistance, together with torque and rotational speed that were taken from the datasheets, were employed to estimate the required voltage (U_m) and current (I_m) of the motor [36].

The motor current (I_m) is then employed to select a proper electronic speed control (ESC) device and a lithium-polymer (LiPo) battery. It is important to highlight that batteries for small UAVs are almost exclusively lithium-based because they offer high capacity, low weight, and high discharge rates [38]. For the battery selection, two different scenarios were explored in this work. The first consisted of defining a nominal battery capacity based on commercial off-the-shelf devices to estimate the flight endurance. The second scenario aims to determine a suitable battery by giving a target endurance. This latter approach was employed to assess the maximum endurance that could be achieved by the UAV, without the constraints of off-the-shelf electronic components. **Figure 3** illustrates the road map to establish the electric propulsion system during the conceptual design stage.

Once the propulsion system and the aircraft external shape have been framed, it is necessary to estimate the UAV total weight in a more refined and accurate way. This value is then contrasted with the admissible weight stated in the design requirements. Since typical procedures are focused on civil aviation, their application cannot be extended to small aerial platforms. Instead, this work proposes a method that individually accounts for the airframe, propulsion system, battery, and payload weights and then adds each contribution to obtain the total weight as stated in Eq. (1).

The structural weight of the airframe was calculated with respect to the fuselage internal volume and the material's density. The former was estimated through the convex hull method [39], and high-density foam was assumed as the major airframe material [26]. The weight of remaining components from Eq. (1) was readily obtained from manufacturer's datasheets.

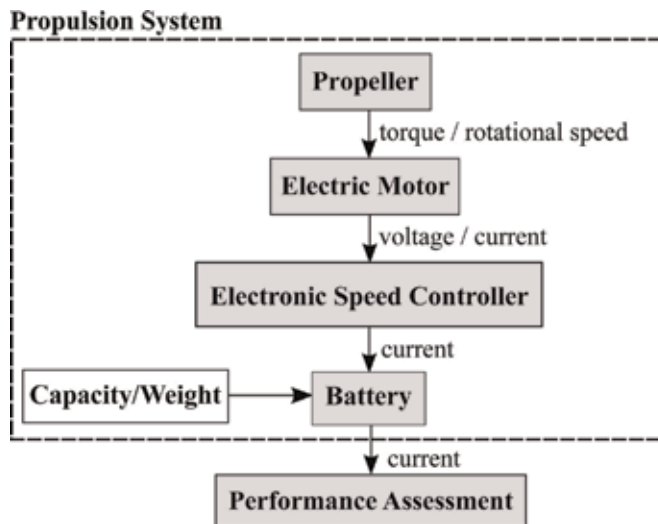$$W_{TO} = W_{airframe} + W_{propulsion} + W_{payload} + W_{battery} [\text{N}] \qquad (1)$$

Figure 3.
Electric propulsion definition and performance assessment methodology.

2.4 Performance evaluation

The performance analysis is an engineering discipline that relies on inputs from aerodynamic and propulsion assessments. In this sense, the performance evaluation aims to verify if a propulsion set (battery, motor and propeller) meets the mission requirements such as endurance and range. For this purpose, both the power required (P_R) and the power available (P_A) are determined. The former depends of the weight and the aerodynamic efficiency of an aircraft, while P_A depends on the propulsion system and its power source [35].

The power required (P_R) is calculated by means of Eq. (2) [34, 35], where ρ_{alt} is the air density at a desired altitude, S is the planform wing area, W_{TO} is the takeoff gross weight, and C_D and C_L are the drag and lift aerodynamic coefficients. Note that W_{TO} and S were previously defined in the initial sizing phase through the constraint analysis and the aerodynamic coefficients were estimated through the employment of the AVL software and parametric characterization [40]. This term represents the power required for steady cruise condition. However, the target power available (P_A) must be greater than P_R to consider a more demanding flight condition such as the takeoff phase. This excess of power is linked to the rate of climb (RC) as Eq. (3) shows [35]:

$$P_R = \sqrt{\frac{2}{\rho_{alt} \cdot S}} \left(W_{TO}^{3/2}\right) \left(\frac{C_D}{C_L^{3/2}}\right) [W] \tag{2}$$

$$P_A = P_R + RC \cdot W_{TO} \ [W] \tag{3}$$

The power available (P_A), which depends of the propeller, motor, and battery characteristics, was estimated through analytical relationships regarding non-dimensional coefficients (C_T, C_P, and J) [35]. The computed value of P_A was verified to be greater or equal to P_R in order to guarantee that the aircraft reaches the absolute ceiling altitude[4] at the desired rate of climb as explained before. Note that P_R will be less for the cruise condition because the airplane is not climbing anymore and, thus, the excess of power is zero. Finally, for the distributed propulsion case, the total power available is estimated by multiplying the number of propellers by their generated power, respectively.

It is important to highlight that the battery must provide a greater power than P_A to account for energy losses as shown in Eq. (4), where η_{prop} represents the propeller efficiency, η_e is the efficiency of the electric set (motor, electronic speed driver and battery), and P_{bat} is the power supplied by the battery:

$$P_A = \eta_{prop} \eta_e P_{bat} \ [W] \tag{4}$$

The endurance and range are the key performance parameters because they reflect the time and distance that the aircraft is able to fly without recharging. Their estimation for electric-powered airplanes through analytical models has not received special attention because the devices for the efficient energy storage are still under development and research. Nevertheless, few authors have introduced distinct and elaborated methods to predict the aforesaid parameters from aerodynamic characteristics and battery working conditions [38, 41].

For this case, a simplified but good enough approach has been employed to estimate the endurance and range [36]. This method assumes that the voltage

---

[4] This term is referred to the absolute maximum altitude that the aircraft can ever maintain level flight, i.e., the RC is zero [26].

remains constant and the battery capacity is decreased linearly. In this sense, Eq. (5) was used to calculate the endurance at cruise condition, where C_{min} represents the battery minimum capacity that can be reached in a safety margin and I_b is the battery current. The former was supposed to be 20% of the total battery capacity because lithium-based batteries can be damaged if discharged more than 80% [42]. On the other hand, I_b is a function of the motor current, avionics current, and internal resistance. Its calculation is further explained in Ref. [36], and, hence, it will not be addressed in this work. The numeric value (0.06) in Eq. (5) represents a unit conversion factor because the capacity of batteries is commonly given in milliamperes-hour, I_b in amperes, and the computed time is given in minutes. It is important to highlight that only a single battery device was considered and its number of cells was determined based on the voltage required by the motor. The range was calculated, by using the cruise speed the endurance through the assumption of a rectilinear displacement:

$$E = 0.06 \left(\frac{C_b - C_{min}}{I_b} \right) [\text{min}] \tag{5}$$

3. Results and discussion

In this section, the methodology previously explained is implemented to set the propulsion configurations for wetland monitoring at the Andean highlands. The obtained results from the UAV conceptual design, aerodynamic assessment, electric propulsion evaluation, and performance analysis are presented.

3.1 Case study

The case study was carried out for wetlands located between 3500 and 4500 masl in the Antisana volcano region from Ecuador. **Table 2** enlists some of the key operating conditions and design requirements that the aerial platform needs to fulfill in order to ensure a successful performance. Both cruise and stall speeds were set to ensure good-quality data gathering [43]. The payload mass was set not to exceed 1 kg after making a brief survey of common sensors (**Table 1**) that UAVs employ for forest monitoring [6]. These data will serve to determine the starting design point by means of the constraint analysis. It is important to mention that the maximum speed was set to be 1.25 times the cruise speed [26].

Parameter	Lower bound	Upper bound
Cruise speed [m/s]	18	22
Maximum speed [m/s]	22	26
Stall speed [m/s]	10	15
Absolute ceiling [m]	3500	4500
Aspect ratio[*]	4.5	5.5
Payload mass [kg]	1	1

The aspect ratio (AR) is defined as the ratio between the wing span and its mean aerodynamic chord [33].

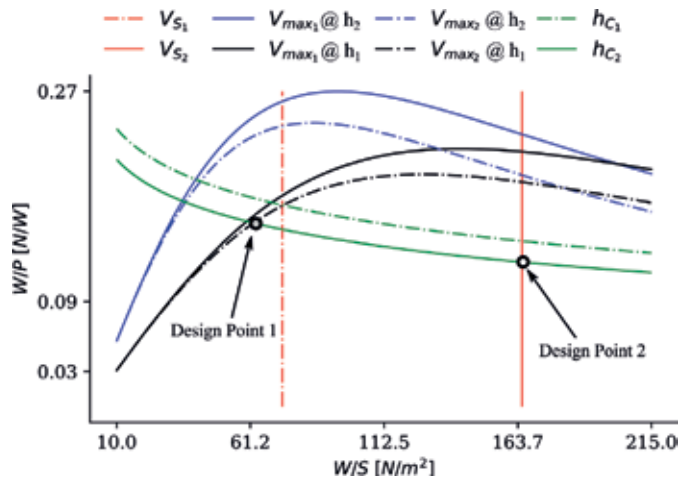**Table 2.**
Operating conditions and design requirements.

Figure 4.
Constraint analysis to determine multiple design points.

3.2 Conceptual model

The constraint analysis illustrated in **Figure 4** shows the variation of the weight-to-power ratio (W/P) with respect to the wing loading (W/S) for various performance parameters such as the maximum speed (V_{max}), stall speed (V_s), and ceiling altitude (h_c) [26, 28]. The intersection of these curves enables to define an acceptable region of design and hence, establish a starting point for the aircraft initial sizing. It is worth to mention that for a propeller-driven aircraft, the acceptable region is located below the set of the aforesaid curves. A higher relation W/P is beneficial because this yields the smallest electric motor in terms of power required [26]; however, this is limited by the stall speed for each case. For this work, as the maximum velocity (V_{max}) function depends on the air density, a curve for each flight altitude analyzed (**Table 2**) was drawn. Thus, a total of four plots were sketched, involving two values of V_{max} at two different flight altitudes (h_c).

Two design points were defined within a permissible range of wing loading for small UAVs [27, 44] while maintaining a weight-to-power ratio as high as possible. The W/S range was established by considering the strong linkage between the structural and aerodynamic behavior of the airplane. These design points will allow to investigate the variation of wing planform area and propulsion power for different design requirements and operating conditions (**Table 2**) to contrast distinct scenarios. Note that the propulsion power computed through the constraint analysis (**Table 3**) is a preliminary estimate. A more accurate value is calculated once the geometrical parameters and the aerodynamic coefficients are defined.

Afterwards, the entire airframe (wing and fuselage) was outlined through classical methods of fixed-wing aircraft design [26]. Major geometrical parameters were obtained with respect to the preliminary weight (W_{TOp}) and wing planform area (S), previously computed in the constraint analysis. Moreover, non-dimensional parameters such as wing aspect ratio (AR) and taper ratio[5] (λ) were initially established with regard to similar UAV architectures [12] and permissible ranges for this application [26]. The airfoil selected was the NACA 64A210 because

---

[5] The taper ratio (λ) is defined as the ration between the tip chord and the root chord of a wing.

Parameter	Design point 1 case A	Design point 2 case B
Wing loading [N/m^2]	87.97	165.37
Power loading [N/W]	0.145	0.141
Reference area [m^2]	0.52	0.19
Wingspan [m]	1.60	0.99
Aspect ratio	4.96	5.22
Preliminary W_{TO} [N]	33	20
Preliminary power required [W]	224	244

Table 3.
Initial sizing parameters obtained from the constraint analysis.

it has proven to be suitable for small BWB models [45]. No twist angle was considered for this study. Main parameters from the initial sizing stage are summarized in **Table 3**.

The geometrical parameters from **Table 3** were employed to generate a three-dimensional shape of the proposed airframes as depicted in **Figure 5**. This resulted in two different models whose primary difference is the size.

3.3 Aerodynamic assessment

The aerodynamic coefficients from both design concepts were estimated using the AVL open-source software. For this aim, these coefficients were obtained regarding the variation of the attack (α), that is the angle between the freestream velocity vector and the flight path as shown in **Figure 6**.

The drag polar obtained from the aerodynamic assessment of both conceptual UAV models (**Table 3** and **Figure 5**) is depicted in **Figure 7**. In this sense, the left plot illustrates the variation of both lift (C_L) and drag (C_D) coefficients with respect to the angle of attack. It is important to highlight that the AVL software employs the Vortex Lattice Theory to predict the aerodynamic coefficients and, thus, it does not predict the stall behavior at high angles of attack. In addition, this code does not calculate the zero-lift drag coefficient, and, therefore, the total drag coefficient was estimated through semiempirical methods [40, 46].
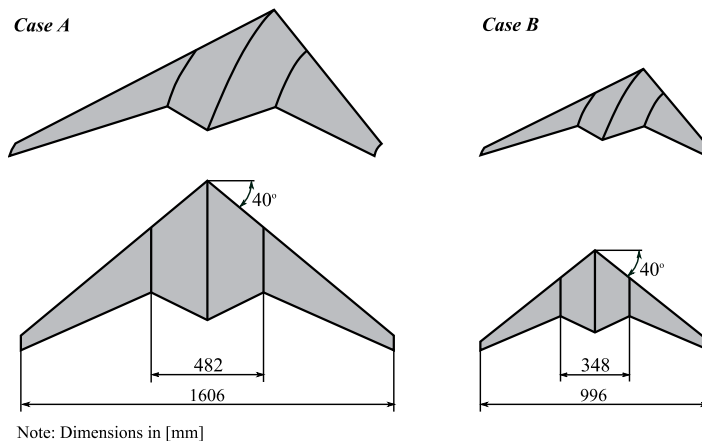

Note: Dimensions in [mm]

Figure 5.
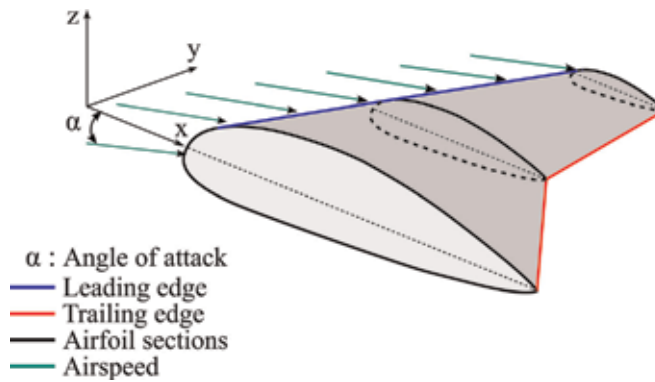*Graphical representation of BWB airframe for two design cases (dimension in mm).*

Figure 6.
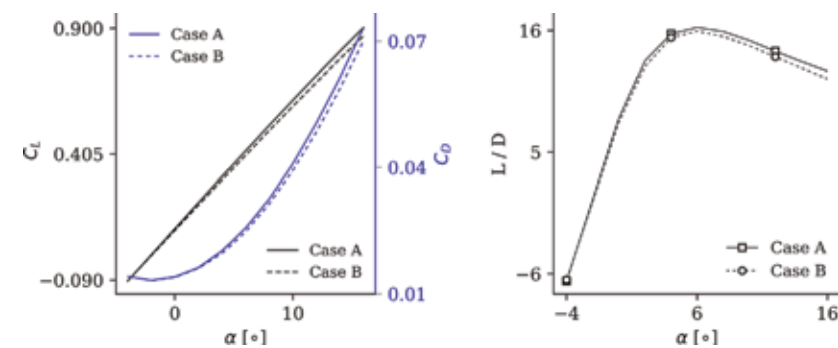*Angle of attack between the freestream and a half wing.*

Figure 7.
Drag polars of UAV conceptual models.

On the other hand, the right plot of **Figure 7** depicts the aerodynamic relation lift-to-drag (L/D) as a function of the angle of attack. This relation is a common way of reflecting the aerodynamic efficiency of an aircraft as a function of geometrical configuration and flight conditions. Moreover, this relation is highly important because it directly impacts on the endurance and range. The maximum L/D ratios obtained for cases A and B are 15.5 and 15.8, respectively. For this case, the minimum drag condition has been set for the cruise flight regime [35]. Finally, as seen in **Figure 7**, an L/D ratio of 8 at cruise condition is expected for both cases, which is in accordance with commercial UAV models [6].

On the other hand, the target power available, estimated by means of Eq. (3), was 302 W for both cases. This value is the same for cases A and B because their weight, aerodynamic coefficients, and operating conditions are almost equal, and hence an equivalent behavior is expected. Note that the estimated value through Eq. (3) is greater than the preliminary power required computed in the constraint analysis (**Table 3**) because during the initial sizing stage, several parameters were assumed based on historical and statistical data. Therefore, the power required calculated with Eq. (3) is more accurate because it considers the real performance and geometrical characteristics of the conceptual UAV.

3.4 Propulsion modelling

To investigate the integration of electric distributed propulsion into small UAV concepts, the available space on the trailing edge of the fuselage, as shown in
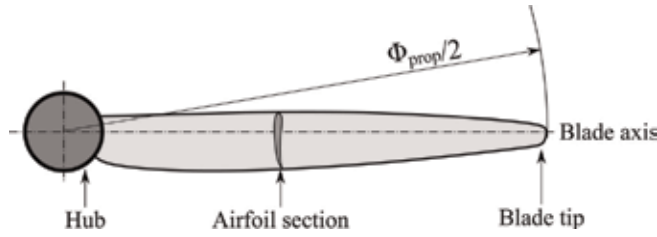
Figure 8.
Main components of propeller geometry.

Cases				N_P		
				1	2	3
Case A	$T_{req,T}$ = 20.1 [N] @ 15 [m/s]	$T_{req,i}$ [N]		20.10	10.05	6.70
		Φ_{prop} [in]		18.00	8.50	5.50
Case B	$T_{req,T}$ = 20.1 [N] @ 15 [m/s]	$T_{req,i}$ [N]		20.10	10.05	6.70
		Φ_{prop} [in]		13.00	6.00	3.75

Table 4.
Thrust required for distributed propulsion.

Figures 1 and **6** has been considered. This allows estimating a suitable diameter for the propeller Φ_{prop} (**Figure 8**) and setting the quantity of motors that fits adequately the available space and generate the power needed.

The thrust that each propeller must generate, in conjunction with their diameter, is presented in **Table 4** for both cases (A and B) with three distinct configurations: single and distributed propulsion with double and triple propulsors. Note that when the propulsion system possesses more than one propulsor, the thrust required per propeller ($T_{req,i}$) is obtained by dividing the total thrust required (T_{req}) by the number of installed propellers. Besides, it is important to mention that the term T_{req} was obtained by dividing the power required for the desired value for cruise speed (15 m/s for both cases).

3.4.1 Propeller selection

Tables 5 and **6** summarize the performance characteristics of selected propellers for cases A and B, respectively. The suitable models were established regarding the freestream velocity, their diameter, and the rotational speed. Special attention was paid to guarantee that the considered propeller arrangements fit the available space and, at the same time, generate the thrust required. The cruise speed was set for minimum drag condition [35].

For each propulsion set, several parameters from propellers, such as: non-dimensional coefficients (J, C_T, and C_P), efficiency, torque, shaft power, and thrust generated were extracted from the experimental database at desired operating conditions. Notice that the power available of individual propellers ($P_{A,i}$) was obtained by multiplying the power shaft for its corresponding propeller efficiency (η_p). Likewise, the total power available (P_A) is a function of the number or propellers (N_p) implemented, and it was obtained by multiplying N_p for its corresponding individual power ($P_{A,i}$). Finally, the power that battery must supply to the propulsion system was obtained by multiplying the power shaft for the

N_P	1		2		3	
Propeller	17×10	18×10	8×6	8×10	5×3	5×5
RPM $\times 10^3$	5	5	13	12	27	25
J	0.44	0.42	0.36	0.4	0.26	0.3
C_T	0.069	0.061	0.1078	0.1195	0.1145	0.1213
C_P	0.0415	0.0353	0.068	0.095	0.0642	0.0851
η_P	0.73	0.72	0.57	0.5	0.47	0.42
P_{shaft} [W]	432.5	499.6	294.5	320.6	238.1	249.1
$P_{A,i}$ [W]	315.7	359.7	167.9	160.3	111.9	104.6
P_A [W]	315.7	359.7	335.8	320.6	335.7	313.8
Q [Nm]	0.831	0.954	0.216	0.257	0.083	0.095
T_i [N]	20.2	22.7	10.5	10.1	7.4	6.7
T [N]	20.2	22.7	21	20.2	22.2	20.1
P_{bat} [kW]	0.432	0.499	0.589	0.641	0.714	0.747

Table 5.
Propeller selection—case A.

N_P	1		2	
Propeller	12×6.5	11×7	6×4	6×3
RPM $\times 10^3$	9	10	25	23
J	0.326	0.33	0.23	0.26
C_T	0.0979	0.1036	0.0949	0.1166
C_P	0.0544	0.0657	0.0473	0.0627
η_P	0.58	0.52	0.46	0.48
P_{shaft} [W]	589.1	634.5	344.5	355.7
$P_{A,i}$ [W]	335.8	329.9	158.5	170.7
P_A [W]	335.8	329.9	316.9	341.5
Q [Nm]	0.627	0.605	0.131	0.148
T_i [N]	23.1	21.5	10.8	10.9
T [N]	23.1	21.5	21.6	21.8
P_{bat} [kW]	0.589	0.634	0.689	0.711

Table 6.
Propeller selection—case B.

number of propellers implemented. Note that the shaft power and the battery power will be the same for a single propeller configuration because only one motor is considered and the electrical efficiency losses were neglected for practical purposes.

Note that, in **Tables 5** and **6**, the propeller efficiency is dramatically affected as its diameter is reduced. As observed, the lesser the propeller's size, the higher the rotational speed is needed to generate the required thrust. For instance, smaller models (e.g., three propellers 5×3) must operate at a high RPM (27,000) to produce the thrust required (**Table 4**). In contrast, a single larger propeller (e.g., a propeller 17×10) operates at lower RPM (5000) to generate the same thrust. These

aspects also reflect the variation of propeller efficiency due to its direct linkage to the cruise speed, rotational speed (ω), and propeller diameter (ϕ_{prop}) [47, 48]. In this sense, the decrease of propeller efficiency (as its diameter is lower) is attributed to the increase of the induced velocity at the propeller tips, which in turn increments the tip losses due to drag [47].

In addition, the lower propeller efficiency, the higher power that needs to be delivered by the motor (P_{shaft}). As observed in **Tables 5** and **6**, the large drop in efficiency (around 20% for the increment of one propeller) produces an increment in total power consumed. Nonetheless, the total power available (P_A) for all the cases remains almost constant, and it agrees the target power available (302 W).

Table 6 shows similar results as **Table 5**; however, it is worth to highlight that propeller efficiencies are even lower due to the smaller propeller's diameters for this case, which results in higher values of power shaft compared to case A. Additionally, note that the three-propeller configuration for this case was not assessed due to the unsuitability of allocating more than two propellers within the airframe trailing edge.

3.4.2 Motor selection

The selection of an electric motor for each set of propellers was accomplished through a catalogue-search of different manufacturers. The key parameters for motor selection and propeller-motor matching were the revolutions per minute (RPM), power shaft, and voltage constant. The latter represents a motor constant which correlates the RPMs and the operating voltage. Finally, when the set of the propeller and electric components is found, recommended values given by manufacturers for propeller pairing were used to check if the established arrangement meets the requirements.

Tables 7 and **8** present the motor devices for the propulsion configurations of cases A and B, respectively. As observed, for the distributed propulsion systems with three propellers of case A (**Table 7**) and with two propellers of case B (**Table 8**), it was not possible to find any off-the-shelf electrical motor that fulfills the propeller requirements, and, hence, they were not used in further analysis. For all favorable cases (first and second arrangements of case A and first set of case B), adequate motor models were decided, and their operating parameters were employed to size and select a suitable battery to perform a given mission.

N_p	Propeller	Motor	RPM	Battery cells	K_V	I_{m0} [A]	U_{m0} [V]	R_m [Ohm]
1	17×10	A40-14L V4 14-Pole	6000	6S	355	0.85	8.4	0.050
2	8×6	A40-12S V4 8-Pole	12,820	3S	1350	1.94	8.4	0.018
3	5×3	No motor matching	–	–	–	–	–	–

Table 7.
Motor selection—case A.

N_p	Propeller	Motor	RPM	Battery cells	K_V	I_{m0} [A]	U_{m0} [V]	R_m [Ohm]
1	12×6.5	A30 8 XL V4	9500	3S	1100	2.8	8.4	0.015
2	6×3	No motor matching	–	–	–	–	–	–

Table 8.
Motor selection—case B.

3.5 Performance assessment

As mentioned, the performance of an electric aerial vehicle mainly depends on the battery capacity and the total current draw supplied to the propulsion system. For this work, a single battery device was considered for each configuration, even in the case of distributed propulsion. In this way, the battery current (I_B) was computed as a function of several motor parameters such as voltage constant (K_v), no-load current (I_{m0}), no-load voltage (U_{mo}), and motor resistance (**Tables 7** and **8**). Another parameter employed for the battery selection was its nominal voltage (U_B), which is directly linked to the number of internal cells.

For case A, when a single propeller is considered, the battery voltage is almost twice the voltage of the distributed propulsion scenario. This is because a larger propeller demands higher torque to work properly, and hence a larger motor that works with a higher voltage is employed. Nonetheless, it is also observed that the current supplied by the battery to the motors (I_B) for the distributed propulsion configuration is twice the value of the single propeller set. This is because two motors that work in a parallel are employed in the first case. Moreover, it is seen that the motor of case B-1 requires a lower voltage than the case A-1, because of the difference in size of the propellers employed (**Tables 5** and **6**). The number of cells of the battery for each configuration was set according to the manufacturer suggestion. **Table 9** compiles the results of general battery characteristics such as the number of cells and total current that battery supplies.

Regarding the takeoff gross weight estimation, it can be appreciated that the higher the nominal voltage, the higher number of cells from the battery and hence the aircraft weight increases. In this sense, two different scenarios were investigated to select a battery. The first one consisted of selecting a desired capacity from commercial datasheets, and, from this, the vehicle performance was assessed. For this approach, **Table 10** and **Figure 9** present the UAV weight estimation and its breakdown for the three configurations once the battery characteristics have been outlined. Meanwhile, **Table 11** shows the estimated range and endurance under these battery characteristics.

It is interesting to note that for case A, the takeoff gross weight (W_{TO}) of the aircraft is lower when the distributed propulsion system is implemented; however, the weight fractions of the components are altered. For instance, the propulsion

Case	N_p	Cells	U_B [V]	U_{eo} [V]	I_m [A]	I_B [A]
CA-1	1	6	22.2	19.1	31.9	28.4
CA-2	2	3	11.1	10.7	32.6	63.8
CB-1	1	3	11.1	10.8	75.4	74.2

Table 9.
Parameter for battery selection—cases A and B.

Case	N_p	W_{motor} [kg]	$W_{propeller}$ [kg]	W_{ESC} [kg]	$W_{battery}$ [kg]	$W_{fuselage}$ [kg]	$W_{payload}$ [kg]	W_{TO} [kg]
CA-1	1	0.275	0.063	0.05	2.024	0.538	1	3.95
CA-2	2	0.190	0.014	0.05	1.055	0.538	1	3.10
CB-1	1	0.177	0.041	0.06	1.055	0.118	1	2.45

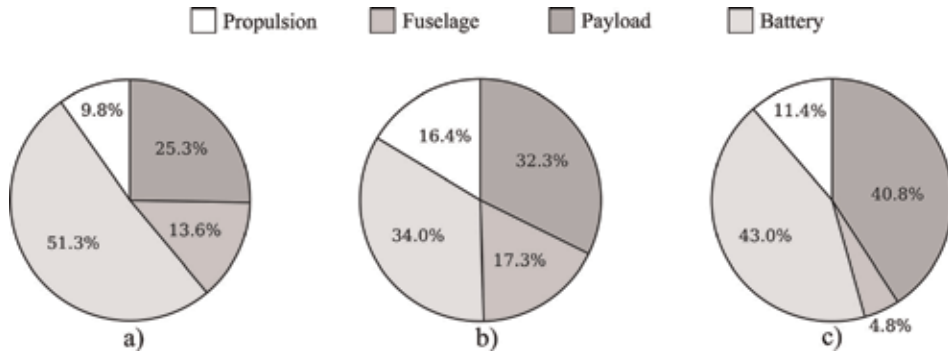**Table 10.**
Weight assessment—cases A and B.

Figure 9.
UAV—weight breakdown. (a) Case A-1 propeller, (b) case A-2 propeller, and (c) case B-1 propeller.

Cases	Method 1			Method 2		
	Input	Output		Input		Output
	C_B [mAh]	E [min]	R [km]	E [min]	R [km]	C_B [mAh]
CA-1	16,000	27.1	24.39	30	27	17731
CA-2	16,000	12.0	10.8	30	27	39,892
CB-1	16,000	10.3	9.27	30	27	46,378

Table 11.
Battery selection—cases A and B.

system mass fraction increments from 9.8 to 16.4%, and, in similar way, the fuse-lage mass fraction increases from 25.3 to 32.3%. Although the lessening of weight that resulted from the implementation of the distributed propulsion system, this is overshadowed by the lessening of the endurance and range of the aircraft because the power consumed by the motors in the distributed propulsion scenario is higher, as showed in **Table 11**.

At last, comparing the single propeller configurations (**Figure 9a** and **c**) indicates that fuselage mass fraction is decreased for case B because of its smaller geometry. Note that the battery mass fraction is lower for case B because a 3-cell battery was employed for this configuration; meanwhile, for case A, a 6-cell configuration was utilized, which results in a weight increment.

The second performance approach determined the minimum battery capacity required for a target endurance and range. **Table 11** (Method 2) shows the results for case A (one and two-propeller configuration) and case B (one-propeller configuration). As can be seen, for the same target endurance, the battery capacity for the distributed propulsion configuration is dramatically raised compared with the single propeller setting. In other words, the capacity lasts less due to the augment of current draw that the battery must provide as consequence of the loss in propeller efficiency. When comparing the one-propeller configuration of both cases (A and B), it is observable that the endurance reduces for case B because of the aerodynamic and propulsion drawbacks arising from a lesser wetted area and lower efficiency of the propeller.

The results from the second method of performance assessment showed that the required battery capacity to accomplish a specific mission increases for distributed propulsion arrangements. As observed in **Table 11**, the capacity to perform the

same mission flight is different for all three cases because of the notable increment of the current draw (**Table 9**).

4. Summary

Wetland monitoring at the Andean highlands presents imperious needs in terms of more efficient and environmentally friendly UAV designs. The challenges imposed by the hard-operating requirements make commercial electrical small UAVs not suitable for monitoring tasks. However, their lower environmental impact and low costs encourage their improvements through the implementation of different technologies. In this context, this work has assessed the performance of two different configurations using electrical distributed propulsion system. Since for this particular application the payload required is small, the search for architectures with a large number of propulsors was not suitable, and hence the maximum number of propellers that could be allocated was set to three. The results showed that the propeller's size reduction affected dramatically its performance, outweighing the benefits in weight and propulsive efficiency. The results from the performance analysis show that endurance, range, and weight decrease for distributed propulsion configurations. The reduction on total aircraft weight is beneficial; however, this was outweighed by the lower thermal performance of the propellers, which reflected on higher total power consumption for the distributed propulsion cases. It is important to highlight that distributed propulsion may be a good option when the propeller's size does not decrease so dramatically as in the configurations studied. This aspect is a key variable in order to assess a recommendable range for distributed propulsor size, where the benefits obtained from weight, reliability, control, and aerodynamic aspects are not to be affected by the thermal propulsors' performance.

Another aspect to highlight in this study is that conversely to other aviation sectors, the small UAV category allows to implement or design an important variety of electronic propulsion components, which can be easily tailored for the operating requirements. This aspect opens up the door to generate more flexible designs which incorporates forefront technology such as thrust vectoring, boundary layer ingestion (BLI), and propulsion airframe embedded (PAE) designs, among others in exchange of moderate costs. In this sense, it is important to implement a versatile and flexible optimization methodology, which enables the assessment of different geometrical configurations accounting for the aerodynamic and propulsion integration at system engineering perspective. These routines will enable to evaluate a larger range of aircraft configurations, and it will contribute to establish ideal models that fulfill the requirements from a synergetic standpoint.

Finally, since this study was implemented at conceptual level, the distortion features and momentum reduction produced by the ingestion of the boundary layer have not been considered. Nonetheless, further studies to determine the compromise between size and propeller performance incorporating BLI aspects need to be carried out.

Acknowledgements

Abbreviations and nomenclature

ρ_{alt}	air density at desired altitude [kg/m^3]
ω	motor/propeller rotational speed [RPM]
ϕ_{prop}	propeller diameter, [in]
η_e	electric set (motor, battery, ESC) efficiency
η_{prop}	propeller efficiency
BWB	blended wing body
C_D	drag coefficient
C_L	lift coefficient
C_B	battery capacity [mAh]
C_{min}	minimum battery capacity [mAh]
E	endurance [min]
I_B	total current [A]
I_m	motor current [A]
I_{m0}	nominal no-load motor current [A]
K_V	voltage constant [RPM/V]
N_p	number of propellers
RC	rate of climb [m/s]
S	planform wing area [m^2]
P_A	power available [W]
P_R	power required [W]
P_{Rp}	preliminary power required [W]
P_{shaft}	power shaft of the motor [W]
P_{bat}	power of battery [W]
Q	torque [Nm]
T	thrust [N]
UAV	unmanned aerial vehicle
U_B	nominal battery voltage [V]
U_{m0}	nominal no-load voltage of motor [V]
U_{eo}	equivalent battery voltage [V]
V_{max}	maximum flight speed [m/s]
V_c	cruise speed [m/s]
V_s	stall speed [m/s]
W/S	wing loading [N/m^2]
W/P	weight to power ratio [N/W]
$W_{battery}$	battery weight [N]
W_{ESC}	electronic speed control weight [N]
$W_{fuselage}$	fuselage weight [N]
W_{motor}	motor weight [N]
$W_{payload}$	payload weight [N]
$W_{propeller}$	propeller weight [N]
W_{TO}	takeoff gross weight [N]
W_{TOp}	preliminary takeoff gross weight [N]

Author details

Esteban Valencia*, Víctor Alulema and Darío Rodríguez
Department of Mechanical Engineering, National Polytechnic School, Quito,
Ecuador

*Address all correspondence to: esteban.valencia@epn.edu.ec

IntechOpen

References

[1] Baruch Z. Ordination and classification of vegetation along an altitudinal gradient in the Venezuelan páramos. Vegetatio. 1984;**55**(2):115-126

[2] Schoolmeester T et al. Outlook on climate change adaptation in the Tropical Andes mountains. 2016

[3] da GABF, Norman Myers JK, Mittermeier RA, Mittermeier CG. Biodiversity Hotspots for conservation priorities. Nature. 2000;403

[4] Josse CE, Cuesta F, Navarro G, Barrena V, Chacón-Moreno ESJ, Ferreira W, et al. Ecosistemas de los Andes del Norte Centro. Bolivia, Colombia, Ecuador, Perú y Venezuela. Lima: Secretaría General de la Comunidad Andina, Programa Regional ECOBONA-Intercooperation, CONDESAN-Proyecto Páramo Andino, Programa BioAndes, EcoCiencia, NatureServe, IAvH, LTA-UNALM, ICAE-ULA, CDC-UNALM, RUMBOL SRL; 2009

[5] Buytaert W et al. Human impact on the hydrology of the Andean páramos. Earth-Science Reviews. 2006;**79**(1–2):53-72

[6] Gundlach J. Civil and Commercial Unmanned Aircraft Systems. Washington, DC: American Institute of Aeronautics and Astronautics, Inc; 2016

[7] Marcaccio JV, Markle CE, Chow-Fraser P. Unmanned aerial vehicles produce high-resolution, seasonally-relevant imagery for classifying wetland vegetation. International Archives of the Photogrammetry, Remote Sensing and Spatial Information Sciences. 2015;**40**(1W4):249-256

[8] Shahbazi M, Théau J, Ménard P. Recent applications of unmanned aerial imagery in natural resource management. GIScience Remote Sensing. 2014;**51**(4):339-365

[9] E. 38 Unmanned Systems. The E384 Mapping Drone – Event 38 Unmanned Systems. 2018. [Online]. Available from: https://event38.com/fixed-wing/e384-mapping-drone/ [Accessed: 18-June-2018]

[10] Parrot. Parrot DISCO FPV | Official Parrot® Site. [Online]. Available: https://www.parrot.com/us/drones/parrot-disco-fpv#-parrot-disco-fpv [Accessed: 12-Sep-2018]

[11] Valencia E, Saá JM, Alulema V, Hidalgo V. Parametric study of aerodynamic integration issues in highly coupled Blended Wing Body configurations implemented in UAVs. 2018. pp. 1-15

[12] Panagiotou P, Fotiadis-Karras S, Yakinthos K. Conceptual design of a blended wing body MALE UAV. Aerospace Science and Technology. 2018;**73**:32-47

[13] Lehmkuehler K, Wong KC, Verstraete D. Design and test of a UAV blended wing body configuration. 28th Congr Int. Counc. Aeronaut. Sci. 2012, ICAS 2012, vol. 1. April. 2012. pp. 432-442

[14] Panagiotou P, Yakinthos K. Parametric aerodynamic study of Blended-Wing-Body platforms at low subsonic speeds for UAV applications. In: 35th AIAA Appl. Aerodyn. Conf., no. June. 2017. pp. 1-19

[15] Dehpanah P, Nejat A. The aerodynamic design evaluation of a blended-wing-body configuration. Aerospace Science and Technology. 2015;**43**:96-110

[16] Leifsson L, Ko A, Mason WH, Schetz JA, Grossman B, Haftka RT. Multidisciplinary design optimization of blended-wing-body transport aircraft

with distributed propulsion. Aerospace Science and Technology. 2013;**25**(1): 16-28

[17] Hepperle M. Electric Flight–Potential and Limitations. 2012. pp. 1-30

[18] Gundlach J. Designing Unmanned Aircraft Systems: A Comprehensive Approach. Manassas, Virginia: American Institute of Aeronautics and Astronautics, Inc; 2011

[19] Gohardani AS. A synergistic glance at the prospects of distributed propulsion technology and the electric aircraft concept for future unmanned air vehicles and commercial/military aviation. Progress in Aerospace Science. 2013;**57**:25-70

[20] Kim HD, Perry AT, Ansell PJ. A review of distributed electric propulsion concepts for air vehicle technology. In: 2018 AIAA/IEEE Electr. Aircr. Technol. Symp. 2018

[21] Herwitz SR, Johnson LF, Dunagan SE, Higgins RG, Sullivan DV, Zheng J. Imaging from an unmanned aerial vehicle: Agricultural surveillance and decision support. Revista de Derecho Comunitario Europeo. 2011;**39**(15): 523-540

[22] Grenzdörffer G et al. The photogrammetric potential of low-cost UAVs in forestry and agriculture. International Archives of the Photogrammetry, Remote Sensing and Spatial Information Sciences. 2008;**1**: 1207-1213

[23] Al-Hajjaji K, Ezzin M, Khamdan H. Design, Development and Evaluation of a UAV to Study Air Quality in Qatar. Qatar; 2017

[24] Johnson LF, Herwitz S, Dunagan S, Lobitz B, Sullivan D, Slye R. Collection of ultra high spatial and spectral resolution image data over California

vineyards with a small UAV. Biosystems Engineering. 2013;**108**(4):49-61

[25] Macjke DC Jr. Systems and image database resources for UAV search and rescue applications [masters theses]. 2013. p. 115

[26] Sadraey M. Aircraft Design: A Systems Engineering Approach. Vol. 27 (1). New Hampshire, USA: Wiley; 2013

[27] Keane AJ, Sóbester A, Scanlan JP. Small Unmanned Fixed-Wing Aircraft Design: A Practical Approach. John Wiley & Sons; 2017

[28] Glīzde N. Wing and engine sizing by using the matching plot technique. Transport and Aerospace Engineering. 2017;**5**(1):48-59

[29] Sóbester A, Forrester AIJ. Aircraft Aerodynamic Design: Geometry and Optimization. 2014

[30] Bertin JJ, Rusell C. Aerodynamics for Engineers, 6th ed. Harlow Essex England: Pearson, 2014

[31] Ol M, Zeune C, Logan M. Analytical/experimental comparison for small electric unmanned air vehicle propellers. In: 26th AIAA Appl. Aerodyn. Conf., no. August. 2008

[32] Brandt J, Selig M. Propeller performance data at low Reynolds numbers. In: AIAA. 2011

[33] Sadraey MH. Aircraft Performance: An Engineering Approach. Boca Raton: CRC Press; 2017

[34] Anderson JD. Aircraft Performance and Design. 2003

[35] Ruijgrok GJJ. Elements of Airplane Performance. 2nd ed. Leeghwaterstraat: Delft University Press; 2009

[36] Quan Q. Introduction to Multicopter Design and Control. 2017

[37] Drela M. DC Motor/Propeller Matching - Lab 5 Lecture Notes. 2005;**6**:6

[38] Avanzini G, De Angelis EL, Giulietti F. Optimal performance and sizing of a battery-powered aircraft. Aerospace Science and Technology. 2016;**59**:132-144

[39] Elekes G. A geometric inequality and the complexity of computing volume. Discrete & Computational Geometry. Dec. 1986;**1**(4):289-292

[40] Valencia EA, Hidalgo V, Rodriguez D. Parametric modelling for aerodynamic assessment of a fixed wing UAV implemented for Site Specific Management. In: 2018 AIAA Inf. Syst. Infotech @ Aerosp., no. January. 2018. pp. 1–17

[41] Traub LW. Range and endurance estimates for battery-powered aircraft. Journal of Aircraft. 2011;**48**(2):703-707

[42] Scarpino M. Motors for Makers A Guide to Steppers, Servos, and Other Electrical Machines; 2016

[43] Kontogiannis S, Ekaterianaris J. Design, performance evaluation and optimization of a UAV. Aerospace Science and Technology. 2013;January: 339-350

[44] Sóbester A, Forrester AIJ. Aircraft Aerodynamic Design: Geometry and Optimization. 2014

[45] Shim HJ, Park SO. Low-speed wind-tunnel test results of a BWB-UCAV model. Procedia Engineering. 2013;**67**: 50-58

[46] Gur O, Mason WH, Schetz JA. Full-configuration drag estimation. Journal of Aircraft. 2010;**47**(4):1356-1367

[47] Filippone A. Advanced Aircraft Flight Performance. 2010

[48] Torenbeek E. Synthesis of Subsonic Airplane Design. Dordrecht: Springer Netherlands, 1982

Chapter 4

Beamed Launch Propulsion

Koichi Mori

Abstract

An advanced concept of launch system from ground to orbit, called laser launch system, has been discussed. As a 100-kW-class fiber laser has been developed today, the laser propulsion is now a realistic option for launching microsatellites frequently at very low cost. In this chapter, we shall discuss several unresolved technical problems such as propulsion design and laser beam transmission through atmosphere. It is proved theoretically that high specific impulse higher than 900 seconds is possible in a new conceptual design. On the other hand, the laser beam may be suffered by the atmospheric turbulence when the launch vehicle reaches at altitude higher than 10 km.

Keywords: launch vehicle, laser propulsion, laser, rocket propulsion, wireless power transmission

1. Introduction

In this chapter, we consider the unknown system called laser propulsion. Designing the system is a mixture of various engineering fields, including propulsion engineering, laser engineering, electromagnetic wave engineering, flight dynamics, and control engineering, which are interconnected to each other. The laser propulsion has been studied in the field of the propulsion engineering for more than 50 years. Moreover, the laser propulsion appeared as a gadget in several sci-fi works [1, 2]. (Strangely, in all those works, the laser propulsion is introduced as a technology of aliens rather than an earth-oriented technology. It would reflect that this technology is full of mysterious images.) However, in view of the practical application, few have achieved so far. This is mainly because no laser facilities whose continuous power is sufficiently high have been available. However, in 2010, the world has changed. A 100 kW fiber laser has been commercialized by IPG Photonics Inc. A 100 kW fiber laser facility has been delivered to the NADEX laser R&D Center in Fukui, Japan. We come to the place where we can do genuine experiments of laser propulsion. Surrounding situations are being prepared today. Laser propulsion is one step short of practical application.

As shown in **Figure 1**, in the laser launch system, a vehicle is propelled by transmitting the propulsive energy via laser beam from the ground. Gaining the specific impulse higher than the practical chemical propulsions, the laser propulsion is of the same class of the electric propulsion for spacecraft. At the same time, by leaving the heavy part of the energy source on the ground, the lightweight vehicle on the basis of simple propulsion energy system is realized.

In the following, at first, we are going to consider why the laser propulsion is necessary. For this, we need to consider what kind of launch systems will be required in near future. The conventional rocket technology is in the period of
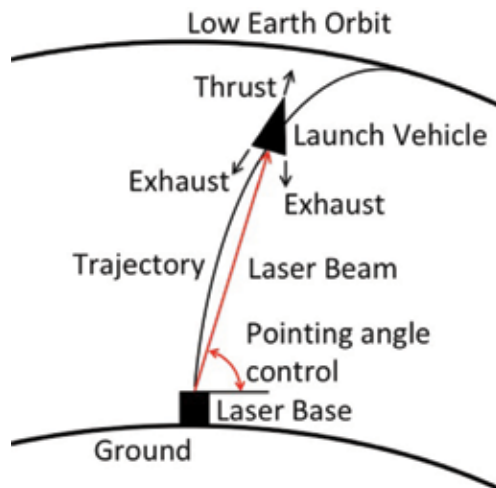
Figure 1.
Laser launch system.

maturity, while the fetal movement for new launch system of high specific impulse that is not limited by the chemical reaction has been ignited. Then, we need to investigate what kind of the laser propulsion system is technologically feasible. Ensuring the foregoing studies of the laser propulsion, we shall consider the practical laser launch system. The technological problems to be solved are numerous. The laser transmission through turbulent atmosphere gives critical problems to the feasibility in the laser launch system although they have been half ignored so far. Solving the numerous technological problems that are necessary to realize the laser launch system is related to the advanced technology such as Starshot project [3], space-based solar power [4], and laser communication in space [5]. Naturally, the space will become familiar by realizing the laser propulsion. Laser propulsion is the technology that is worth challenging.

2. Principles of laser propulsions

Laser propulsion is a variation of the wireless power transfer (WPT) technology, which transfers power remotely using electromagnetic (EM) waves such as microwaves or laser beams. When electric power is necessary at the receiving side, the power of EM waves is transformed to dc current using semiconductors. For the laser propulsion, the power of EM waves is transformed directly into the enthalpy of a working fluid to generate momentum via thermal propulsion mechanisms. This can be called the laser thermal propulsion (LTP). Similar idea would be the laser electric propulsion (LEP) that converts the EM wave power to the dc power to store in the battery once, and then the dc power is used to generate thrust via electric propulsion mechanisms. The LEP is a new idea that allows the storage of the energy on board. However, the heavy weight of the battery would be the bottleneck for the feasibility of this system. Moreover, the LTP will be more energy efficient than LEP because the LEP requires multiple energy conversion processes, which lose the power at each stage. On the other hand, for LTP, it is necessary that the laser beam is always irradiated on the vehicle so that the control mechanisms keep the linkage between a laser source on ground and a fast-moving vehicle. Moreover, it is necessary to keep the vehicle in sight of the laser source so that available flight trajectory of the vehicle is largely limited. Furthermore, the atmospheric perturbation to the

laser beam may be a critical factor in the feasibility study of the LTP. A laser beam is transmitted across turbulent atmosphere for a long distance up to 100 km from ground to space.

There are two kinds of the laser propulsion: repetitive pulse (RP) laser type and continuous wave (CW) laser type. The concept of laser propulsion is first proposed by Kantrowitz in 1971 [7]. His concept was to irradiate the laser beam on the ablator installed on the bottom surface of the vehicle as propellant. At that time, it was unknown how much the momentum can be generated for a certain laser power. The research team led by Kantrowitz first investigated the momentum coupling performances of RP laser propulsion and its physical mechanisms. As a result, the impulse generation mechanisms of laser-supported detonation waves and laser-supported combustion waves have been developed. At the beginning of 2000s, Myrabo invented a new vehicle design called a Lightcraft, which is illustrated in **Figure 2**, to perform first launch demonstrations using a 10-kW-class CO_2 RP laser facility of US Air force [8]. He succeeded in the independent flight of the vehicle without any external guide or support except for the laser beam for the first time in the world. The world record of the flight altitude was 71 m. Through the development of the Lightcraft, Myrabo developed the concept of "beam-riding." The vehicle must be kept irradiated to generate the momentum all the time of flight. Lightcraft was designed to keep its trajectory along a fixed laser beam, while this is the meaning of the term of beam-riding. When the vehicle position is deviated from the laser beam, the recovery side force is generated to the vehicle to keep the trajectory. His consideration was epoch-making because no previous studies in the laser propulsion have considered the flight dynamics of the vehicle. In the same periods, Sasoh invented the in-tube laser propulsion, which is illustrated in **Figure 3**, and investigated the concept experimentally using a 1-kW-class RP CO_2 laser. A projectile could be accelerated in a tube efficiently due to the confinement effect of the tube wall. In the times of early 2000s, several different types of RP laser propulsion have been invented and investigated experimentally. The concepts of laser propulsion that have been proposed so far are reviewed in the two review papers in detail [9, 10]. From the research team of the author, new laser launch system using "donut-beam," whose power density has hollow distribution on the cross-sectional plane, higher at peripheral of the cross section than at the center, and a spherical vehicle for stable acceleration has been proposed. This concept is studied in experiments [11] and numerical simulations [12]. Because the concept uses the atmospheric air as propellant, the acceleration performance of vehicle is determined by the aerodynamic drag and the atmospheric air density to be propelled using the laser power. Each concept of
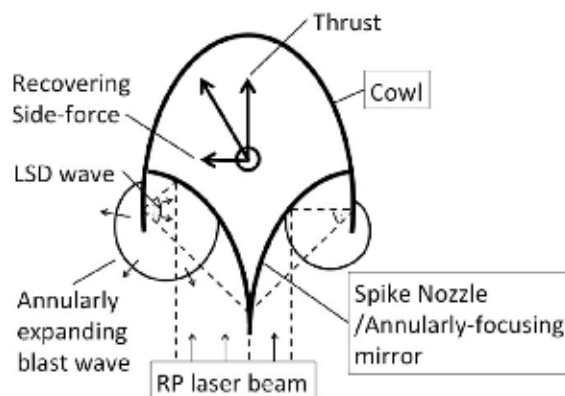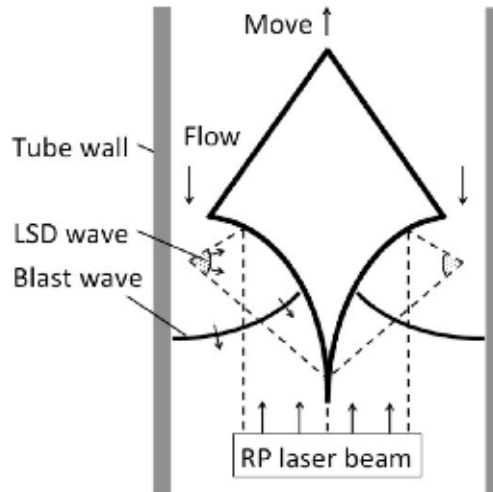

Figure 2.
Myrabo's Lightcraft.

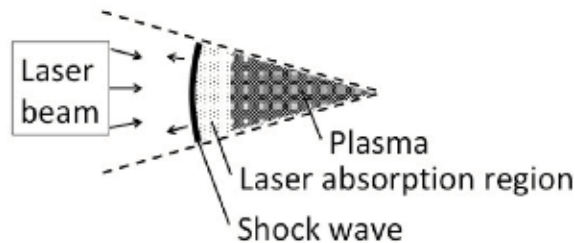**Figure 3.**
Sasoh's LITA.

Figure 4.
Laser-supported detonation wave.

RP laser propulsion uses only gaseous propellant or only solid propellant, called the laser ablative propulsion, or the both. The gaseous propellant mostly used is the air atmosphere, and air-breathing propulsion concepts have been studied by many researchers. By focusing an intense laser pulse in the air, a laser-supported detonation wave is generated instantaneously to generate a blast wave around the optical focal point, as illustrated in **Figure 4**. The impulsive thrust is generated as recoil of the blast wave reflection in the nozzle. This method is a variation of the pulse detonation engine (PDE), which generates the thrust via isochoric heating and unsteady gas expansion. The source of the gas expansion, the LSD wave can be generated even in the hypersonic flow, and it can be applied in the air-breathing engines that can operate in hypersonic speeds.

For the CW laser propulsion, only gaseous propellants have been used, because strong momentum coupling from laser ablation requires intense and short laser pulse, and the power density from the CW lasers is too small to be used for the laser ablative propulsion. Moreover, no air-breathing engines have been studied for CW laser propulsion. Two different kinds of rocket were proposed. The laser-sustained plasma (LSP) engines, illustrated in **Figure 5**, use the plasma kept by laser absorption to heat the gaseous propellant running through it [13]. The strong point of this type is high specific impulse more than 1000 seconds because of the high temperature of plasma more than 10,000 K. Mystery remains in plasma stability to the perturbation of the laser power density and its distribution relative to the flows of propellant. Strict optical alignment is necessary for operation. Another kind is heat

exchanger (HX) rocket proposed by Kare, which is illustrated in **Figure 6** [14]. The laser power is converted to the propellant enthalpy via solid heat exchanger so that the specific impulse is limited up to 900 seconds due to the allowable maximum temperature for the heat exchanger. However, the strict optical alignment is not necessary for its operation, and this type is robust to the perturbation to the laser power density and the distribution that is expected during the flight. In the CW laser propulsion, the propellant is heated through the isobaric process, and a propellant pump for an additional compression process is necessary. Hence, the engine for CW laser propulsion is more complicated and then heavier than the RP laser propulsions. This is why no launch test has been accomplished until today.

High-power laser is the first priority to realize the laser launch system (LLS). In all the previous studies, except for Myrabo's campaign, the time-average power of the laser was around a few kilowatt is too low for the practical experiment. As mentioned above, 1 MW laser power is necessary to launch 1 kg payload. Hence, if you want to launch 1-ton payload as in the case of the conventional chemical rockets, you need to prepare 1 GW laser facility. This power is 10^6 times as high as in the previous experiments, and it would be natural to think that even the basic phenomena should be different for such high-power laser in the foregoing experiments. In the previous experiments, it is impossible to generate and maintain continuously a laser-supported detonation wave using CW laser, while it will become possible if one uses the MW or GW-class laser. Once the heating
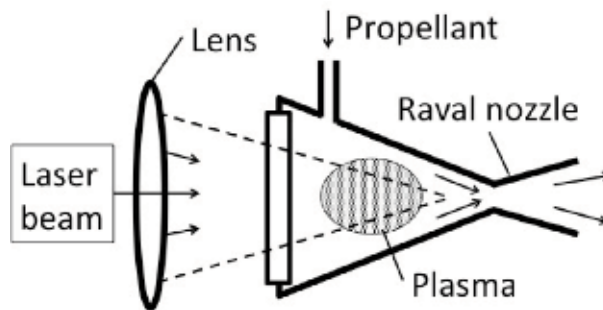
Figure 5.
LSP type CW laser propulsion.
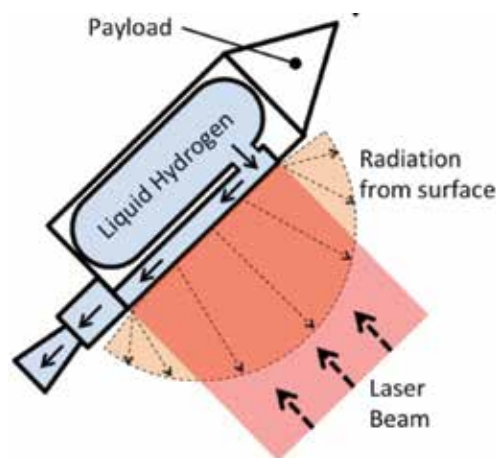
Figure 6.
Heat exchanger rocket.

mechanism is changed, the propulsion design will change. Evolution of super high-power CW laser will induce a new research domain of "high-power CW laser engineering."

On the other hand, it should be reasonable to assume that the minimum weight of launch vehicle should be heavier than 100 g. As the vehicle becomes smaller, the structural mass ratio is expected to increase to assure the structural strength. Hence, the minimum CW laser power for launch demonstrations should be around 100 kW. Of course, this estimate is quite rough, and the structural design of vehicle, propulsion performance, and trajectory plans should be considered for more detailed feasibility study. The launch system of laser power at 100 kW–1 MW is possible soon. There exists 100 kW fiber laser. It is technically possible to build a 1 MW laser by increasing the number of bundled fibers, and it is the matter of budget. Recently, high-power, energy-efficient, and compact fiber laser has been evolving. CW laser is easier to attain high power rather than RP laser especially in the case of fiber laser. If we could construct the LLS powered by CW laser, the launch demonstration will be completed at early times. As noted above, the design of LLS is the art of the integration in a broad area of engineering field. The relevant field includes propulsion, laser, beam transmission, flight dynamics, and control engineering.

Even after a high-power laser becomes available, a number of the engineering problems are remained. If we could have a proper propulsion system, we should determine the trajectory of a vehicle. The basic guidance law of conventional launch vehicles is the bilinear tangent law. Typical trajectory is illustrated in **Figure 7**. However, for LLS, we need to concern the special issue that a vehicle must stay on the laser beam. Kantrowitz assumed a circular trajectory at which center the laser source is located. It is illustrated in **Figure 8**. For such a trajectory, a good point is that the laser beam can always be irradiated onto the side surface of the vehicle fuselage. Similar trajectory was considered by Escape Dynamics Inc. Possible bad point is the unknown effects of the atmospheric turbulence on the laser beam transmission. Because the atmospheric turbulence is especially strong near the ground, the laser beam should be distorted drastically. This effect gives the degradation of the energy efficiency of the laser beam transmission and the engineering problem to keep a "laser link" between the vehicle and the ground laser facility. Katsurayama et al. proposed a zenith trajectory for LLS as illustrated in **Figure 9**
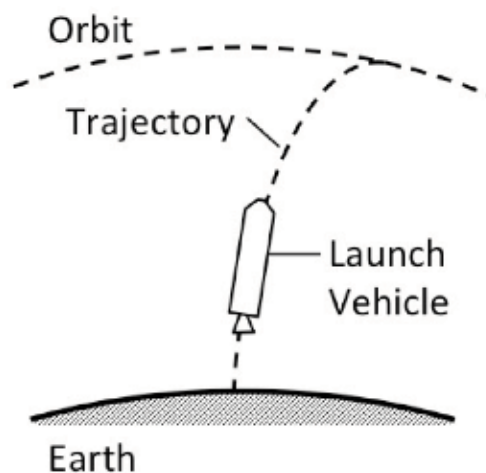

Figure 7.
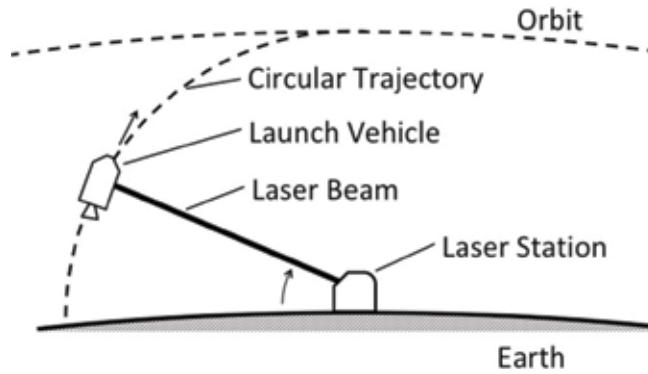*Typical trajectory of conventional launch vehicles.*

Figure 8.
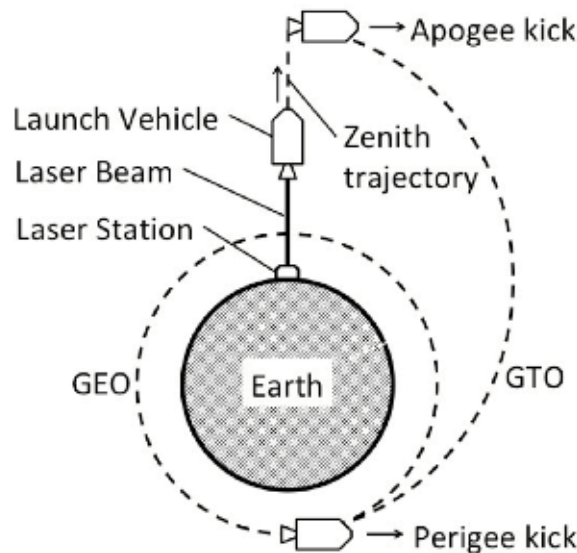*A circular trajectory concept for laser launch.*

Figure 9.
A zenith trajectory concept for laser launch G.

[15]. The zenith trajectory gives the minimum influence of the turbulence on the beam transmission. A vehicle is transferred via apogee-kick efficiently to the orbit around the earth. They consider using air-breathing engines, which can produce higher velocity increments on horizontal flight, and the optimum trajectory will be possibly determined from the trade-off between the effect of the air turbulence on the laser beam transmission and the air-breathing engine performance. Phipps et al. solved the optimum trajectory for RP laser ablative rocket, without any air-breathing engine, from the ground to the orbit [16]. They commented simply to the effect of the air turbulence on the laser beam propagation. They concluded that the effect of the air turbulence is ignorable to the laser beam whose cross-sectional diameter is smaller than the "seeing size," which will be explained below; typical value is around 10 cm for the wavelength at 530 nm. They also suggested how to correct the pointing error due to the wave front tilt. More detailed estimation and system design in this aspect is important for the feasibility of LLS.

Moreover, the control mechanisms to keep the laser link between the ground and vehicle are indispensable to maintain the continuous energy supply via laser beam for the operation of the propulsion system. Sasoh's LITA and Myrabo's

Lightcrafts are the concepts of the passive way to maintain the laser link. On the other hand, Phipps considered an active control of the optics onboard of the vehicle of the ablative launch system for the first time. Finally, the cooperative control between vehicle and beam pointing will be the natural solution for this issue. For the beam pointing control, the information of the beam position and vehicle position should be resolved precisely. The spatial resolution should be around 1 cm. We need to innovate a high-resolution method to measure vehicle and beam position. After considering these problems, it is clear that the propulsion design and the air turbulence effect on the beam transportation are the root problem.

3. Motivation of laser propulsion

In order to expand the human activities in space, it is indispensable to drastically reduce the cost of transportation from ground to orbit. For an example of today's launch cost, the launch cost for a unit payload mass of the actual rocket of Japan, H-II, to launch a 6 ton payload to geo transfer orbit is around 20,000 $/kg. Today the price competition is intense so that much of the same is the launch cost value in the USA and EU. Drastic reduction of the launch cost for the unit payload mass has been at stake for a long period. The space shuttle is the first attempt to reduce the launch cost. Shuttle was the first partly reusable launch vehicle. The orbiter was designed reusable to reduce the launch cost by using the orbiter repetitively at a high frequency. However, as it is well-known today, the space shuttle launch system was too huge and complex to reduce the launch cost due to the expensive maintenance. The Space Shuttle Project left the severe lessons for the engineers who still dream to develop a new reusable launch vehicle. Today, the expandable launch vehicles (ELVs) are still major way to the orbit, and the engineers are reducing the cost mainly by the standardization and the simplification. For an example, the next H-III rocket of Japan is claimed to halve the launch cost.

Falcon Heavy produced by SpaceX is a huge rocket that can deliver 26.7 ton to GTO, which is four times as heavy as H-IIA, reducing the launch cost for an unit payload mass around to 6000 $/kg, which is around one-third of the H-IIA. This is not surprising. On the basis of the statistical data of the ELV developed so far, the launch cost of the ELV has a trend to decrease inversely with the vehicle size [6]. The launch cost for a unit payload mass draws a unique curve decreasing with the payload mass for the same launch mission. Falcon Heavy owes its low price to its large size. It is unclear if the price would continue to decrease with increasing the rocket size, like a huge launch vehicle for the interplanetary transport system designed by SpaceX. For the drastic cost cut, revolutionary breakthrough is necessary to compete the launch market.

To the opposite direction, the unit launch cost naturally increases with the decreasing the payload weight. Recently, R&D of small satellites is very active, and the nanosats (lighter than 10 kg) and picosats (<1 kg) will become in practice soon. Then, the demand for very small launch vehicle (VSLV) at reasonable cost is increasing. Several teams are now developing VLSV using liquid propellant. The Vector Space System Inc. is launching small-sat launch vehicle, which can deliver a 65 kg payload to LEO using liquid propellant rocket using propylene and LOX. The Interstellar Technologies Inc. is launching a gas pressure-pumped liquid propellant rocket called MOMO, while the Rocket Lab Inc. developed electrically pumped liquid rocket engines. In general, liquid propellant offers the specific impulse higher the solid propellant rockets. On the other hand, the liquid propellant rockets tend to

be more complicated than solid rockets partly because the liquid propellant needs to be pressurized and pumped to the combustion chamber of rocket engines. The final price would be determined by the balance between structural complexity and increase in the specific impulse.

This can be explained in more quantitatively as follows. The launch cost of ELV mainly consists of the production cost of the launch vehicle and the propellant cost, if we could ignore the development of the system and the infrastructure maintenance of launch site. We shall start from the Tsiolkovsky rocket equation:

$$\frac{m_{\text{pay}} + m_{\text{st}}}{m_{\text{pay}} + m_{\text{st}} + m_{\text{prop}}} = \exp\left[\frac{\Delta V}{gI\text{sp}}\right] \tag{1}$$

Here, ΔV is the velocity increments required to reach the orbit, $I\text{sp}$ is the specific impulse, m_{st} is the structural mass, m_{prop} is the propellant mass, and m_{pay} is the payload mass. We shall define empty mass as $m_{\text{empty}} = m_{\text{st}} + m_{\text{prop}}$. Structural mass ratio ε is defined as $m_{\text{st}}/m_{\text{empty}}$. Furthermore, we shall assume simply that the production cost of the vehicle is proportional to m_{st} and the propellant cost is proportional to m_{prop}. Then, the launch cost, C, is proportional to m_{empty}. The constant of proportionality is defined as α. After several mathematical steps of Eq. (1), the launch cost for an unit payload mass is formulated as

$$\frac{C}{m_{\text{pay}}} = \alpha \frac{1 - \exp\left[\frac{\Delta V}{gI\text{sp}}\right]}{\exp\left[\frac{\Delta V}{gI\text{sp}}\right] - \epsilon} \tag{2}$$

From this equation, it is proved that the launch cost for a unit payload mass decreases monotonously with I_{sp}, while it decreases with ε. It is effective way to reduce the launch cost by increasing I_{sp} and reducing the vehicle mass. This theoretical result is consistent to the VSLV designs by the ventures. Moreover, in order to ensure the structural strength of VSLV, ε increases inevitably as the vehicle size is reduced, increasing the launch cost. Here, we assume the single-stage launch, while the launch cost increases with the number of stages. Unfortunately, even when liquid propellants are used, it is quite difficult to realize the single-stage launch vehicle due to the limitation of chemical rocket I_{sp} less than 460 seconds. Extreme reduction of launch cost can be attained by higher jump of I_{sp} with extremely simplified structure of the vehicle, at a single stage.

This will be attained by using laser propulsion. By using only hydrogen as propellant, I_{sp} can reach 900 seconds, which is limited by the allowable temperature limit of the engine materials, and the hydrogen temperature cannot exceed around 3000 K. The vehicle can be extremely simplified as the energy source is left on the ground. Laser propulsion can launch the payload of around 1 kg with a 1 MW laser facility. The maximum power of the available laser facility is 100 kW today. In principle, it is possible to develop a MW-class laser by bundling the fibers with the price of several tens million US dollars. Once it is developed, massive materials, though just 1 kg at a time, can be launched continuously and on demand to the orbit. The price of the 1 MW-class laser facility is almost the same level of a single launch of H-IIA rocket vehicle. Once a VSLV on demand is realized, the induction effect is expected for the technical breakthrough and the market expansion of small satellites. On the other hand, a GW-class laser facility is necessary to launch a payload of several tons at a time, which is typical launch capability of conventional launch systems. The development of such a huge laser facility will require an extremely large budget, and it would not be easy to realize in near future.

4. A new design of laser propulsion

Then, assuming that a 100-kW-class CW fiber laser is available, we shall consider how to build the LLS. At first, we need to expect the fluctuations of the laser power, the laser beam incident angle, and the cross-sectional distribution. For this reason, the heat exchanger type requires no precise optical alignment of the incident laser beam on the vehicle. Kare's concept of heat exchanger rocket is illustrated in **Figure 6**. This is similar to the microwave rocket concept illustrated by the Escape Dynamics Inc. in 2015. In principle, the nuclear thermal rocket, like NERVA, is a kind of heat exchanger rocket. The specific impulse of a thermal rocket is maximized by using propellant of minimum molecular weight, hydrogen. If the propellant temperature could reach at 3000 K, the specific impulse in vacuum becomes 900 seconds [17, 18]. Nevertheless, Kare's estimation of the proper-specific impulse is around 600 seconds. In this concept, the laser beam is irradiated and absorbed on the side surface of the vehicle fuselage, where the temperature is highest, and the propellant is heated through the heat convection on the inner surface of the fuselage. The temperature of the propellant never exceeds the temperature of the outer surface. Because the maximum temperature of the outer surface of the heat exchanger limits the maximum temperature of the propellant, the specific impulse is limited by the thermal resistance of the materials for the outer surface. Because the atmosphere includes the oxygen, the oxidation resistance is also an important issue for the outer materials. Moreover, a large amount of black-body radiation is emitted from the outer surface and is dissipated in the air as a significant factor of the energy loss. Furthermore, this type of the heat exchanger requires quite narrow flow channel to assure high heat transfer rate, and this causes the significant pressure loss of the propellant in the heat exchanger.

An alternative design of heat exchanger rocket is illustrated in **Figure 10**. We shall consider the zenith angle launch similar to Katsurayama's concept. As mentioned earlier, the zenith angle launch minimizes the effect of the atmospheric turbulence on the laser beam transmission and the complexity of the guidance and control. The vehicle introduces the laser beam of high-power density from the bottom surface of vehicle. Due to the atmospheric turbulence, the laser beam is expanded and deflected. In addition to the propulsion system of high performance (efficient and high specific impulse), precise beam pointing to a small window on the bottom surface of the vehicle is another key issue. A thrust-vectoring gimbal is assumed here for the attitude control. The pointing control and guidance are performed in a cooperative system consisting the propulsion thrust, gimbal, and laser beam optical system on the ground. The vehicle position is always informed onto the ground station. This will be done by the GPS signal from the vehicle or the optical tracking system on the ground or on orbit. On the basis of the information, the beam direction is controlled on the ground. At the same time, the exact position of the laser spot is detected on the vehicle and informed to the ground station. The beam position is adjusted from the ground, while vehicle adjusts its position transverse to the beam direction. Although more detailed analysis and design are necessary, we shall leave this issue for the future work. Before this issue, it is critical to investigate the effect of the atmospheric turbulence on the laser beam propagation through the atmosphere. As mentioned later, the high-frequency fluctuation of the laser beam direction (scintillation) should be critical when the vehicle attains the altitude higher than 10 km. Unfortunately, there is no control technique real-time correction of the scintillation today. The astronomers are taking pictures of stars at short exposure time, by catching the instantaneous image. The real-time correction of the beam direction should be based on the adaptive optics, for which we need to
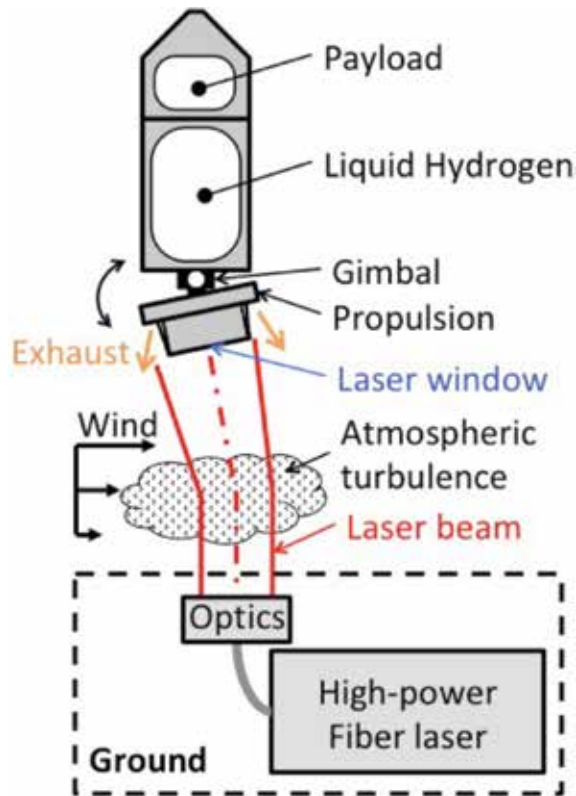
Figure 10.
Alternative LLS.

detect the atmospheric turbulence on the ray line between the ground station and the vehicle by some means. We need to develop anti-scintillation techniques in the near future. However, for the development of the launch system, we need to move forward step by step. It should be better to start from the aim to a 10 km altitude along the zenith angle trajectory. Myrabo reached at 71 m. The 10 km is a well worthful challenge. For the control and guidance techniques, before going to the cooperative control, it is realistic to accomplish more simple method of the active bream-riding flight along a vertical trajectory.

For the propulsion, we shall investigate an externally heated rocket, similar to Kare's concept, using liquid hydrogen as propellant. For the externally heated rocket, the specific impulse is limited by the thermal and oxidation resistance of the high-temperature materials, while the propellant can be selected per request. The propulsion system is illustrated in **Figure 11**. In this new concept, the inside of the engine is separated via glass window from the outside. Porous material is filed inside of the engine. The porous material absorbs the laser power introduced across the window and coverts the laser energy to the enthalpy of the hydrogen gas, which passes through the porous material. One feature of the porous heat exchanger is high rate of heat convection and low-pressure loss when using high porosity and high heat-resistance porous material like DONACARBO Felt© Osaka Gas Chemical Inc. shown on the right of **Figure 4**. Because the diameter of carbon fiber is around 10 mm, large surface area and high rate of heat convection are attainable even at high-porosity condition, which leads to the low-pressure loss. Because the heat exchanger is in a close cell filled with the hydrogen, the maximum temperature of
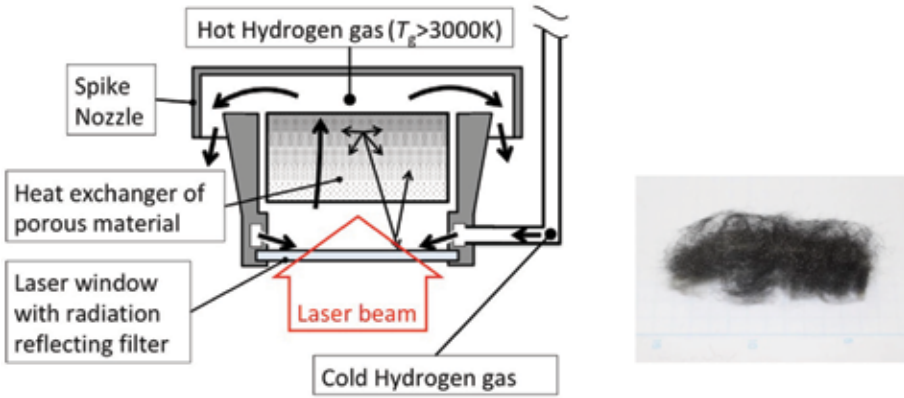
Figure 11.
Schematic of volume absorber-type laser rocket engine.
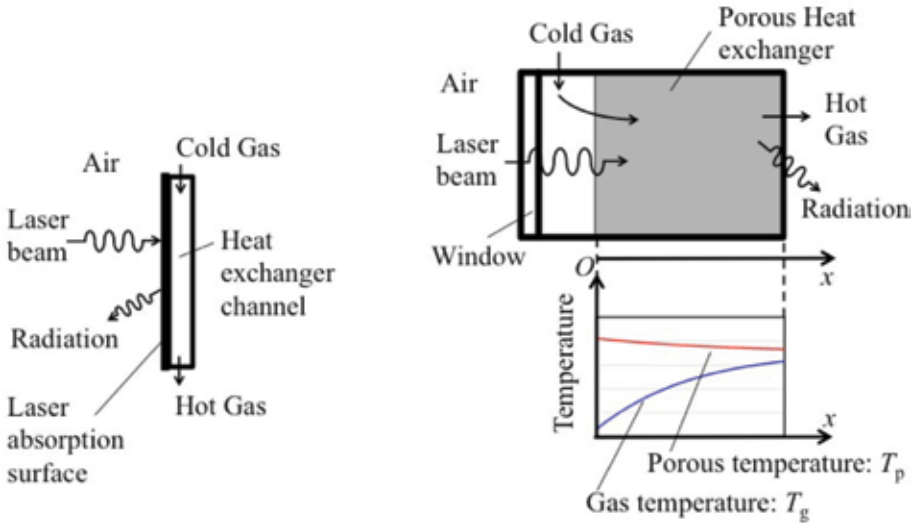
Figure 12.
Surface absorber vs. volume absorber.

the graphite materials will be more than 3000 K. (Sublimation point of graphite under anaerobic condition at one atmosphere pressure lies between 3895 and 4020 K [19].) Another feature of the porous media heat exchanger is the moderate absorption length that can be varied by the bulk size and the porosity of the porous material. This may lead to the reabsorption of the radiation from the high-temperature part of the porous material and the suppression of the energy loss due to radiation. By heating up the hydrogen gas to around 3000 K, the specific impulse in vacuum condition will reach at 900 seconds. In **Figure 12**, the "volume absorber" in the present concept is compared with the conventional Kare's concept of the so-called surface absorber. We shall consider the theoretical modeling of the volume absorber.

For the energy balance of the bulk material of porous media and the gas past the porous media, we shall consider the one-dimensional model as

$$ha_v\left(T_p - T_g\right) + \frac{dI_L}{dx} + q_{rad} = 0 \tag{3}$$

$$\rho u C_{p,g} \frac{dT_g}{dx} - h a_v (T_p - T_g) = 0 \qquad (4)$$

Here, T_p and T_g are the temperature of the bulk material of porous media and the gas, respectively. x is the coordinate inside of the porous media as illustrated in **Figure 12**. ρ is the density of gas. u is the velocity of the gas. $C_{p,g}$ is the specific heat at constant pressure of the gas. h is the volumetric interfacial heat transfer coefficient, for which a number of empirical models have been presented, and is the function of Reynolds number whose standard size is element size of the bulk material of the porous media. For the carbon fiber-based porous media, the standard size should be the diameter of the carbon fiber, which is around 10 mm. When hydrogen is used as working gas, because hydrogen has the largest mean free path among the species at certain pressure, the porous flow features high Knudsen number, and then the analysis could become complicated. The fiber size significantly affects the energy transfer processes. a_v is the specific surface area of porous medium (surface area per unit volume), and q_{rad} is light power irradiated by the black-body radiation from the element surface of porous medium, which is determined on the basis of the Stefan-Boltzmann law. I_L is the laser power density. The scattering of the laser light, the scattering and reabsorption of radiation from high-temperature part, the reflection of radiation on the interface between the porous media and the engine wall, and the heat conduction inside of the porous media have been ignored. In a real engine, the energy efficiency can be enhanced by transforming the radiation to the gas enthalpy. For the heat convection in the porous media, the local thermal equilibrium (LTE) model ($T_g = T_p$) is frequently used. On the other hand, we shall use more general local thermal nonequilibrium (LTNE) model. Actually, the temperature difference between the gas temperature, T_g, and the bulk material temperature, T_p, drives the heat convection. Note that all the variables are calculated in SI unit.

The calculation results for laser power at 100 kW and hydrogen propellant are shown in **Figure 13**. The total temperature and the energy efficiency defined as the fraction of the laser power that is converted to the gas enthalpy are plotted as functions of the incident laser power density, I_{L0}. δT is defined as $I_{L0}/\rho u C_{p,g}$, which is equal to the temperature of the gas without energy loss. On the curve of a constant δT, the mass flux ρu increases as the laser power density, I_{L0}, increases. As is clear from the figure, the energy conversion efficiency increases monotonously with I_{L0}. In order to attain 3000 K, I_{L0} should be larger than 10^9 W/m^2, which means that the 100 kW laser beam is focused on a spot of the order of 1 cm.
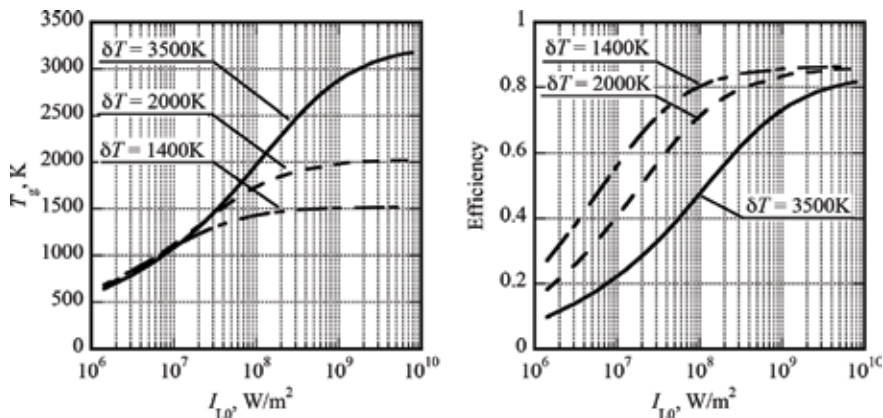

Figure 13.
Result of propulsion model.

Moreover, because the mass flux is quite large, the Reynolds number and the Mach number of the flow into the porous media become 10^2 and 0.3, respectively, which are extraordinarily large numbers for the porous flows. The heat transfer model should be further investigated experimentally.

5. Beam transmission through the atmosphere

The laser beam transmission through the atmosphere is a critical issue for the feasibility of LLS. For the LLS, the laser beam propagates from 0 to 100 km across the atmosphere to point continuously and precisely on a vehicle. The laser beam expands both due to diffraction and atmospheric turbulence. In the studies of the LLS, to the best of author's knowledge, as noted above, only Phipps et al. have considered the atmospheric beam transmission simply using the Fried parameter. Several studies considered the solar power satellite, SPS, using laser beam though there is no systematic study for the beam transmission through the atmospheric turbulence. This is partly because relevant theory has not been fully developed. The light wave propagation through the turbulent atmosphere has been studied in the field of astronomy in terms of the adaptive optics [20]. Only numerical simulations on the basis of the random phase screen method is useful for the exact analyses. To be exact, the atmospheric turbulence depends on local and instantaneous weather conditions. For a particular launch site, the numerical studies and the launch tests are necessary to verify the local effects of the atmospheric turbulence on the laser beam transmission. In some cases, it is necessary to apply the adaptive optics (AO) techniques like the large telescope like Subaru. On the other hand, qualitative discussion is also useful for typical cases, but it is not easy on the basis of numerical simulations. The analytical formula for the effects of the air turbulence on the Gaussian beam was found in 2009 [21]. What is necessary now is to know how and how much the air turbulence can affect the beam propagation. In this section, we shall discuss the impact of air turbulence on the laser beam propagation qualitatively on the basis of recent result in the research field of AO.

In order to attain high-transmission efficiency, the laser spot on the vehicle is adjusted to a proper size. The beam diffraction is regulated using the focusing optics. From the formula of diffraction limit, the minimum spot diameter of a Gaussian beam, d_s, is formulated as a function of the propagated distance z and wavelength λ, the beam quality factor at M^2, and the beam diameter on the source of beam, ϕ_0:

$$d_s = 1.2 \frac{z \lambda M^2}{\phi_0} \tag{5}$$

Substituting z = 100 km, λ = 1 μm, M^2 = 1.1 (typical value for fiber lasers), and ϕ_0 = 36 cm, we get $d_s \sim$ 37 cm. This means that a straight beam of 30 cm can be built.

The effect of the atmospheric turbulence on the laser beam propagation is categorized: (1) scintillation, (2) beam expansion, and (3) beam wonder. Scintillation is the so-called twinkle of stars. The intensity of the light varies unsteadily at high frequency. Beam expansion means the additional expansion of the beam diameter after propagating on a long path across the atmosphere. Beam wonder means the variation of the center of the laser beam axis on the cross-sectional surface. This is induced by the additional angular deflection of the laser beam due to the air turbulence. These effects are originated from the fluctuation in the deflection index distributed in the atmosphere; described using the structure constant of

deflection index $C_n{}^2$. $C_n{}^2$ is the function of the altitude, depending on the local weather condition. Since it is sensitive to the instantaneous perturbation as the passing of an aircraft, it is not easy to predict $C_n{}^2$ precisely in general cases. Here, we shall choose well-known HV 7/5 model for the altitude distribution of $C_n{}^2$ [20].

Fried parameter (or called coherence length or seeing size) r_0 is defined by integrating $C_n{}^2$ along the beam direction as

$$r_0 = \left[0.423k^2 \sec(\beta) \int_0^L C_n{}^2(z)dz\right]^{-3/5} \tag{6}$$

Here, k is the wave number of the laser beam, sec is the secant (trigonometric function), β is the zenith angle, and L is the propagation distance. When a laser beam is transmitted from the ground to space, r_0 is the maximum beam diameter on the ground for the diffraction limited focusing in space. Even when the beam diameter is larger than r_0, the spot diameter on space object is larger than the diffraction limit of r_0. Hence, it is useless to increase the beam diameter on the ground larger than r_0. Fried parameter equals to the typical size of the turbulence. Its typical value is around 10 cm for the visible light around for λ = 500 nm. Because $r_0 \propto \lambda^{1.2}$, it is around 20 cm for λ = 1 μm. For the flatness of the wave front, isoplanatic angle θ_0 is defined as

$$\theta_0 = \left[2.91k^2 \int_0^L C_n{}^2(z)z^{5/3}dz\right]^{-3/5} \tag{7}$$

The typical value for the visible light (λ = 500 nm) is 7 μrad, and considering $\theta_0 \propto \lambda^{1.2}$, typical value is 16 μrad for λ = 1 μm. In HV 7/5 model, the altitude distribution of $C_n{}^2$ is formulated as follows taking r_0 and θ_0 as major parameters:

$$C_n{}^2(z) = 5.94 \cdot 10^{-23}z^{10}e^{-z}\left(\frac{W}{27}\right) + 2.7 \cdot 10^{-16}e^{-\frac{2z}{3}} + Ae^{-10h} \tag{8}$$

Here, z is the altitude from sea level [km], and h is the altitude from the beam source [km]. When the laser beam is emitted from sea level, $z = h$ as assuming in the following. The unit of $C_n{}^2(z)$ is m$^{-2/3}$. W and A are the constants that represent the atmospheric condition, formulated using (r_0, θ_0) as

$$W = 27\sqrt{75\theta_0{}^{-5/3}\lambda^2 - 0.14} \tag{9}$$

$$A = 1.29 \cdot 10^{-12}r_0{}^{-5/3}\lambda^2 - 1.61 \cdot 10^{-13}\theta_0{}^{-5/3}\lambda^2 - 3.89 \cdot 10^{-15} \tag{10}$$

Here, the units of r_0, θ_0, and λ are cm, μrad, and μm. As shown in **Figure 14**, the typical value of $C_n{}^2$ is 10^{-15} m$^{-2/3}$ near the ground and is reduced sharply to 10^{-17} m$^{-2/3}$ at altitude of 10 km. Then, it becomes almost constant. For the laser beam propagation from the ground to the sky, the atmospheric turbulence has significant impact at altitude lower than 10 km. In the actual atmosphere, the atmospheric boundary layer, typically lower than 2 km, is quite effective to the fluctuations in the laser beam. On the other hand, the conditions in the boundary layer depend on the local landform and are time-varying even in 1 day. This complexity in atmospheric boundary layer makes $C_n{}^2$ unpredictable. According to Ref. [21], beam expansion of a Gaussian beam δw is formulated as

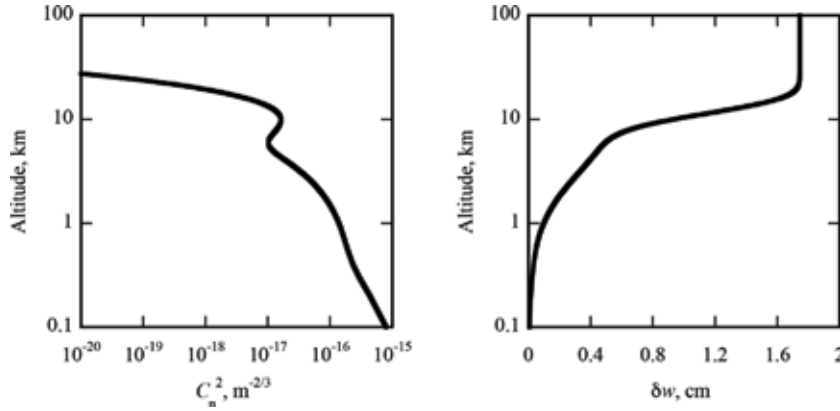$$\delta w^2 = \frac{128}{5}\left(0.545C_n{}^2(z)\right)^{6/5}k^{2/5}z^{11/5}\delta z \tag{11}$$

Figure 14.
Examples of C_n^2 and δw for λ = 1 μm, $θ_o$ = 16.1 μrad, and r_o = 23.0 cm.

λ (μm)	$φ_0$ (cm)	r_0 (cm)	$θ_0$ (μrad)	δα (μrad)	δw (cm)
0.5	10	10	7	3.0	2.0
1	10	23	16	3.0	1.7
10	10	364	254	3.0	1.1

Table 1.
Beam expansion and wondering at altitude of 100 km.

Moreover, the angular fluctuation due to the beam wondering is formulated as

$$\delta\alpha^2 = 0.364\left(\frac{\phi_0}{r_0}\right)^{5/3}\left(\frac{\lambda}{\phi_0}\right)^2 \tag{12}$$

As shown in **Figure 14**, δw saturates at the altitude around 10 km.

The results are summarized in **Table 1**. The beam diameter on the ground is assumed 10 cm. The increment of the beam diameter δw is 1.7 cm (around 17%) at the altitude of 100 km. This should be regulated using the optics on the ground. The beam wondering is around 3 μrad. This means the beam position is deflected by 30 cm at the altitude of 100 km. Because the beam diameter is 10 cm and then the size of the beam-receiving surface on the vehicle is almost same, the fluctuation of the beam location at 30 cm is quite large. This fluctuation varies typically at a frequency of 1 kHz. Without any correction to the beam wondering, the thrust cannot be generated at altitude of the order of several tens kilo-meter. On the other hand, the beam wondering should be ignorable in the demonstration of launch up to the altitude of 1 km. Both r_0 and $θ_0$ increase with λ. Consequently, although δw decreases slightly with λ, δα is constant.

6. Summary

It is clear that we need to develop a launch system of high specific impulse to expand our universe. Laser launch system (LLS) is a promising candidate that can generate the specific impulse higher than 900 seconds. As a 100-kW-class fiber laser has been developed today, actual launch to the orbit will happen in near future. In this chapter, we looked around the technical problems and tried some analyses for the propulsion performance and the atmospheric turbulence effect on

the laser beam transmission. The latter problem will become important in the near future when the laser launch vehicle can reach the altitude higher than 10 km. This problem is linked with the methodologies for the guidance and control of vehicle. Future studies will clarify the design features and technical problems of LLS in more detail.

Author details

Koichi Mori
Nagoya University, Nagoya, Japan

*Address all correspondence to: koichi.mori@mae.nagoya-u.ac.jp

IntechOpen

References

[1] Pournelle J, Nieven L. Foot Fall. New York: Del Rey, Penguin Random House; 1985

[2] Wilson RC. New York: Burning Paradise, Tor Books; 2013

[3] https://en.wikipedia.org/wiki/Breakthrough_Starshot

[4] https://en.wikipedia.org/wiki/Space-based_solar_power

[5] https://en.wikipedia.org/wiki/Laser_communication_in_space

[6] Ketsdever AD et al. Overview of advanced concepts for space access. Journal of Spacecraft and Rockets. 2010;**47**:238-250

[7] Kantrowitz A. Laser population. Astronautics and Aeronautics. 1971;**10**:74

[8] Myrabo LN. World record flights of beam-riding rocket lightcraft: Demonstration of disruptive propulsion technology. AIAA Paper 01-3798; 2001

[9] Komurasaki K, Wang B. Laser propulsion. In: Encyclopedia of Aerospace Engineering. New Jersey, USA: Wiley & Sons, Ltd, Hoboken; 2010

[10] Phipps C et al. Review: Laser-ablation propulsion. Journal of Propulsion and Power. 2010;**26**(4):609-637

[11] Tran TD, Yogo A, Nishimura H, Mori K. Impulse and mass removal rate of aluminum target by nanosecond laser ablation in a wide range of ambient pressure. Journal of Applied Physics. 2017;**122**:233304

[12] Xie C, Tran DT, Mori K. Numerical estimation of laser-ablation propulsion performance in spherical capsule. In: 31st International Symposium on Shock Waves. Nagoya, Japan. No. SBM000190; 2017

[13] Legner HH, Douglas-Hamilton DH. CW laser propulsion. Journal of Energy. 1978;**2**(2):85-94

[14] Kare JT. Laser-powered heat exchanger rocket for ground-to-orbit launch. Journal of Propulsion and Power. 1995;**11**(3):535-543

[15] Katsurayama H, Komurasaki K, Arakawa Y. A preliminary study of pulse-laser powered orbital launcher. Acta Astronautica. 2009;**65**:1032-1041

[16] Phipps CR, Reilly JP, Campbell JW. Optimum parameters for laser-launching objects into low earth orbit. Laser and Particle Beams. 2000;**18**(4):661-695

[17] Robbins WH, Finger HB. An Historical Perspective of the NERVA Nuclear Rocket Engine Technology Program. NASA Contractor Report 187154, AIAA-91-3451, Prepared fro Lewis Research Center Under Contract NAS3-25266, 1991

[18] Gabrielli RA, Herdrich G. Review of nuclear thermal propulsion systems. Progress in Aerospace Sciences. 2015;**79**:92-113

[19] Abrahamson J. Graphite sublimation temperatures, carbon arcs and crystallite erosion. Carbon. 1974;**12**(2):111-118

[20] Tyson RK. Principles of Adaptive Optics. 4th ed. Florida, USA: CRC Press, Boca Raton; 2015

[21] Ji X, Li X. Directionality of Gaussian array beam propagating in atmosphere turbulence. Journal of the Optical Society of America A. 2009;**26**(2):236-243

Hall Thruster Erosion

Andrey Vitalievich Loyan and Alona Nikolaevna Khaustova

Abstract

Hall thruster (HT) is one of the thrusters that are systematically applied in space. If to compare HT with plasma ion thrusters, it has lower lifetime and specific impulse. HT has a set of advantages, and that is why interest to this plasma thruster is high. It has relatively simple design and technology of production. HT does not require a complex power supply unit, and it is very important for spacecraft. Propulsion system on the base of HT has lower mass, simpler technology, and less time of production. One of the main HT characteristics that require improvement is the lifetime of thruster. As it is known, one of the main factors that decrease thruster lifetime is the wear of discharge chamber (DCh). With the analysis of demands to HT, it is understandable that the required lifetime is more than 10 years. So the question about lifetime of the HT is still open. This chapter presents the overview of the thruster elements lifetimes and the overview of methods of thruster erosion investigation. It shows advantages and disadvantages of optical methods of DCh erosion rate investigation. Chapter presents modified method of optical investigation. The results of HT research under various modes of operation and results of tests with different ceramic are presented.

Keywords: electric propulsion thruster, stationary plasma thruster, lifetime, discharge chamber, method diagnostics, optical emission spectroscopy, erosion rate

1. Introduction

With the increasing of number and complexity of tasks performed by modern spacecrafts, more high requirements appear for the propulsion unit (PU). Today, units based on hall thruster (HT) are one of a promising type of PU. Modern HT meets customer requirements by the following parameters: efficiency, specific impulse, and thrust price. However, the claimed thruster lifetime cannot fully meet the requirements of the technical task [1].

The common symptom of the completion of the HT's lifetime is the moment, when the elements of the magnetic system, the cathode, are bombarded by the ion flow first time, and this prose is followed by degradation of integral characteristics. To estimate the technical state of the discharge chamber (DCh) wear, the HT tests and measures of the erosion of the material are carried out [1, 2].

The problem of research of DCh wear is based on two factors. First, the maximum number of HT orders for a single customer does not exceed 10 units per year. To use the classical mathematical statistics, volumes of samples should count dozens of samples and tests should last hundreds thousands hours. To determine the HT lifetime, which is 4000 hours, it is necessary to provide tests of 130 thousand hours for 32 thrusters, which exceeds the cost of PU. The dissemination of the test results

from individual samples to a whole range of thrusters, even with one design, is unreasonable because of the lack of statistical data and high requirements for space technology.

Second, while using the reduced lifetime tests, the duration of the experiment is about 10% of the physical thruster lifetime. For example, for HT with 4000 hours of operation time, a test with a minimum base of 400 hours is required. The cost of such tests can be compared to the cost of one HT.

These factors determine the necessity of searching for new diagnostic methods of DCh wear—to increase the HT lifetime and to reduce the test duration [1–3].

Performance of the mentioned works on increase in a resource of the HT can be done in several directions:

- search for new ceramic materials;

- improvement of thruster design;

- improvement of mathematical model of thruster in order to find new ways of enhancing sustainability of the DCh to high-energy ion flow; and

- search for new ways of HT resource increasing, for instance, by means of selection of its operation mode.

The search for new materials is a direction of work that requires not only significant material but also durable time expenses; positive result will undoubtedly lead to DCh recourse increase, but will not be able to influence on characteristics of finished thrusters.

The existing mathematical models of HT allow us to simulate the process of DCh insulator wear and based on the results of calculations, with reasonable accuracy, to predict the behavior of HT erosion. Despite this, leading HT developers are inclined to believe that trusted quantitative data can only be obtained experimentally on the basis of long-term resource tests.

The results of the analysis of the state of wear research of the DCh HT show that today there is no possibility to make a list of the main guaranteed recommendations according to which it would be possible to develop a design of the thruster with a lifetime up to two times higher than existing analogues; therefore, HT improvement works are carried out in all of the previously mentioned areas.

This chapter presents the results of research of the HT DCh edge wear at various operating modes (with different ratios of coil currents at stable values of the discharge voltage and mass flow rate).

The research results of low-power HT with different materials of ceramic insulators are presented.

2. Possible Hall thruster lifetime limiting elements

2.1 Main components and operating principle of the HT

HT is a plasma thruster in which thrust is created by propellant ions, formed and accelerated in a discharge in crossed electric and magnetic fields.

In the traditional version, HT consists of two main nodes—the cathode and anode blocks (**Figure 1**). The cathode (1) is performed according to the scheme of a hollow cathode, located on the side of the anode block and is a source of electrons. The purpose of the cathode is to ensure the thruster ignition, maintains its normal operation,
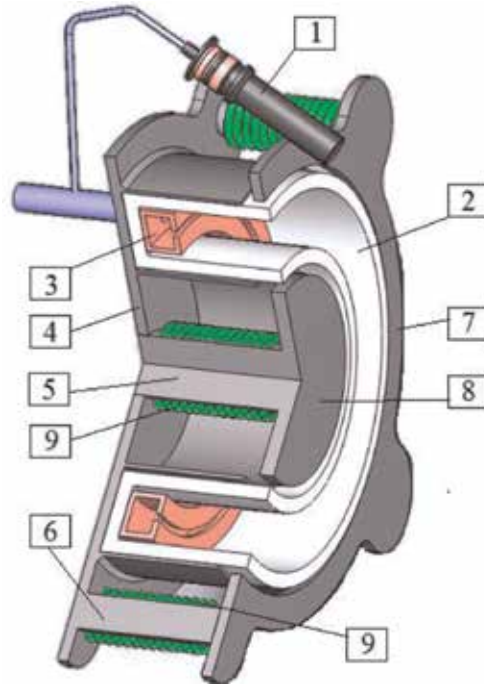
Figure 1.
Principle scheme of the HT: 1—cathode-neutralizer; 2—discharge chamber; 3—anode; 4—magnetic part;
5 and 6—inner and outer cores; 7 and 8—outer and inner poles; 9 and 10—inner and outer coils.

and also neutralizes the charge of the plume flowing out of the thruster. The anode block consists of a magnetic system and accelerating channel (2) with an anode (3). The magnetic system (MS) includes: magnetic part (4), inner core (5) and an outer core (6), an outer pole (7) and an internal pole (8), as well as a coils (9 and 10). The MS is constructed in such a way that a radial magnetic field is formed in the discharge channel (DCh) located in the gap between the magnetic poles. DCh is limited by coaxial cylindrical walls of dielectric material, in the base of which anode is located, which also performs the function of supplying gas to the thruster channel [4].

The thruster works as follows: the propellant through the anode comes via the DCh. Discharge voltage is applied between the cathode and the anode. Under the action of electric field, electrons begin to move from the cathode to the anode and enter the crossed electric and magnetic fields. The magnitude of the magnetic field induction in the DCh is chosen such that the Larmor radii of the electrons r_e and the ions r_i satisfy the condition $r_e \ll L \ll r_i$, where L is the length of the DCh.

Under these conditions, the electron motion is performed in the azimuthal direction, and in the direction of the anode, displacement occurs due to collisions with neutral and charged particles, with the walls of the DCh, and also because of the plasma oscillations.

During the operation of the thruster, the electrons moving to the anode ionize the atoms of the propellant, and the ions that are formed are accelerated along the electric field, creating a reactive thrust. At the thruster exit, the ion flow is neutralized by electron flow created by the cathode.

2.2 Discharge chamber lifetime

In the region of the DCh exit, an ion stream is produced, and some of which is directed not along the axis of the thruster, but on the wall of the DCh. In the plasma

of the HT, the ion flux reaches an energy level of tens, hundreds, and thousands of electron volts. Upon impact against the surface, the ions begin to "dissipate" it, that is, knock out one or more atoms (physical sputtering—erosion), ions (emission), electrons (emission), or fragments of molecules (chemical sputtering). Bombarding ions can acquire electrons on the surface and be reflected from it in the form of neutral atoms, the neutralization process. Ions can be bound to the sample surface (adsorbed). The listed processes are accompanied by electromagnetic radiation from ultraviolet to X-ray ranges.

The ion energy greatly exceeds the covalent bond energy of the particles in the layer and the weak Van der Waals and electrostatic interaction between the layers, which leads to the appearance of various types of physical sputtering, which are divided into several types: primary direct knockout, sputtering by linear cascades, and thermal peaks [5].

In the first case, the ion transmits to atoms enough amount of energy, so that atoms are able to leave the material after a small number of collisions. In two other sputtering modes, the amount of transmitted energy is sufficient to excite the displacement from the equilibrium position of whole groups of atoms that overcome the surface energy barrier and leave the wall of the DCh. This can explain the occurrence of zones of normal and abnormal erosion on the surface of ceramic inserts.

The main mass of sputtering product of the DCh material is neutral atoms, and the fraction of ions does not exceed 1% [6]. Ionized erosion products are recorded only at high values of the discharge voltage; the number of emitted ions of the material is by 2–4 orders of magnitude less than the number of emitted atoms.

The result of the erosion process can be traced visually after the tests. **Figure 2** is the photo of new 0.1 kW power hall thruster that is developed by the Scientific-Technological Center of Space Power and Engines (STC SPE) of National Aerospace University named after N. Ye. Zhukovsky "Kharkiv Aviation Institute," Ukraine. **Figure 3** presents the ceramic wall of the HT 0.1 kW after 92 hours of operation. There are areas of normal and abnormal erosion.
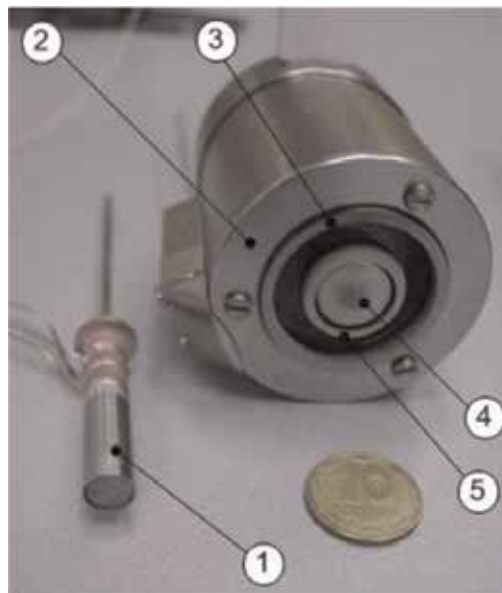
Figure 2.
Photo of the new hall thruster of 0.1 kW power and cathode: 1—cathode-neutralizer; 2—magnetic pole; 3—outer ceramic; 4–inner poles; 5–inner ceramic.
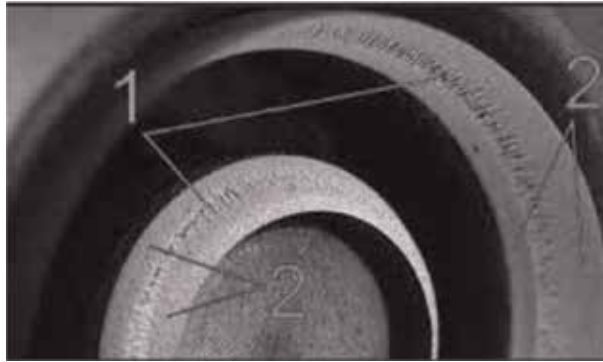
Figure 3.
Erosion belt of the thruster of 0.1 kW after 92 hours of operation: 1—abnormal erosion; 2—normal erosion.

The width of the erosion belt depends not only on the thruster design, the field distribution, but also on the DCh material and the choice of the thruster operation mode.

Resistance to the wear of the DCh wall material depends on more than 20 parameters, the most important of which are composition, density, porosity, and manufacturing technology [7].

2.3 The cathode lifetime (ignition electrode and emitter)

In spite of the fact that the cathode neutralizer is located in the zone with the minimal influence of the ion flow (i.e., outside the thruster plume), the fraction of ions with high-energy values is present in the near-cathode region. This leads to a gradual sputtering of the cathode block (**Figure 4**).

The most closely located to the DCh section element of the cathode is the ignition electrode (IE) (**Figure 6**). The goal of IE is to create an initial discharge between the emitter and the IE. Next, the main discharge is ignited between the anode and cathode blocks.

Analysis of the results of long-term lifetime tests carried out in the EDB Fakel Kaliningrad [9] showed that the volume of IE material sputtering is linear until the
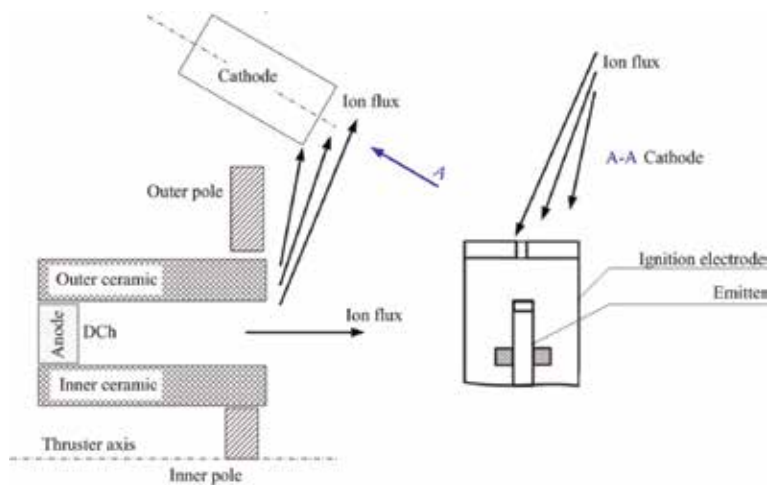
Figure 4.
Position of cathode according to the DCh exit.

length of the outer insulator exceeds the length of the outer pole tip. As the length of the outer ceramic insert decreases, the insulator ceases to be a barrier between the plasma plume and the cathode block, and thereby opens both the pole tip and the cathode for ion flow influence. The results of long tests of about 3000 hours or more showed that even with full wear of the end part of the IE, it fully performs the function of starting the thruster. According to the forecast, the IE lifetime is more than 10,000 h.

The cathode emitter lifetime is determined by the rate of material loss of its emission part. The statistical data show that during the time of the cathode block lifetime tests with duration of more than 8000 hours, the emitter volume loss is less than 8%. The predicted emitter lifetime is not less than 15,000 hours [15].

2.4 Hall thruster magnetic system lifetime

HT magnetic system materials possess low sputtering coefficients as compared to ceramic insulators of DCh. The design of discharge chamber exit of the thruster is designed in such a way that the edges of both the outer ceramic insert and the inner ceramic insert block the ion flow to the magnetic poles.

Obviously, despite the applied constructional solutions, there is a weak flux of high-energy ions in this region. However, the material mass leakage is negligible. The results of experiments on the determination of the initial stage of materials of the magnetic system wear at different thicknesses of the walls of the DCh show that with a proper selection of the geometry of the DCh walls, a lifetime of a magnetic system of more than 15,000 hours can be achieved for a 1.35 kW HT model [8].

The results of long-term HT lifetime tests show that at first, DCh edges are susceptible to ion bombardment discharged, and only after the total sputtering of the edges of the insulators, magnetic system elements and cathode block are beginning to significantly erode. Hence, one of the most critical elements of HT from the point of view of the lifetime is the edge of the DCh insulators.

3. Overview of methods of Hall thruster erosion measurements

A number of direct and indirect methods have been developed to study the rate of erosion of the HT DCh, each of which has unique methodological differences.

3.1 Direct methods

During the thruster operation, the profile of the edges gradually changes due to the loss of the weight of the DCh insulators. If the design of the thruster allows rapid extraction of ceramic inserts from the HT anodic block quickly and without causing defects, then the mass change control (weighting methods) is carried out, for example, using laboratory scales (WA-21).

For the initial masses of outer and inner ceramics m_{OC_0} and m_{IC_0}, the mass of the insulator is taken just after its manufacturing. Further tests are carried out with the HT unchanged operating mode. The time base of the experiment is divided into several stages, for example, 10–50 hours each, depending on the thruster power and the rate of erosion. After the end of each stage of the tests, the insulators are removed from the anode block, and their mass, mn1 and mv1, are measured. Mass loss rate, mg/h, of the sample is determined by calculating the difference between the initial and measured masses and dividing it into a time test base [9].

In order to control the radial erosion, mm/h, measuring instrumental microscopes are used.

Using direct methods, data on the rate of erosion of ceramic units of measurement—mm/h or mg/h are received. The error in determining the wear depends on the stability of the thruster operation and the accuracy of the measuring equipment. There is no need for a sophisticated calculation method.

3.2 Indirect methods

In order to be able to monitor the erosion rate directly during thruster operation, there are a number of indirect measurement methods. These include optical methods and special methods [10].

3.2.1 Method of quartz crystal

The principle of the method is to trap the sputtering products of ceramic insulators on a quartz crystal (**Figure 5**).

The design of the recording device is designed in such a way that the ionic component of the plume would not be able to overcome the potential barrier created by the electric field applied to the housing. Permanent magnets are used to trap electron component of the flow. Magnets characteristics are selected depending on the thruster plume. The quartz crystal is attached to the resonating circuit. During the experiment, the frequency of the loop oscillation is monitored, which changes when the film forms on the surface of the crystal from the deposited neutral atoms—the erosion products of the thruster material.

Analysis of the data obtained using this method showed good alignment of results and the method of optical emission spectroscopy (OES).

3.2.2 Laser-induced fluorescence

Laser-induced fluorescence (LIF) has also been used for several decades to study the fluorescence spectra of HT plasma [9].

LIF is considered a highly sensitive method [8], since the excitation rate is independent of the plasma parameters, with stable operation of the thruster, and there is a possibility to adjust the equipment to obtain maximum sensitivity for each
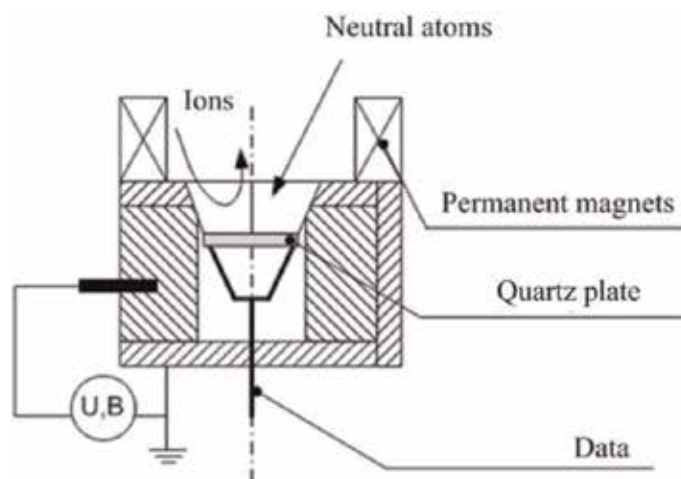
Figure 5.
The device for recording the mass loss of the DCh insulators by the quartz crystal method.

component under study. However, the need to install and set a large number of measuring equipment, the need to reconfigure the laser to investigate various components of the spectrum, critically limits the scope of the method [9].

3.2.3 Mass spectrometry

One of the methods for recording HT sputtering products is the mass spectrometry method [8]. Modern mass spectrometers have high resolution and can be used with all kinds of particles in different states of excitation and different concentrations of the sample under study.

Despite the significant advantages of modern mass spectrometers, high sensitivity, in comparison with other optical methods, unambiguous identification of particles, and a large operating range of masses, they have a number of disadvantages. First, mass spectrometers are complex instruments both in operation and in maintenance. Second, modern mass spectrometers are an extremely expensive type of equipment, the cost of which is comparable to the cost of manufacturing several HTs.

3.2.4 Optical emission spectroscopy

The principle of the method of optical emission spectroscopy consists in recording the emission spectrum of the thruster sputtering products and recalculating the intensities of the spectral lines in the erosion rate [9]. Advantages of the method, namely contactless, relatively simple procedure for processing experimental data, and relatively simple technical organization of measuring equipment, led to the extensive use of OES as one of the main diagnostic tools in the field of research of the technical state of HT.

The requirements to the method of HT insulators edges erosion rate are next:

- non-intrusive, estimation of erosion without any contact with thruster itself or plasma plume;

- technically simple;

- short-term preparation time of measuring equipment;

- no need for multiple calibration and adjustment of measuring equipment;

- possibility of multiple use of recording sensors;

- the ability to do measurements during the thruster operation;

- short-term procedure of experimental data processing;

- measurement of the external and internal insulators erosion rate separately.

Methodological requirements are as follows: relatively high measurement accuracy and unambiguous interpretation of the results.

The analysis of the methods for diagnosing the rate of erosion of the spraying products of the edge edges of HT insulators showed that in order to obtain qualitative measurement results, two diagnostic methods should be used throughout the thruster test cycle: OES and measurements by direct methods.

4. Detailed description of the optical emission spectroscopy (OES) method. OES development: method of the optical emission spectroscopy with the scanning of thruster plasma through collimator (OESSC)

4.1 Basic scheme and principle of measurements with the OES method

The basic scheme of the OES method is shown in **Figure 6**. Radiation of the plasma of the thruster through the inspection flange and the lens by means of an optical cable is transferred to a spectrometer where the spectrum is decomposed. Further, the signal is transmitted to the computer and output as a dependence of the intensity of the spectral line on the wavelength. As a rule, the inspection flange of a vacuum chamber is made of quartz glass of KU-1 type with a low absorption coefficient of radiation in a wide range of wavelengths.

It is obvious from **Figure 8** that when using the basic scheme of the OES method, it is not possible to register radiation separately from each edge of the DCh ceramic.

4.2 Basic scheme and principle of measurements with the OESSC method

For the spectral measurements from small regions of the plasma radiation of the thruster, the OES method experimental scheme was modified. From the OES measurement scheme, the collecting lens was removed, and the optical cable was installed into the vacuum chamber at the minimum possible distance from the DCh cut. A collimator was installed on the fiber optic cable (**Figure 7**). Collimator is a device that geometrically reduces the divergence angle of the optical fiber. For a standard optical cable, the divergence angle is equal to 25.4°. For the developed optical receiver, which consists of a collimator and a cable, the divergence angle was 4.5°.
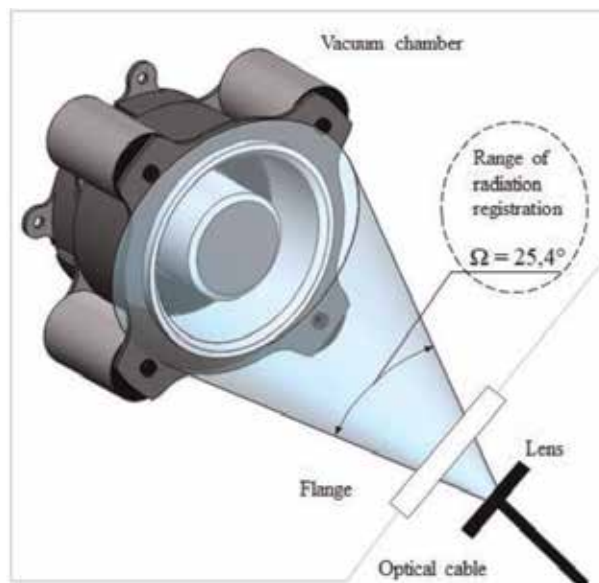
Figure 6.
The scheme of measurements of the rate of erosion by the OES method.
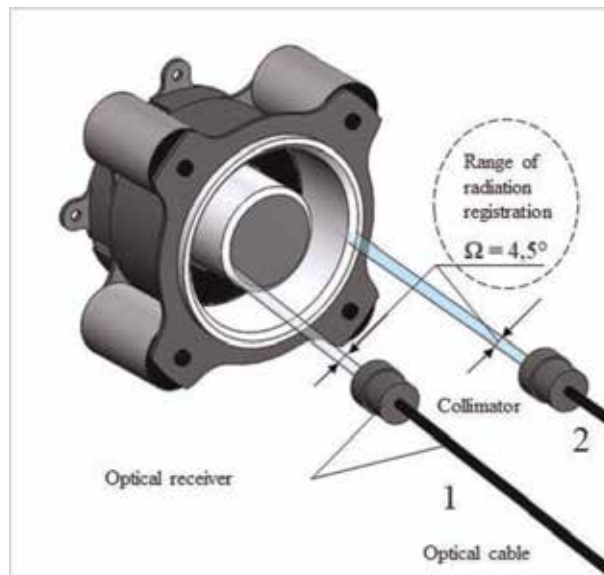
Figure 7.
Scheme of measurements of the erosion rate by the OESSC method: 1—position of measurements of "inner ceramic"; and 2—position of measurements of "inner ceramic" and "outer ceramic."

It is also possible to scan radiation from different regions of the DCh by installing a registration element on a coordinate platform. According to the presented scheme, the improved method of OES was called the method of optical emission spectroscopy with scanning of the plasma radiation of the thruster through a collimator (OESSC).

The above scheme of measurements by the OESSC method has a number of advantages:

- the possibility to obtain data on the wear rate of insulators from each of the ceramic inserts separately during the tests of the thruster;

- the ability to carry out measurements of the entrainment of the material separately of different parts of the thruster magnetic system during the tests;

- possibility to register the degree of wear of ceramics in the azimuth direction;

- nonintrusive—no contact of measuring equipment with thruster plasma, which may lead to change thruster operation mode and the change of the plasma parameters;

- a simple procedure of experimental data processing;

- absence of complicated procedures for calibration and adjustment of measuring equipment; and

- the possibility to get erosion data at different thruster operating modes, namely at different voltages, mass flow rates, and coil currents [11].

One of the method disadvantages is the installation of a sensitive optical cable in a vacuum chamber, which leads to the dusting of the fiber with the products of

thruster erosion. However, this problem was solved by installing of the quartz glass protective screens to the sensitive element of the optical fiber [12].

4.3 Processing of the spectral measurement results

The results of spectral measurements of two thrusters with different materials of ceramic insulators BN and BN + SiO$_2$ are presented in **Figure 8**. As can be seen in the UV-range, boron lines with a wavelength of 249.66 and 249.77 nm are presented on the spectra of both thrusters. These boron lines that are suitable for qualitative analysis are well recorded. Silicon lines are presented on the thruster with BN + SiO$_2$ ceramic and absent on the thruster with BN ceramic. The intensities of silicon line in UV-range are relatively high, so these lines can be used for the quantitative analysis.

Known method of erosion rate computation based on the thruster DCh radiation spectrum measurements has a comparable character. It means that, for example, computational data can give assessment of erosion rate differ at different thruster operational modes or how the erosion rate changes in time. OES equation does not describe how the optical fiber position and DCh erosion area influence the registered emission flow. These data are necessary for the computation of erosion rate from different DCh walls.

That is why for the OESSC method, next calculation expression is used

$$Er = I^B_{249.77} \frac{R_B{}^2}{V_B} \frac{I^{Xe}_{828.01}}{I^{Xe+m}_{484.43}} \qquad (1)$$

where Er is the erosion rate of the material; $I^B_{249.77}$ is the lighting of the optical cable by the boron atoms on the wavelength 249.77 nm; $I^{Xe+m}_{484.43}$ is the lighting of the optical cable by the xenon metastable ions on the wavelength 484.43 nm; $I^{Xe}_{828.01}$ is the lighting of the optical cable by the xenon atoms on the wavelength 828.01 nm; R$_B$ is the distance from the source to the radiation detector, m.; and V$_B$ is the amount of radiation from DCh wear products, m^3.

This expression is used for defining the erosion rate from different parts of the DCh.
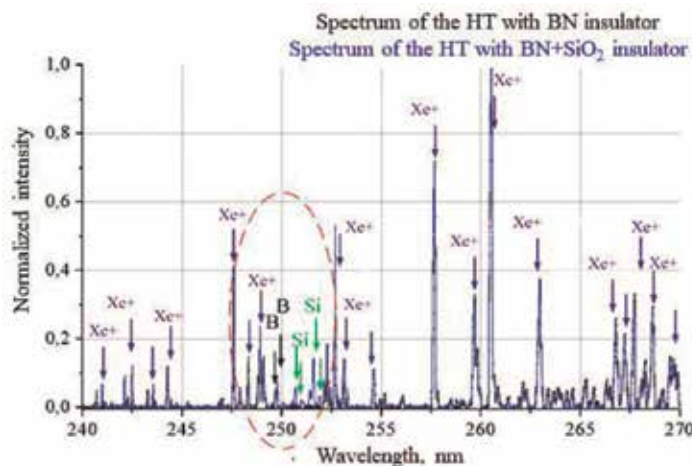
Figure 8.
Spectrum in the UV-range 240–270 nm: black—HT with BN insulator; blue—HT with BN + SiO$_2$ insulator.

5. OES studies of plasma propulsion systems of 100 W power

5.1 OES test equipment and its adjustment

For the purpose of preliminary studies on the influence of the modes of operation of the HT on its erosion characteristics for measuring the spectra of optical radiation of the plasma plume of the 0.1 kW HT, an experimental installation was established, and the scheme of which is shown in **Figure 9**. The radiation emitted by the plasma (1) 0.1 kW HT, through a quartz window (2) (diameter—40 mm and thickness—5 mm), was observed with the help of a device for measuring the spectrum located outside the camera. The angle of observation of the plasma plume at the cut of the thruster was 60° relative to the chamber axis. With 10 cm of focusing lens (3), the radiation is collected and focused on a light conductive fiber (4) with a diameter of 1 mm. The distance between the plasma plume and the lens was about 80 cm. The end of the fiber is connected by a special adapter with the inlet of the spectrometer (5). A lens with a focal length of 10 cm gave an approximately 9× magnification. With an optical fiber with a diameter of 1 mm, the spatial resolution was about 9 mm in diameter. Thus, the installation captured most of the plasma jet in the thruster channel and its exit.

The end of the optical cable through a special adapter connects to the input port of the spectrometer USB2000. This mini spectrometer, manufactured by Ocean Optics (USA), was kindly provided by Laboratoire de Physique des Gaz et des Plasmas [13]. It was used to cover the considered range with a resolution that is sufficient to distinguish optical lines. Moreover, its weight (600 g), dimensions (15 × 11 × 5 cm), and power consumption (100 mA) make it an excellent candidate for the use in summer experiments to study the erosion of ceramics and the optical spectrum of the plasma plume of the thruster (**Figure 9**).

The light entering the spectrometer is refracted by a fixed dispersing prism and is directed to the charge coupled device (CCD) line with 2048 elements. So, in one shot, this spectrometer gives a spectrum of wavelengths of 380–830 nm with a resolution of 0.2–0.22 nm. The spectrometer is connected to the laptop through the USB interface. The computer controls the parameters of the spectrometer USB2000
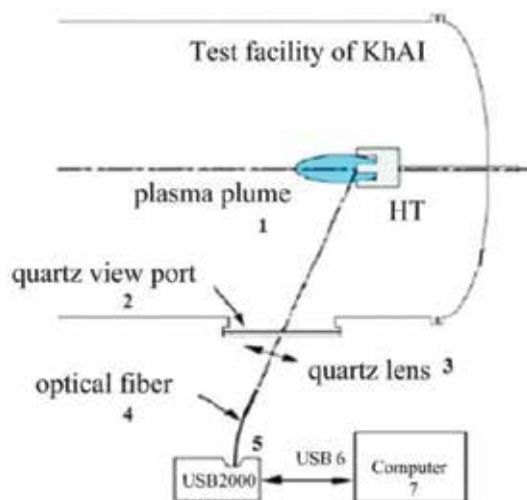
Figure 9.
Experimental equipment: HT—Hall thruster; 1—plasma plume; 2—quartz view port; 3—quartz lens; 4—optical fiber; 5—spectrometer USB-2000; 6—USB connection cable; and 7—computer.

through the computer, and the graphical interface allows you to get a spectral image that can be saved as a text file with data.

Such a measuring spectrometric system is quite user-friendly, promptly provides information about the controlled spectrum, and thanks to a numerical representation, which allows us to conveniently store information and compare it with another that was previously registered.

5.2 OES studies of the HT erosion at different operation modes

Together with the Laboratoire de Physique des Gaz et des Plasmas, Université Paris, Laboratoire d'Analyse Spectroscopique et d'Energétique des Plasmas, Université d'Orléans, and Laboratoire d'Aérothermique, the 0.1 W HT optical (spectral) tests were conducted to determine the effect of the regime of the thruster on its erosion characteristics [13]. Measurements were provided on the test facility as shown in **Figure 10**. Experimental parameters, discharge voltage (Ud) from 200 to 300 V in a step of 20 V, and also the current on the solenoid of the magnetic system of the thruster varied in the range of 1.5–3.0 A. All measurements were made at two values of xenon consumption: 0.20 and 0.25 mg/s.

In calculating of this parameter, the power of the solenoid was taken into account, but was neglected by the mass flow of xenon through the cathode. The maximum value of the efficiency (0.353) of HT during this experiment was obtained at a discharge voltage of 300 V and a mass flow of xenon 0.25 mg/s.

Xe I (828.01 nm), Xe II (484.43 nm), and Al I (396.152 nm) lines were distinguished for the analysis of the level of erosion of the stationary plasma thruster with ceramics from the ABN. These three lines made it possible to analyze the rate of erosion. This analysis was conducted with Laboratoire d'Analyze Spectroscopique et d'Energétique des Plasmas, Université d'Orléans, and its results are published in the materials of the international conference [14].

The Xe II xenon ion emission occurs due to the transition from the wavelength of 484.43 nm from the initial level $5p^4\left(D_{7/2}^0\right)6s - 5p^5\left(^2P_{3/2}^0\right)6p$ of 14.10 eV (80118.962 cm^{-1}) to the level 11.54 eV (68045.156 cm^{-1}). The upper level $5p^4\left(D_{7/2}^0\right)6s$ is basically two metastable states Xe$^+$ $5d^4D_{7/2}$ and $5d^4F_{7/2}$.
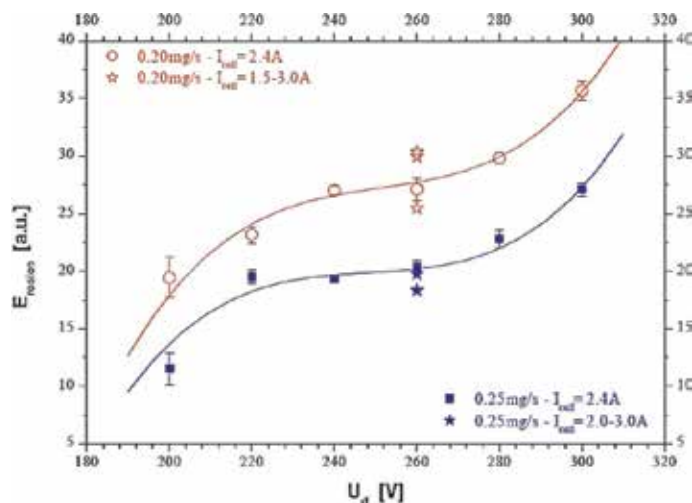
Figure 10.
Dependence of the erosion from the discharge voltage.

The two lines for aluminum are close to the transition $3s^23p - 3s^24s$ to the emission level of 3.14 eV (25347.756 cm^{-1}): the first one is 394.40 nm and the other one is 396.15 nm. Second quasi-resonance line is used. This line Al I has an amplitude of light oscillations and is located near the lines Xe II. The spectrometer should be able to isolate this line from the set of other lines of Xenon plasma emission. To determine the exact value of the AlI line 396.15 nm, a numerical method of data approximation was used for Gauss's multi-profile profile. The radiation level is also occupied by electrons excited from their ground state $\left(2P_{1/2}^0\right)$ [15].

The erosion of the thruster ceramics was determined from the ratio of the intensity of the lines

$$E_{rosion} = \frac{I(AlI, 396\ nm) \cdot I(XeI, 828\ nm)}{I(XeII, 484\ nm)}. \tag{2}$$

where intensities were determined as:

$$I_{Al}(396\ nm) \propto n_{Al} \cdot n_e \cdot k_e^{Al},\ I_{Xe}(828\ nm) \propto n_{Xe} \cdot n_e \cdot k_e^{Xe},\ I_{Xe^{+m}}(484\ nm) \propto n_{Xe^{+m}} \cdot n_e \cdot k_e^{Xe^{+m}} \tag{3}$$

where n_{Al}, n_{Xe}, $n_{Xe^{+m}}$—metastable aluminum densities, neutral and ionized xenon, respectively, and k_e^{Al}, k_e^{Xe}, $k_e^{Xe^{+m}}$—electronic excitation coefficient for the corresponding upper state. The ratio of the intensity of the lines is used to determine the concentration of aluminum.

$$E_{rosion} = \frac{I(AlI, 396\ nm) \cdot I(XeI, 828\ nm)}{I(XeII, 484\ nm)} \propto \frac{n_{Al} \cdot n_e \cdot k_e^{Al} \cdot n_{Xe} \cdot n_e \cdot k_e^{Xe}}{n_{Xe^{+m}} \cdot n_e \cdot k_e^{Xe^{+m}}}. \tag{4}$$

Applying an actinometric hypothesis, we obtain that the density of ionic metastable is proportional to the concentration of ions, reducing the value k_e^{Al} and $k_e^{Xe^{+m}}$ because of the equivalence of energy change (several eV), and this equation takes the form:

$$E_{rosion} \propto \frac{n_{Al} \cdot n_e \cdot k_e^{Al} \cdot n_{Xe} \cdot n_e \cdot k_e^{Xe}}{n_{Xe^{+m}} \cdot n_e^2 \cdot k^{Xe+} \cdot k_e^{Xe^{+m}}} \propto n_{Al}. \tag{5}$$
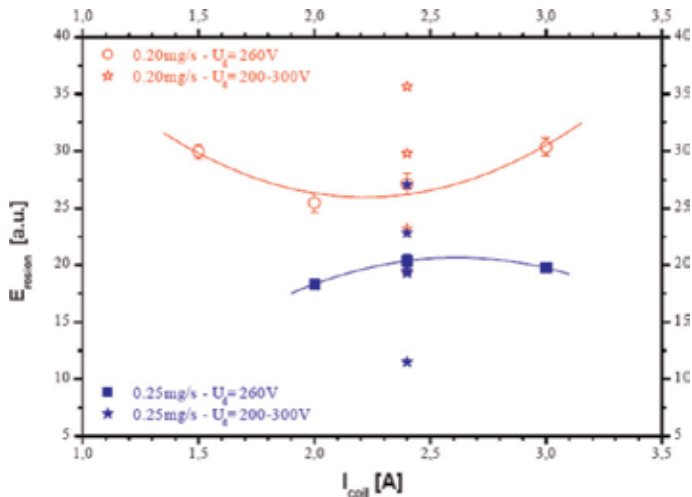
Figure 11.
Dependence of the erosion from the coil current.

To understand the behavior of the erosion in the regimes of thruster that were not measured, the experimental data were approximated by the polynomial dependence (**Figures 10** and **11**).

Figure 11 shows the dependence of the erosion on the coil current for a constant discharge voltage of 260 V and for two xenon mass flow (0.20 and 0.25 mg/s).

6. Experiment investigation of HT erosion with the OESSC and method of radial erosion measurements

As it was told, before OESSC method was developed to provide measurements of the HT erosion of outer and inner ceramics separately during thruster test was not possible for OES method. In this section, the results of the experimental investigation of two erosion measurements methods are presented: direct measurements radial erosion and OESSC method.

6.1 The algorithm of the OESSC method

In the Scientific-Technological Center of Space Power and Engines (STC SPE) of National Aerospace University named after N. Ye. Zhukovsky "Kharkiv Aviation Institute," Ukraine, 1.35 kW thruster was tested to determine the dependence of the DCh edges erosion parameters from the ratio of the magnetic system coil currents. The thruster was tested with a ceramic BN.

Algorithm of the diagnostics by OESSC method consists of several steps.

1. Maintenance of the experimental equipment (**Figure 12**).

Measuring equipment of the OESSC method consists of a block of high-resolution spectrometers for recording the radiation of HT in the range with the wavelength of 240–830 nm and two-coordinate platform for moving the optical receiver and the unit for protecting the optical fiber from dust.

2. Launch of the thruster and stabilization of the erosion parameters.

3. Measurement of the radiation spectra for each of the insulators and calculation of the erosion rate from the formula (6).

4. Repeat the procedure of spectrum measurements for each of the DCh ceramic inserts at different ratios of the thruster coil currents.
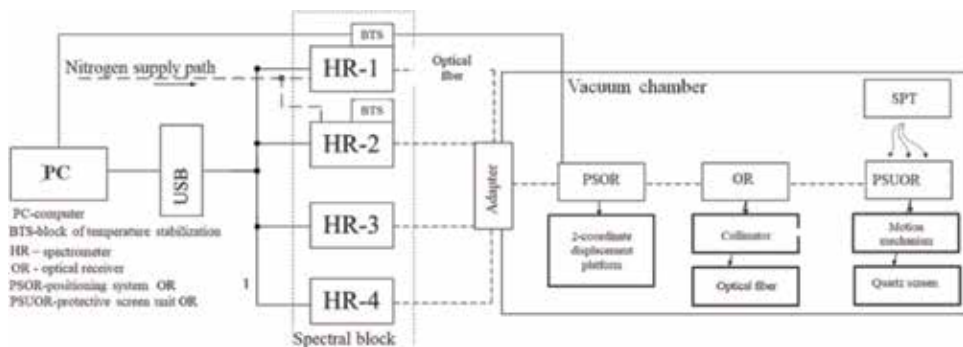
Figure 12.
Measuring equipment of the OESSC method.

5. Comparison of the erosion rate of insulators in different modes of HT.

The ratio of the erosion rates of edges obtained by the OESSC method (ΔEr) was determined like:

$$\Delta Er = \frac{Er_{\text{inner\_ceramic}} - Er_{\text{outer\_ceramic}}}{Er_{\text{inner\_ceramic}}} \cdot 100\% \quad (\text{if } Er_{\text{inner\_ceramic}} > Er_{\text{outer\_ceramic}}) \, or$$

$$\Delta Er = \frac{Er_{\text{outer\_ceramic}} - Er_{\text{inner\_ceramic}}}{Er_{\text{outer\_ceramic}}} \cdot 100\% (\text{if } Er_{\text{outer\_ceramic}} > Er_{\text{inner\_ceramic}})$$

(6)

6. Development of recommendations regarding the optimal operating mode with the maximum lifetime of the thruster DCh edges.

6.2 The method of the radial erosion measurements

After taking measurements by the OESSC method and selecting the operating mode, the thruster is tested on a time base of 50 hours, and measurements of radial erosion by a direct method are performed (**Figure 13** and **Table 1**). As a basis for measuring the insulator edge thickness, the outer diameter of the outer insulator and the inner diameter of the inner insulator were chosen.

Measurements are provided with the help of an instrumental measuring microscope with an error of less than 0.0005 mm. To eliminate errors in the installation of the DCh relative to the microscope, each measured position is photographed.

Radial erosion is defined as the difference between the coordinates of the edges of the insulators before and after the thruster operation.

$$E_{RAD\_OUT} = e_{OUT\_INITIAL} - e_{OUT\_FINAL}$$
$$E_{RAD\_IN} = e_{IN\_INITIAL} - e_{IN\_FINAL}$$

(7)

where E_{RAD_OUT} and E_{RAD_IN} are changes in thickness of the edges of the external and internal insulators after the thruster tests, mm.

The radial erosion rate is defined as:

$$V_{RAD\_OUT} = \frac{E_{RAD\_OUT}}{t_N}, \quad V_{RAD\_IN} = \frac{E_{RAD\_IN}}{t_N},$$

(8)

where V_{RAD_OUT} and V_{RAD_IN}—radial erosion rate of outer and inner insulators, mm/h; t_N—duration of the thruster test phase, h; and N—thruster test stage number.
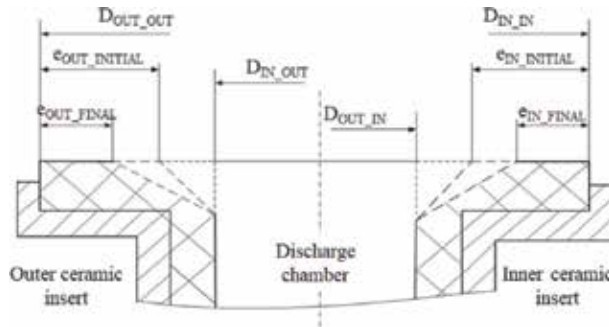
Figure 13.
Scheme of radial erosion measurements.

D_{IN_OUT}	Inner diameter of outer ceramic
D_{OUT_OUT}	Outer diameter of outer ceramic
D_{OUT_IN}	Outer diameter of inner ceramic
D_{IN_IN}	Inner diameter of inner ceramic
$e_{OUT\_INITIAL}$	Thickness of outer ceramic before the experiment
e_{OUT_FINAL}	Thickness of outer ceramic after the experiment
$e_{IN\_INITIAL}$	Thickness of inner ceramic before the experiment
e_{IN_FINAL}	Thickness of inner ceramic after the experiment

Table 1.
*Symbol definitions of **Figure 14**.*

Comparison of erosion rates of external and internal insulators was carried out by the following expression:

$$\Delta V_R = \frac{V_{RAD\_\max} - V_{RAD\_\min}}{V_{RAD\_\max}} \cdot 100\%, \tag{9}$$

where V_{RAD_max}—erosion of the insulator for which the wear is greater, mm/h; V_{RAD_min}—erosion of the insulator for which the wear is lower, mm/h.

Results of the erosion measurements with direct methods are presented in **Table 2**.

Thruster operation modes: I—mode with the lowest discharge current, current of inner coil—5 A, and current of outer coil—5 A.

As it is easy to see from the results on the mode with the lowest discharge current, erosion of ceramic walls is not uniform.

6.3 Comparison of results accepted by the OESSC method and direct radial erosion measurements

Figure 14 shows the results of the erosion rate measurements by the OESSC method. It was found that in the operating mode of the thruster with the minimum discharge current (mode I), the difference in the erosion rate of insulators was about 32%, which corresponded to the data obtained with direct measurements. After diagnostics and comparing the irregularity of erosion in 25 regimes, it was found that at the operating mode II, the difference in the erosion rate of the edges does not exceed 0.3%. The results were confirmed in subsequent tests and measurements by a direct method. The time spent on the study of the thruster DCh wear by the OESSC method on 25 operating modes, taking into account the expectation of the time for stabilizing the erosion rate, was 7 hours, which made it possible to reduce significantly the search for optimal current of the coils of the magnetic system from the point of view of uniform wear of the edges of the insulators (**Figure 14**).

# Thruster operation mode	I
Ratio of erosion rates of insulators	ΔV_R, %
Direct method	33

Table 2.
Experimental results with the direct methods.
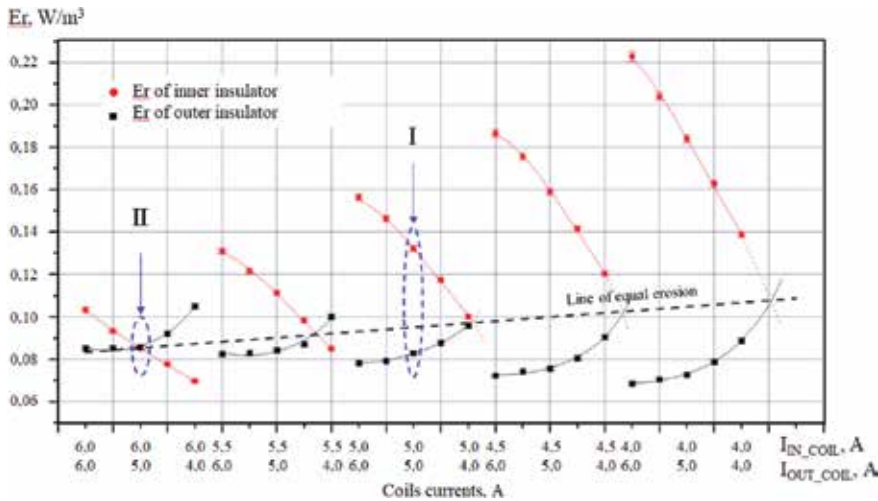
Figure 14.
Dependence of the erosion rate from the magnetic system coil currents.

# Thruster operation mode	I	II
Ratio of erosion rates of insulators	ΔV_R, %	ΔV_R, %
Direct method	33	0.249
OESSC method	32	0.243

Table 3.
Experimental results of erosion measurement with the OESSC method and direct method on two thruster regimes.

The erosion rate data for each of the insulators were approximated and extrapolated, in order to find regimes with the same erosion of the insulator edges. It is obtained that in the investigated range of coil current variation, there are five modes, under which the wear of the DCh edges will be uniform. However, the general wear of the material in other modes is greater. Therefore, mode II was selected for thruster operation.

After getting the results with the OESSC method, the experiment with direct measurements was provided for the thruster regime II. **Table 3** presents the results.

As it is seen from **Table 3**, results accepted by direct measurement were totally confirmed with the results of OESSC method measurements.

Conclusion was done to operate the thruster on the regime II, because on this regime, thruster lifetime is significantly higher.

7. Results of the investigation of several types of ceramic for the Hall thruster

Resource tests of the hollow thruster of power 100 W with one coil were conducted in the STC SPE of National Aerospace University named after N. Ye. Zhukovsky "Kharkiv Aviation Institute," Ukraine. The test purpose was to study the rate of ceramic insert erosion of BN with a different percentage of SiO_2 impurities.

To carry out the experiment, a thruster design was developed that allowed the rapid extraction of the outer and inner ceramic insulators without causing

mechanical damage to their surfaces. The design of the thruster allows ensuring unambiguous installation of ceramic inserts in the DCh.

For each of the ceramic samples, the test time was 68 hours. The whole period of time was divided into four stages of 17 hours each. At the end of each stage of the test, the measured mass for each of the ceramic inserts was suspended and measured using a laboratory scale WA-21.

7.1 Ceramic insulator mass measuring method

The measurements of the ceramic mass are carried out as follows:

1. insulator weighing;

2. degassing of insulators in a vacuum oven at a temperature of 200° C for 30 minutes; and

3. reweighing of the samples till the original weight value was restored to 95%

It was found that the samples with the composition of pure BN, as well as with 5 and 10% impurities of SiO_2 reduced in mass for half an hour when they were in the atmosphere. It took more than 2 hours to restore the original mass of the remaining samples (20, 35, and 50% SiO_2).

The results obtained were used to measure the weight of the esterified substance at the end of each test stage. After stopping the tests, the thruster should be cooled. The temperature of the thruster was controlled by the voltage on the coil. Then the thruster was reinstalled from the chamber, was sorted out, and the ceramic insulators were mounted on the scales. Measurement of the insulator mass was carried out for 40 minutes. Counting of time began from the moment of air intake into the vacuum chamber.

Figure 15 shows the results of the experiment.

As you can see from **Figure 15**, the lowest erosion parameters have pure nitride boron ceramic.
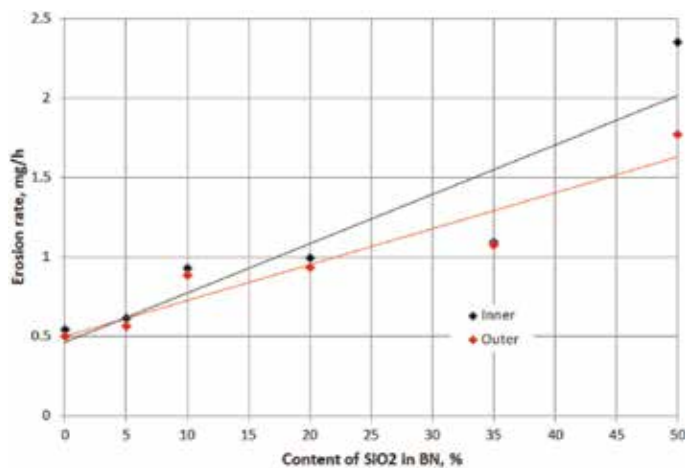
Figure 15.
The result of the tests: black—inner ceramic erosion rate; red—outer ceramic erosion rate.

8. Conclusions

One of the main HT characteristics that requires improvement is the lifetime of thruster. As it is known, one of the main factors that decreases thruster lifetime is the wear of DCh.

This chapter contains the results or investigation of thruster DCh erosion rate with the OES method. The algorithm of experiment is presented. The description of experimental equipment and its calibration process is presented.

Analysis of different intrusive and nonintrusive methods showed that there is no method that can give data about erosion rate of DCh walls separately during the thruster operation. The only method that can be applied in this case is a method of optical emission spectroscopy with scanning of plasma through collimator (OESSC). According to the accepted experiment results, it is shown that criteria of thruster regime selection can be different because the regime with minimal discharge current does not coincide with the regime of minimal erosion from both of ceramics.

Author details

Andrey Vitalievich Loyan* and Alona Nikolaevna Khaustova
Scientific-Technological Center of Space Power and Engines of National Aerospace University named after N. Ye. Zhukovsky "Kharkiv Aviation Institute", Kharkov, Ukraine

*Address all correspondence to: a.loyan@khai.edu

IntechOpen

References

[1] Mitrofanova OA. The influence of magnitude and topology of the magnetic field on the stationary plasma thrusters integral characteristics [dissertation of a Cand.Tech.Sci: 05.07.05] Kalynynhrad: Mitrofanova Olga Alexandrovna; 2015. 147 p

[2] Titov MYu. Stationary plasma thruster integral characteristics improvement by magnetic field gradient maximization [dissertation of a Cand.Tech.Sci: 05.05.03]. Kharkov: Titov Maksim Yur'evych; 2018. 170 p

[3] Khaustova AN. Method for stationary plasma thruster outer and inner ceramic edges erosion rate diagnostics [dissertation of a Cand.Tech.Sci: 05.05.03]. Kharkov: Khaustova Alona Nikolaevna; 2018. 217 p

[4] Semenov AA. Sputtering of ceramics and ceramic composites with low energy ion flows [dissertation of a Cand.Tech.Sci: 05.07.05]. Moskov: Semenov Alexander Anatolievich; 2015. 103 p

[5] Isayev YA, Oransky AI. The method of express estimation of gas hollow cathode erosion rate and results of its approbation. In: International Electric Propulsion Conference. 1995. pp. 1408-1412

[6] Rajput RU, Khaustova AN, Loyan AV. Plasma plume diagnostics of low power stationary plasma thruster (SPT-20M8) with collisional-radiative model. The European Physical Journal Applied Physics. 2017;**78**:9. Available from: h ttps://www.epjap.org/articles/epjap/ab s/2017/04/ap160348/ap160348.html [Accessed: 25.05.17]

[7] Khaustova AN, Loyan AV. Method for the erosion rate measurements of stationary plasma thruster insulators. East European Magazine of Advanced Technology. 2017;**3/5**(87):11-17

[8] Horshkov OA, Muravlev VA, Shahayda AA. Hall Ion Thrusters for the Spcacrafts. Moskov: Mashynostroenye; 2008. 279 p

[9] Prydannykov SY. Investigation of stationary plasma characteristics during long time operation [dissertation of a Cand.Tech.Sci: 05.07.05]. Kalynynhrad: Prydannykov Serhey Yur'evych; 2003. 203 p

[10] Merkur'ev DV. Methods of increasing of the thrust characteristics of a stationary plasma thruster operating at high specific thrust impulses [dissertation of a Cand.Tech. Sci: 05.07.05]. Moskva: Merkur'ev Denis Vladimirovich; 2015. 138 p

[11] Khaustova AN, Loyan AV, Rybalov OP. Development of optical receiver for erosion rate measurements of gas discharge chamber external and internal ceramics separately. Engineer's Bulletin. 2015;**2**:29-36

[12] Khaustova AN, Rybalov OP. OESSK method instrumentation facility and diagnostics method of stationary plasma thruster edge insulator wear. Engineer's Bulletin. 2016;**2**:212-220

[13] Pagnon D, Pellerin S, Dudeck M, Maksimenko TA, Koshelev NN, Loyan AV. Optical emission spectroscopy measurements on a SPT-20 Hall Effect Thruster on the KhAI ground test facility. Aviatsionno-kosmicheskaya tekhnika i tekhnologiya. 2006;**10**(36): 117-122

[14] Loyan AV, Maksimenko TA, Rybalov OP. 1500 hour lifetime test of SPT-20 and comparison with optical emission spectroscopy of plume. In: 31st International Electric Propulsion Conference (IEPC-2009); 20-24 September 2009; University of Michigan. USA; 4 p

[15] Rajput RU, Khaustova AN, Loyan AV. Development of xenon collisional radiative model for plasma diagnostics of hall effect thrusters. East European Magazine of Advanced Technology. 2017;**28**(86):24-29

Biological Propulsion Systems for Ships and Underwater Vehicles

Naga Praveen Babu Mannam and P. Krishnankutty

Abstract

Regulations and performance requirements related to technology development on all modes of transport vehicles for reduced pollution and environmental impact have become more stringent. Greening of transport system has been recognized as an important factor concerning global warming and climate change. Thus environment-friendly technical solutions offering a reduction of noxious exhaust gases are in demand. Aquatic animals have good swimming and maneuvering capabilities and these observations have motivated research on fish-like propulsion for marine vehicles. The fish fin movements, used by fish for their locomotion and positioning, are being replicated by researchers as flapping foils to mimic the biological system. Studies show that flapping foil propulsion systems are generally more efficient than a conventional screw propeller, which suffers efficiency losses due to wake. The flapping foil propulsors usually do not cavitate and have less wake velocity variation. These aspects result in the reduction of noise and vibration. The present study will cover an overview of aquatic propulsion systems, numerical simulations of flapping foils and ship model self-propulsion experiments performed using flapping foil system, particle image velocimetry (PIV), and digital fluoroscopy studies conducted on fish locomotion. Studies performed on underwater and surface vehicles fitted with flapping fins will also be presented.

1. Introduction

Biological locomotion is defined as the movement of animals from one place to another place with the use of its whole body or appendages. The modes of locomotion existing in nature are classified as self-propelled, e.g., swimming (fish, shark, whale, seal, and dolphin), running (cheetah, wolf, and zebra), flying (swallow, hawk, owl, crow, and bat), jumping, slither (snakes and other reptiles), hopping (kangaroo, rabbit, and grasshopper) and gliding (flying squirrel) are mentioned in **Table 1**. This is termed as active locomotion, where it uses its own body muscles or legs for locomotion. Passive locomotion is defined as animal species that depend on the environment for transportation, e.g., beetles and spiders. The entire biological locomotion is classified into four types—aquatic locomotion (underwater or surface swimming organisms), terrestrial locomotion (moving on the ground or any other surface, tree-dwelling), fossorial locomotion (underground) and aerial locomotion

(birds flying in the air). These animals use water and air as its medium for its locomotion. Flying fish and diving birds use the air-water medium for its locomotion. The classification of biological locomotion in nature is shown in **Figure 1**. The

Active locomotion				Passive locomotion
Fossorial locomotion	**Terrestrial locomotion**	**Aquatic locomotion**	**Aerial and arboreal locomotion**	
Earthworms, golden mole, marsupial mole, ground squirrels.	Walking and running: ostrich, emu, humans. Hopping or jumping: kangaroo, rabbit, hare, jerboa. Crawling or slithering: snakes, sand snakes.	Hydraulic propulsion: jelly fish. Waterjet propulsion: ocean squids. Fish: sharks, eels, tunas. Dual medium animals: fish: eels, flying fish. Other marine mammals: whales and birds: ducks, swans, ostriches.	Active flight: insects, birds, bats, pterosaurs. Gliding: flying snake, flying squirrel, flying frog, flying fish. Soaring: vultures, eagles, gulls. Ballooning: spiders. Arboreal locomotion: brachiating gibbon.	Hydrozoans, arachnids, insects, crustaceans, remoras, angler fish, parasites.

Table 1.
Locomotion in nature.

(a)

(b)

(c)

(d)
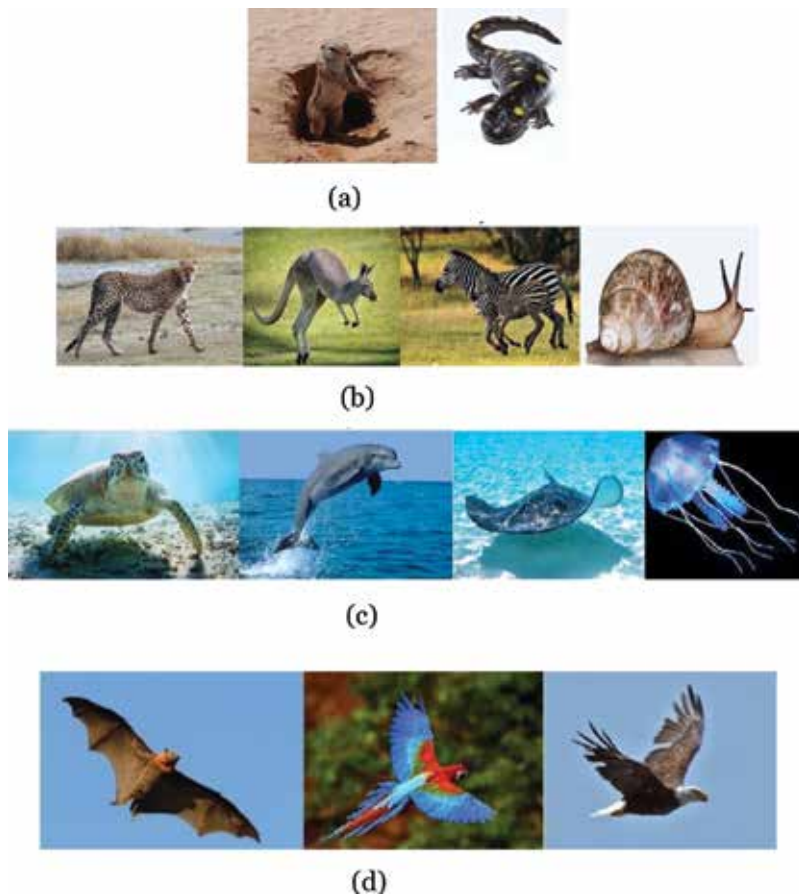
Figure 1.
Locomotion in nature. (a) Fossorial locomotion (underground) (e.g., Cape ground squirrel and mole salamanders). (b) Terrestrial locomotion—walking, hopping, running, crawling (e.g., cheetah, kangaroo, zebra, and snails). (c) Aquatic locomotion—lift based, undulation (body-caudal fin and median-paired fin modes), jet mode propulsion (e.g., turtles, dolphins, rays, and jellyfish). (d) Aerial locomotion—lift-based propulsion (e.g., bats, parrots, and eagles).
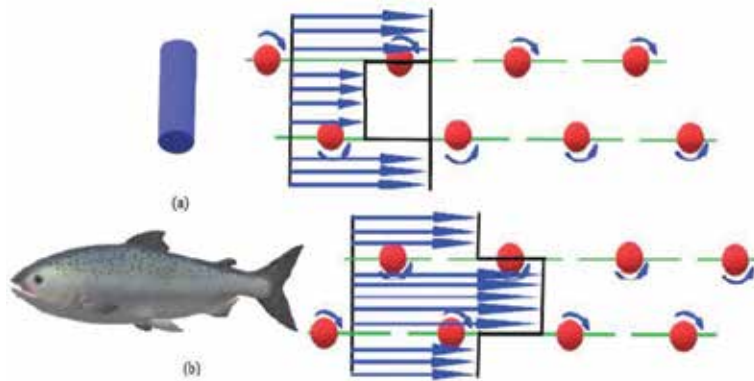
Figure 2.
(a) von Karman vortex street behind a cylinder and (b) reverse von Karman vortex street during fish swimming.

use of fossorial and terrestrial-inspired biorobots is currently used in the exploration of Martian atmospheres, robots in various defense sectors, etc. The aquatic locomotion is currently used in designed and development of autonomous surface ships and underwater vehicles for deep-sea exploration. The aerial locomotion is used for developing flapping micro aerial vehicles and reduction of noise vibrations from wind turbine applications.

1.1 Lift-based propulsion

In lift-based propulsion, flapping foils or wings are used to create lift and horizontal thrust force by moving through water. It creates a pressure difference between the top and bottom surfaces of the flapping wing. The sea turtles and penguins use their paired wings for creating lift and thrust force. Mainly, lift-based propulsors are vortex enhanced propulsors. They use this vortex enhancing mechanism of converting von Karman vortex street to reverse von Karman vortex street. All the lift-based animals produce drag at low Strouhal numbers. These animals sense the opposing fluid force on the body and increase the frequency and amplitude of fins, thereby increasing the Strouhal number that is in the range of 0.2–0.5. The von Karman vortex street and reverse von Karman vortex street are shown in **Figure 2**.

1.2 Drag-based propulsion

The drag-based animals such as ducks, Nile crocodiles, frogs, and other diving animals uses cyclic motion where they push water back in power stroke and return their limbs forward, which is defined as recovery stroke (**Figure 3**). In power stroke, the animals move their body forward by using its power stroke. In return stroke, the animals move their limbs to start position by pushing water forward minimally, which results in moving the body of the animal slightly backward. During the return stroke, the swimming movement of the animal is opposed and the opposing force is known as drag. This type of propulsion for conventional vehicles results in low efficiencies.

1.3 Undulatory propulsors

In undulation mode, aquatic animals swim through the water by the creation of undulations or flag movements with their bodies or using fins. The undulation

Figure 3.
Drag-based propulsion (e.g., ducks and Nile crocodile).

mode is classified as a body-caudal fin (BCF) propulsion and median-paired fin (MPF) propulsion. The BCF mode is again subdivided into (a) anguilliform, (b) carcharhiniform (c) sub-carangiform (d) carangiform, (e) thunniform (f) esociform fish and (g) ostraciiform modes. The anguilliform and ostraciiform modes are slow swimmers and carangiform, thunniforms are relatively fast swimmers. In the anguilliform mode, slender body fish such as sea snakes, eels generate propulsive wave starting from head portion of the body to the tail portion. The sub-carangiform and carangiform group increase its wave amplitude from the middle portion of the body to rear part of the fish body. The thunniform mode of fish is high-speed long-distance swimmers. The ostraciiform group of fish is box-shaped bodies with caudal fin. Only the caudal fin itself oscillates to generate thrust. Similarly, MPF mode is classified as (a) tetraodoniform, (b) balistiform, (c) diodontiform, (d) rajiform, (e) amiiform, (f) gymnotiform and (g) labriform. In MPF mode, most of the fish use a pair of pectoral fins, anal fins or a combination of both for generating a propulsive force. The detailed classification is given in **Table 2**.

1.4 Jet propulsors

In Jet propulsion mode, aquatic animals fill their cavity by compressing the fluid and eject the fluid out to propel themselves in the opposite direction of the ejected fluid. In jet propulsion mode, the propulsion mechanisms are different from one animal to another animal. In jellyfish, it draws water from the rear and ejects it through the rear part. In scallops, fluid enters from its front portion and ejects out at its rear portion of the body.

1.5 Literature review: state of the art

Experimental and numerical methods are the oldest and most reliable sources of information on any physical studies and some do apply for the present studies on marine vehicle propulsion. The experimental studies are carried out on flapping foil propulsor by considering the effects of variations on the Strouhal number and maximum angle of attack on the thrust force which results in increasing hydrodynamic efficiency of flapping foil [1]. The pectoral fin model of bluegill sunfish is studied during its maneuvering to avoid the obstacles. This study involves biological studies of pectoral fins of sunfish, developing kinematic models of the motion of pectoral fins, 3D computational studies of pectoral fins flow characteristics and forces, and implementation of simplified models of pectoral fin kinematics and mechanical properties in a physical model [2]. The mechanical design of fish fin

Body and caudal fin (BCF) propulsion	Median and paired fin (MPF) propulsion
Anguilliform: eel	Tetraodoniform: ocean sunfish
Carcharhiniform: hammerhead sharks	Balistiform: trigger fish
Subcarangiform: rainbow trout	Diodontiform: puffer fish
Carangiform: mackerels	Rajiform: rays
Thunniform: tuna	Amiiform: bowfin fish
Esociform: northern pike	Gymnotiform: knife fish
Ostraciiform: box fish	Labriform: wrasses

Table 2.
BCF and MPF propulsors.

rays that allows active muscular control of curvature and flexibility of the fish body in propulsion are studied [3]. Experimental studies are performed on purely-pitching foil with a rigid and flexible flap of suitable stiffness. The rigid pitching foil produces a weak and meandering jet (and thrust), whereas the flexible foil produces a strong jet of the wake. Deformations of the flexible flap suppress meandering by increasing the initial gap between two successive vortices and by imposing a convective motion on the shed vortices even in the absence of free-stream velocity [4]. Four foils made of adhering layers of plastic sheets to produce discrete regions of high and low flexible stiffness of biologically-relevant magnitudes. Using a

mechanical flapping foil controller, the forces and torques in three directions (x,y,z) and the swimming performance under both heaving motion and constant 0° angles of attack case studies are carried out experimentally [5]. The 2D flapping foils in a tandem configuration in forwarding propulsion at *Re* = 5000 using experimental and numerical techniques are studied. Both tandem foils are subject to symmetrical translational and rotational motions with a Strouhal number of 0.32. The observations show that the foil-wake interaction is favorable to thrust generation, which requires the tandem wing has to cross the shear layer shed from the front wing and results in an increase in angle of attack [6]. Three-dimensional numerical simulations are carried out on tuna fish to study the flow characteristics and vorticity pattern around the fish when swimming in a straight line. The body undulation occurs at the rear half of the fish, and the caudal fin of the tuna fish oscillates with combined sway and yaw motions [7]. The underwater vehicle (UV) which has both flapping-foil and gliding function are studied. Numerical simulations are carried out in the fluent code using dynamic meshing on a single degree of freedom flapping-foil movement, which demonstrated the mechanism of flapping foil. The turbulence effects were taken into account, and the turbulent stress was evaluated by means of the realizable *k*-epsilon model [8]. The detailed hydrodynamic analysis of the thrust generated by an oscillating hydrofoil is carried out using numerical and experimental studies. The hydrofoil is mounted at the bow of a platform supply vessel as a means of auxiliary propulsion and, is vertically oscillating due to the ship's heave and pitch motions in head-waves [9]. On scrutinizing the works presented above it is clearly evident that the experimental approaches have been quite successful over years in predicting the performance of biomimetic propulsion systems for ships and AUV's. A high degree of robustness and reliability has also been observed in methods based on systems and parametric identification in the design and development of bioinspired systems for marine vehicles. Other theoretical methods can only give rough estimates of the thrust generated by flapping foils. Numerical methods Reynolds-averaged Navier-Stokes equations (RANSE)-based computational fluid dynamics (CFD) techniques have been successfully employed in simulating two-dimensional, flapping foils. The method is still in its developing stage, where a confidence level in its application to three-dimensional flapping foils problems is yet to be achieved. Many authors are currently concentrating on this research area of numerical study of 3D flapping foils for marine vehicles.

As far as the use of bioinspired propulsion systems for ocean-going vessels is concerned, the literature to date has been able to give only laboratory demonstrative models. The application of oscillating fins as propellers to conventional marine vehicles is being explored and this has given the impetus in this chapter to concentrate on bioinspired propulsion for marine vehicles. This necessitates the need for detailed experimental and numerical study on three-dimensional fish-like propulsion system used in surface and sub-surface marine vehicles. These studies are envisaged to understand the fluid particle level movements around different fish fins during a live fish swimming, mimicking these fins and its motion using the physical model in a laboratory, attach fins to surface ship and underwater vehicle models to determine the self-propulsion parameters and resulting thrust, torque and propulsive efficiency. The entire study has been divided into four sections. Section 1 gives an introduction to the study, presents the review of relevant literature and the motivation for this study. Section 2 shows the various mathematical models used for the determining hydrodynamic forces of bioinspired propulsors. Section 3 introduces examples of bioinspired propulsion systems. Section 4 summarizes the work and the conclusions from the above studies are presented.

2. Empirical methods to determine hydrodynamic forces and propulsive efficiencies of bioinspired propulsors

2.1 Estimation of propulsive forces using numerical techniques

The non-dimensional flow variables are used for the analysis of the results obtained from the numerical simulations of lift-based propulsion systems. The forces acting on flapping foil (**Figure 4a** and **b**) subjected to heaving and pitching motions are resolved in x and y-direction as $F_X(t)$ and $F_Y(t)$, respectively, and the moment about the pivot point is denoted as $M(t)$. The force coefficients are given as

$$C_X = \frac{(\overline{F}_X)}{\frac{1}{2}\,\rho\,U^2 cS} \tag{1}$$

$$C_Y = \frac{F_Y}{\frac{1}{2}\,\rho\,U^2 cS} \tag{2}$$

$$C_M = \frac{M}{\frac{1}{2}\,\rho\,U^2 c^2 S} \tag{3}$$

where U and c are the free stream velocity and hydrofoil chord length, ρ is the density of fluid respectively, and S is the span of the hydrofoil and is assumed to be unity. The thrust force created by flapping hydrofoil is $F_X(t)$. The average thrust over n complete flapping cycles over period T is given as

$$(\overline{F}_X) = \frac{1}{nT}\int_0^{nT} F_X dt \tag{4}$$

The power required for the flapping foil, defined as the amount of energy imparted to the hydrofoil to overcome the fluid force, is given as

$$P(t) = -F_y(t)\frac{dy}{dt} - M(t)\frac{d\psi}{dt} \tag{5}$$

The sign on both the terms in Eq. (5) is negative as vertical force and moment are the reaction forces created by the fluid as the hydrofoil moves through it.

The average power over n complete cycles of flapping, over a period T, is given as
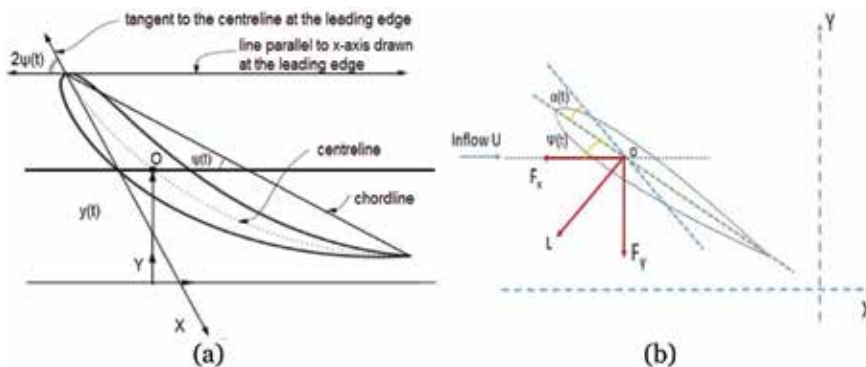
Figure 4.
Foil motion with respect to angle of attack (α), sway and yaw modes.

$$(\overline{P}) = \frac{1}{nT} \int_0^{nT} P \, dt \tag{6}$$

$$(P') = \frac{(\overline{P})}{\frac{1}{2} \rho \, U^3 cS} \tag{7}$$

The propulsive efficiency η is defined as the ratio of the output power $(\overline{F}_X)U$ to the input power $(\overline{P})$. From Eqs. (1) and (7), η is given by

$$\eta = \frac{(\overline{F}_X)U}{(\overline{P})} = \frac{(C_X)}{(P')} \tag{8}$$

2.2 Estimation of thrust and torque of pectoral fins using propeller theories

Flapping foil is composed of a series of blade elements each of which produces hydrodynamic forces such as lift, drag, thrust and torque due to the motion of the fluid. The axial component is the element thrust & the tangential component is the element torque. Integration over the radius of all sections gives total thrust & torque of the flapping foil. In this method, the pectoral flapping wing is divided into a number of independent sections along its span. At each section, a force balance is applied involving lift, drag, thrust, and torque produced by the section shown in **Figure 5**. At the same time, a balance of axial and angular momentum is also applied. This approach is applied to the flapping pectoral fins and the resulting thrust (T_h) and torque (T_q) are obtained as,

$$T_h = \int_{R_o}^{R_t} (C_L \sin\gamma - C_D \cos\gamma) \times 0.5 \times \rho \times V^2 \times C(r) dr \tag{9}$$

$$T_q = \int_{R_o}^{R_t} (C_L \cos\gamma + C_D \sin\gamma) \times 0.5 \times \rho \times V^2 \times C(r) r dr \tag{10}$$

Here C_L and C_D are lift coefficient and drag coefficient with a given angle of attack.
(α) and V is the velocity of flow and is given by,

$$V(r,t) = \sqrt{U^2 + (r\omega(t))^2} \tag{11}$$

The inflow angle γ is calculated as,
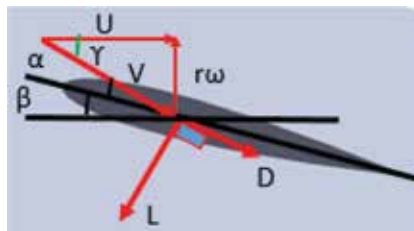
Figure 5.
Flapping foil blade section.

$$\gamma(r,t) = \tan^{-1}\frac{r\omega(t)}{U} \tag{12}$$

As the flapping motion is subjected to sinusoidal motion, the flapping angle $\theta(t)$ and the angular velocity $\omega(t)$ are given by the following expressions

$$\theta(t) = \theta_{max}\sin\frac{2\pi}{T}t \tag{13}$$

$$\omega(t) = \frac{2\pi}{T}\theta_{max}\cos\frac{2\pi}{T} \tag{14}$$

2.3 Estimation of torque of caudal fin

The surface ship model is fitted with caudal fin oscillation mechanism where DC servo motors are used as the prime mover. The power demand for fin oscillation depends on the fin size, its oscillation frequency, and amplitude. The stroke of the caudal fin in the x-y plane is y_G (**Figure 6**) is given by,

$$y_G = r\sin\psi \tag{15}$$

where ψ is the yaw angle. The fin is oscillating with a frequency f (Hz) and hence the instantaneous position of the fin CG is given by

$$y_G = (r\sin\psi)\sin 2\pi ft \tag{16}$$

The velocity, v_G (m/s) is given by,

$$v_G = \frac{dy_G}{dt} = 2\pi fr\sin\psi\,(\cos 2\pi ft) \tag{17}$$

when caudal fin moves to initial centerline of the fish body, $cos2\pi ft$ become one and hence the maximum velocity is given by,

$$v_{Gmax} = 2\pi fr\sin\psi \tag{18}$$

The maximum drag force on the caudal fin is,

$$D_{max} = C_D\left(\frac{1}{2}\right)\rho\,A_f v_{Gmax}^2 \tag{19}$$

where C_D is the drag force coefficient and A_f is the fin profile area.
The maximum torque developed by the caudal fin oscillation is,

$$Q_{max} = D_{max}r = 2\pi^2 C_D\rho\,r^3 A_f f^2 \sin^2\psi \tag{20}$$

Figure 6.
Caudal fin motion mode.

2.4 Estimation of propulsive forces from PIV experiments

In flow visualization experiments, the quantitative measures of hydrodynamic forces acting on the fish body and impulse can be determined. There are two methods for estimating the forces in a fluid, one based on the fluid momentum which is used for unsteady flows and the other one is based on fluid vorticity which is used for steady flows.

In both the cases, one first estimates impulse I, the integral of force F applied to the fluid over time, the mean force F_{mean} applied to the fluid multiplied by the total time T over which it was applied:

$$I = \int_0^T F \, dt \tag{21}$$

$$I = F_{mean} \, T \tag{22}$$

To obtain the force, differentiating I by T. Therefore,

$$F = \frac{\partial I}{\partial t} \tag{23}$$

2.4.1 Vortex analysis

The circulation is defined as the total vorticity within an area circumscribed by a closed loop. For a steadily moving vortex ring, the procedure to estimate the force generated is quite straightforward. Any sufficiently large loop that passes through the center of vortex ring has a constant circulation that is proportional to the force required to generate the ring:

$$F_{mean} = \frac{\pi \rho \Gamma D^2}{4} \tag{24}$$

where ρ is the density of the fluid, Γ is the circulation, D is the distance between the two vortex centers in the plane.

Mathematically, circulation Γ can be written in two equivalent ways:

$$\Gamma = \int_\Sigma \omega \, d\Sigma \tag{25}$$

$$\Gamma = \oint_c u \, \mathrm{d}l \tag{26}$$

where Σ is a surface in the fluid, C is the closed contour around the edge of the surface, and l is the tangent vector along the vorticity contour.

3. Examples of aquatic propulsion systems

3.1 Experimental and numerical study of a surface ship fitted with tandem flapping foils

In the present study, experimental and numerical studies are carried out to ascertain the thrust producing mechanism of flapping foils [10]. The propulsive performance of flapping foils fitted to surface ships in tandem mode at its midship

position is studied. The current work attempts to investigate the thrust generation capability and efficiency of the rigid and flexible hydrofoil in open water condition and the results of which are compared with those obtained from ship model tests in self-propulsion mode. The foil flexibility in computational fluid dynamics (CFD) environment is introduced using an appropriate user-defined function. The lift-based penguin type propulsion system installed in a ship model, used in the study, is shown in **Figure 7**. A pair of flexible flapping foils is attached to the ship model bottom. The amplitude and frequency of these flapping foil oscillations are varied using the electro-mechanical systems. In the experimental study, ship model resistance tests, bollard pull tests, and self-propulsion tests are carried out in the towing tank and the results are recorded, presented and discussed.

3.1.1 Flapping foil propulsion ship: resistance tests

The ship model fitted with fins and other fixtures were run in the towing tank to experimentally determine the model resistance at different speeds. The resistance force of a ship at a constant speed is the force required to tow the ship in calm water at that speed. The model is accelerated to the desired speed and the speed is kept constant. The average values of the measurements for the period of constant speed are recorded. The ship model was built in fiberglass to the scale 1:15. The towing tank dimensions are 82 m long × 3.2 m wide × 2.5 m (water depth). The model was ballasted to the loaded condition with an even keel. Model towing tests were conducted in the speed range covering the design speed. The resistance test results are shown in **Figure 8**. The effective power of the model with fins is estimated at 33.15 W at a speed of 1.2 m/s. The ship hull model (below bottom) is attached with chain sprockets, chain drives, bearing blocks, two circular shafts of 25 mm diameter to mount the flexible flapping foils stiffened with steel plates. This additional fitting attached to the ship hull caused an increase in resistance.

3.1.2 Bollard pull tests

The ship model is tied to a stationary post and the flaps oscillate at different frequencies and amplitudes corresponding to different Strouhal numbers. The thrust developed by the flapping foils is measured in each case using a load cell. The maximum thrust was found to be 21.3 N at f = 3 Hz and oscillation amplitude of 300 mm.

3.1.3 Self-propulsion tests

In self-propulsion tests, the ship model is fitted with an electric motor and load cell to measure the thrust force generated by the flapping foils. The ship speed is matched with towing carriage speed to determine the speed achieved by the ship at different frequencies and amplitudes and the forces are measured using the load cell
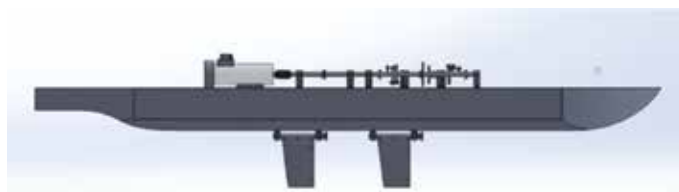

Figure 7.
Ship model fitted with flapping foils.

and data acquisition system. The maximum thrust force of 13.18 N at *St* = 0.53 is measured and shown in **Figure 9**. The thrust force generated by the foils in bollard pull condition is higher when compared to the self-propulsion tests as it appears in the vessels fitted with the conventional screw propellers.

3.1.4 Numerical study of flexible and rigid flapping foil

The standard National Advisory Committee for Aeronautics airfoil section (NACA0012) with a chord length *c* = 0.1 m is used for the hydrofoil modeling. NACA0012 is symmetrical foil, so flap angle of attack *α*, is symmetrical about 0°. The NACA0012 section is mainly used for plunging and combined pitching and plunging motions in numerical simulations for fully laminar and fully turbulent flow regimes.
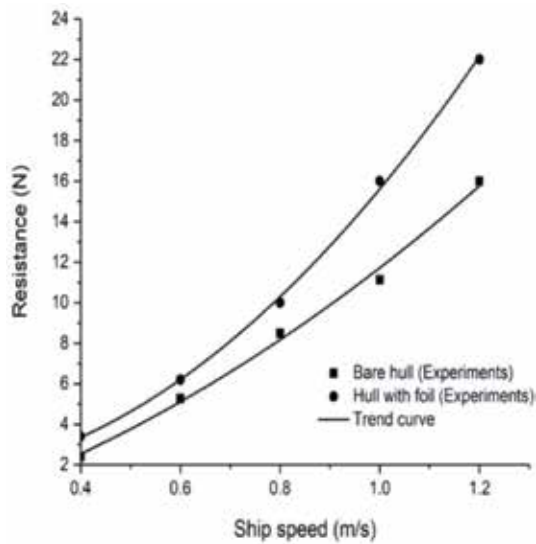
Figure 8.
Resistance tests of the ship model with and without the foils fitted.
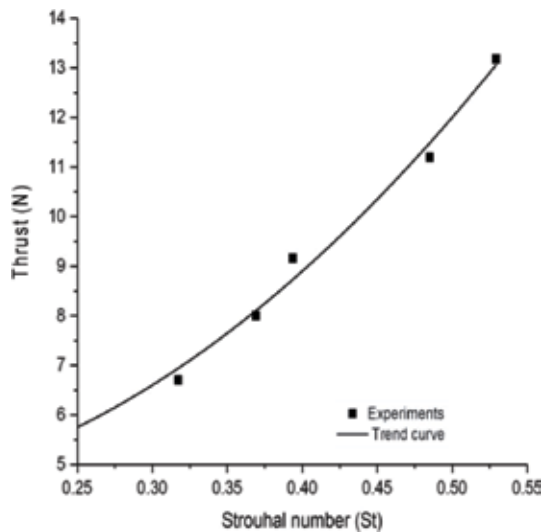
Figure 9.
Thrust developed in self-propulsion mode $(V \neq 0)$.

3.1.5 Results and discussions

The wake characteristics of rigid and flexible flapping foils are studied at different Strouhal numbers (St = 0.1–0.4) with different maximum angles of attack such as 10°, 15°, and 20°. As the flapping frequency and amplitudes are increasing (St = 0.1–0.4), the fluid flow separates from the trailing edges forms a jet of alternating vortices which results in thrust production. This formation of vortices is termed as reverse von Karman Vortices [10]. As the angle of attack increases from 10° to 20°, the vortices becomes stronger at St = 0.1 and the resulting thrust force increases. The absolute vorticity contours for flexible flapping hydrofoil at α_0 = 20° at different Strouhal numbers are shown in **Figure 10**. The variation of force and moment coefficients for flexible flapping foil is shown in **Figure 11**. The average thrust coefficient (C_X) and efficiency (η) of both rigid and flexible foils are shown
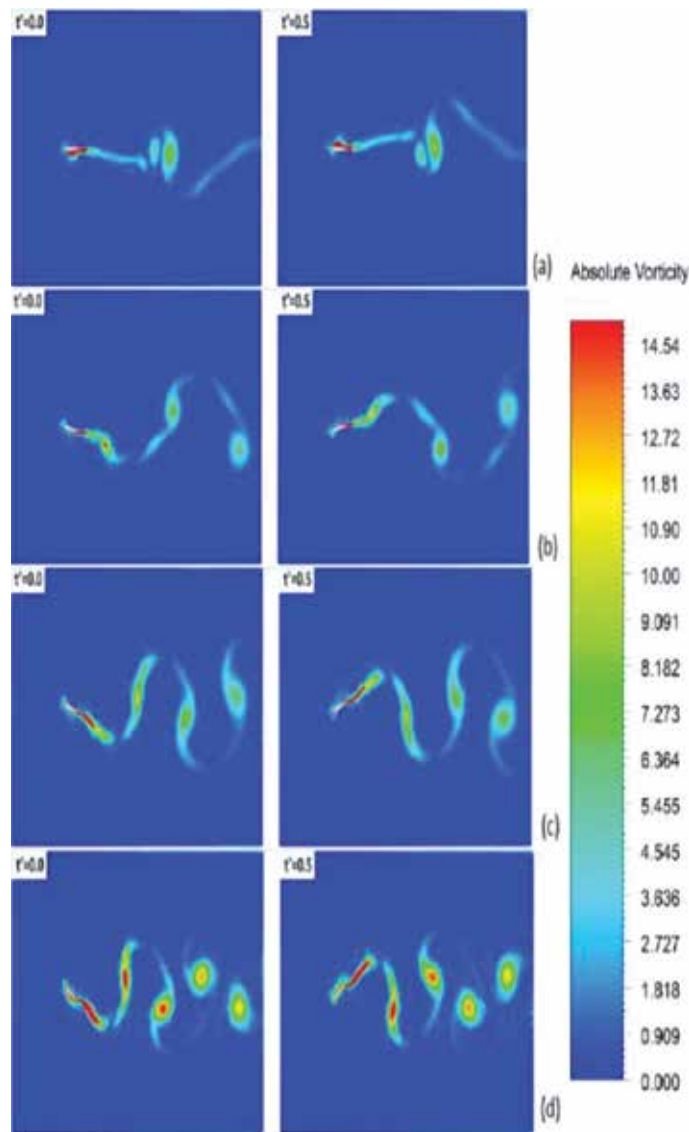
Figure 10.
Absolute vorticity contours of flexible flapping hydrofoil at α_0 = 20° for (a) St = 0.1, (b) St = 0.2, (c) St = 0.3 and (d) St = 0.4.

in **Figures 12** and **13** for different angles of attack (10°, 15°, 20°). From the experimental studies in self-propulsion mode, the thrust (C_X) = 2.75 is measured at St = 0.53. In numerical studies, the maximum thrust coefficient (C_X) = 2.38 is obtained for α_0 = 20° at St = 0.55.

3.2 Obtaining 3D kinematics of fish locomotion using digital X-ray fluoroscopy

Carangiform fish play a major role in propulsion and maneuvering performance. In this section, skeletal view of the carangiform fish spine and caudal fin kinematics during forward swimming are presented using digital X-ray fluoroscopy technique. The aim of this study is to obtain the 3D kinematics of the fish spine and caudal fin motions. The X-ray recordings were possible through collaboration between the Department of Ocean Engineering, Indian Institute of Technology (IIT) Madras, India, and Sri Ramachandra Medical College (SRMC), Chennai, India. Biplanar high-speed cineradiographic fluoroscopy with an image resolution of 1536 × 1024 was taken from top view. The fish swims freely in a glass tank during the experiments. The experimental set up is shown in **Figure 14**. The spinal chord and caudal fin motions were recorded during fluoroscopy tests. These motions are tracked manually for all the videos in which fish swims straight and achieves steady state
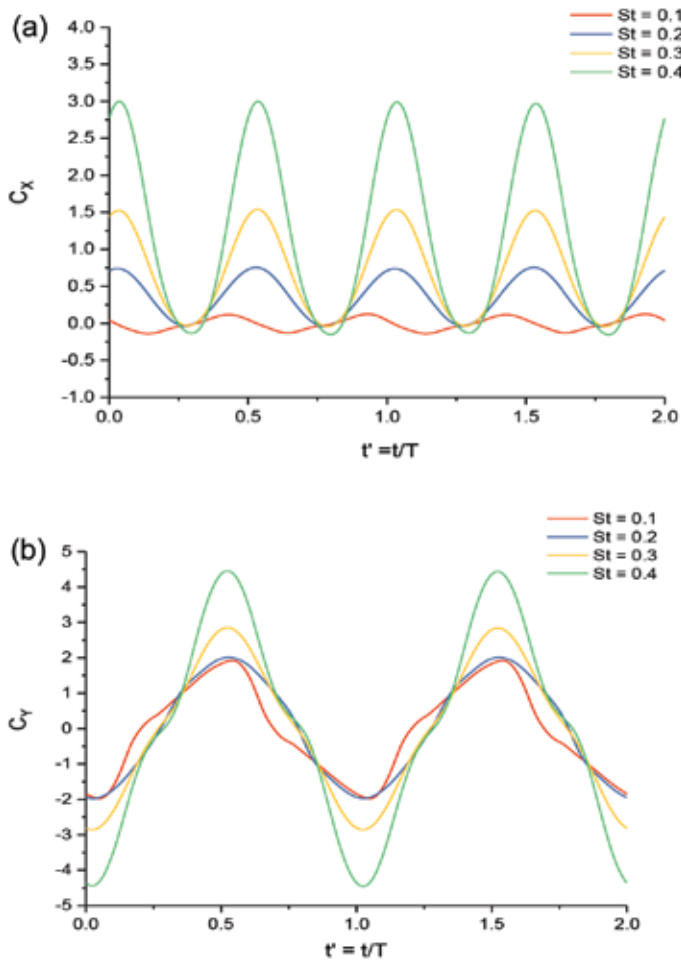
Figure 11.
Variation of (a) C_X, (b) C_Y for St = 0.1–0.4 at α_o = 20° for flexible foil.

locomotion. The fluoroscopy images of the fish spine and caudal fins are shown in
Figures 15 and **16**. As shown in **Figure 16**, the number of joints in the fish spinal
chord and representation of pectoral fins, the caudal fin is marked. By using custom
software, OpenCV we can track these points in the images in order to get the 3D
kinematics of fish swimming which can be taken as a future study in this area.
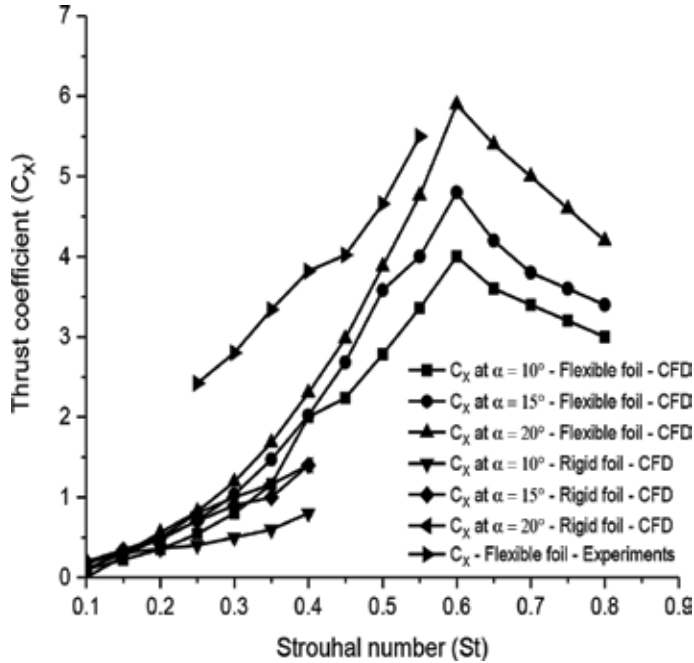
Figure 12.
Thrust coefficient at $\alpha_o = 10°$, $15°$ and $20°$ for tandem flapping foil.
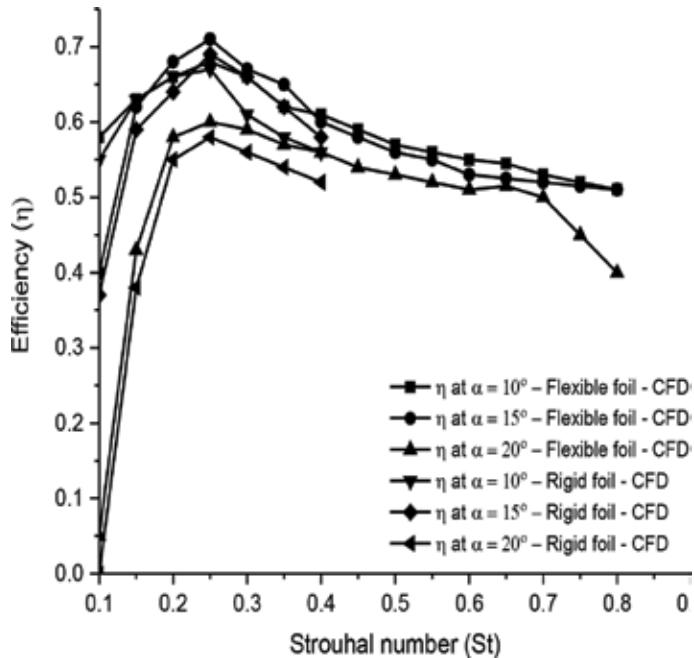
Figure 13.
Propulsive efficiency at $\alpha_o = 10°$, $15°$ and $20°$ for single foil.

Figure 14.
Digital fluoroscopy recording of fish swimming.
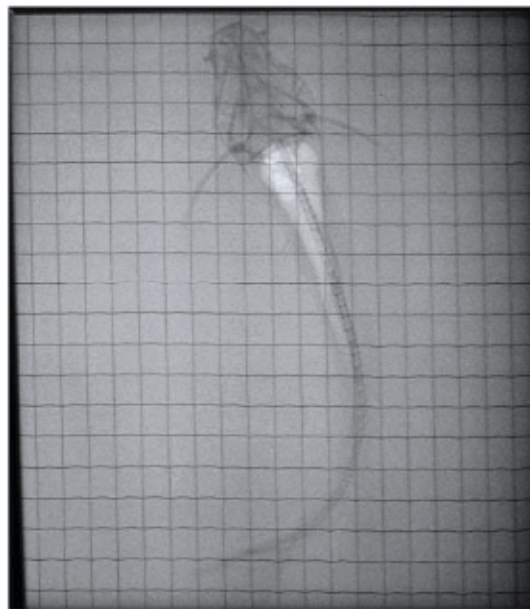
Figure 15.
Fluoroscopy image of fish swimming—skeletal view.

3.3 Experimental study of fish locomotion using 2D particle image velocimetry

Two-dimensional flow visualization experiments are carried out to visualize the flow pattern around the caudal, pectoral, anal and dorsal fins of a freely swimming fish particle image velocimetry (PIV) system [11]. The freshwater black shark fish with a body length of 26 cm is used for the present experimental study. The fish is placed inside a glass tank of size $L \times B \times D = 75 \times 29 \times 37$ cm and it is allowed to swim freely in the tank shown in **Figure 17**. The PIV system used in this experiment consists of (i) a double-pulsed Nd-YAG (neodymium-doped yttrium aluminum garnet) laser with 200 mJ/pulse energy at 532 nm wavelength, (ii) a charge-coupled device (CCD) camera with a 2048×2048 pixels and an image capturing speed of 14 frames per second (fps), (iii) a set of laser and a camera controllers and, (iv) a data acquisition system. The laser sheet is aligned with the longitudinal vertical *XZ* and transverse *YZ* planes. The camera is positioned in front of the test section perpendicular to the laser sheet.
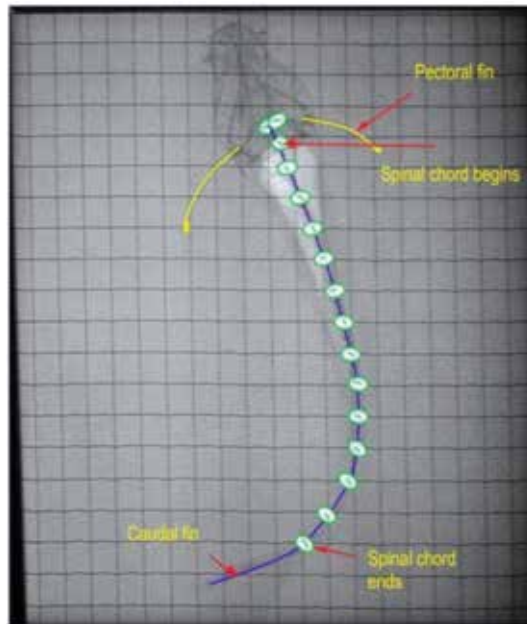
Figure 16.
Manual tracking of fish spinal chord joint and caudal fin.

Figure 17.
Freely swimming freshwater shark fish.

The PIV technique involves the introduction of tiny particles called 'seeder particles' into the fluid path. Hollow glass spheres with a mean diameter of 10 μm are used as the tracer particles. The PIV setup used in the present experiment is shown in **Figure 18**. The flows around the fins of freely swimming fish are analyzed and the velocity vector fields are presented here. In this analysis, we are presenting a raw CCD (charged coupled device) image and the processed image at different time intervals. The white boundary line represents the body contour of fish. The primary vortex regions are marked as V_1, V_2 in images. **Figure 19** shows the CCD image and velocity vector field around adipose and anal fins for Δt = 900 ms. The adipose and anal fins generated vortices, that passes downstream, interacts with caudal fin vortices which results in increasing the propulsive performance. **Figure 20** shows CCD image and velocity vector field around caudal fin stroke in *YZ* plane for Δt = 900 ms while the fin is at the center plane. A jet of high-velocity flow is observed at the top of the caudal fin.
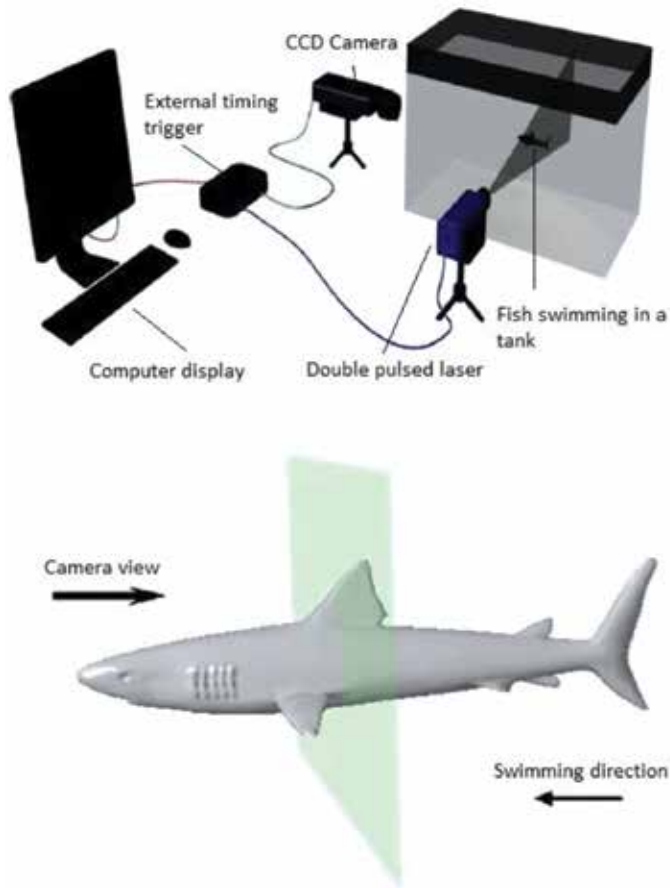
Figure 18.
PIV system arrangement.

3.4 Experimental study of a remotely operated surface ship fitted with caudal fin

The thunniform mode caudal fin propulsion system is designed and developed for a surface ship model. The caudal fin acts as a main propulsor is operated at different frequencies and amplitudes to experimentally find its propulsive performance [12]. The length of the ship model is 1.4 and 0.35 m wide. The caudal fin is actuated by single DC servo motor powered by the lithium-polyimide(lipo) battery of 25.9 V. The crank slider mechanism is used for converting the rotary motion of the motors into the fin oscillation mechanism. By coordinating the movements of the tail fin, the ship model can simulate the movements of fish in the water. **Figures 21** and **22** shows the surface ship model and caudal fin propulsion mechanism used here. The control system consists of a wireless communication unit, microprocessor, strain gauge sensors for force measurement, data acquisition system. The block diagram and tail fin motor connections are shown in **Figure 23**.

3.4.1 Results and discussions

The remotely operated surface ship model in self-propulsion mode is shown in **Figure 24**. In self-propulsion tests, the caudal fin amplitude is kept constant at 0.15 m and the frequencies are varied from 0.5 to 1.75 Hz. The caudal fin of ship
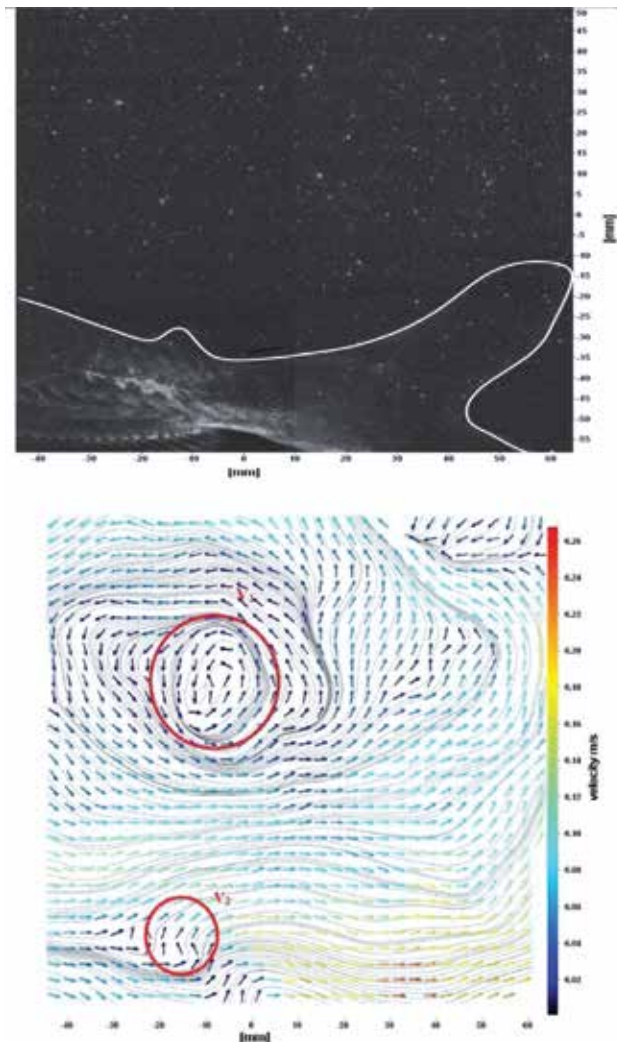
Figure 19.
CCD image and velocity vector field around adipose (upper one) and anal (below one) fins for Δt = 900 ms.

model is tested at different frequencies and constant amplitude and the thrust forces are measured using strain gauges mounted on the caudal fin shaft. The data acquisition system (consists of oscilloscope and amplifier) shown in **Figure 25**. The forward velocity (*V*) of remotely operated surface ship model, fitted with caudal fin, increases until the caudal fin frequency reached about 1.5 Hz and above that the speed of the ship decreases and shown in **Figure 26**. The maximum speed achieved by the vehicle is 0.4 m/s. In self-propulsion tests, a maximum thrust of 8.6 N was recorded at *St* = 0.4 shown in **Figure 27** where the thrust force is plotted against the frequency of flap. In bollard pull, the maximum thrust is found to be 14.8 N at *f* = 1 Hz.

3.5 Experimental study of the remotely operated underwater vehicle with bioinspired caudal fin

The bioinspired robotic fish is shown in **Figure 28** where the body is an axis-symmetric one with a long cylindrical body having a hemispherical nose and conical aft portion, and with a pair of pectoral fins at the forward area and tail (caudal) fin
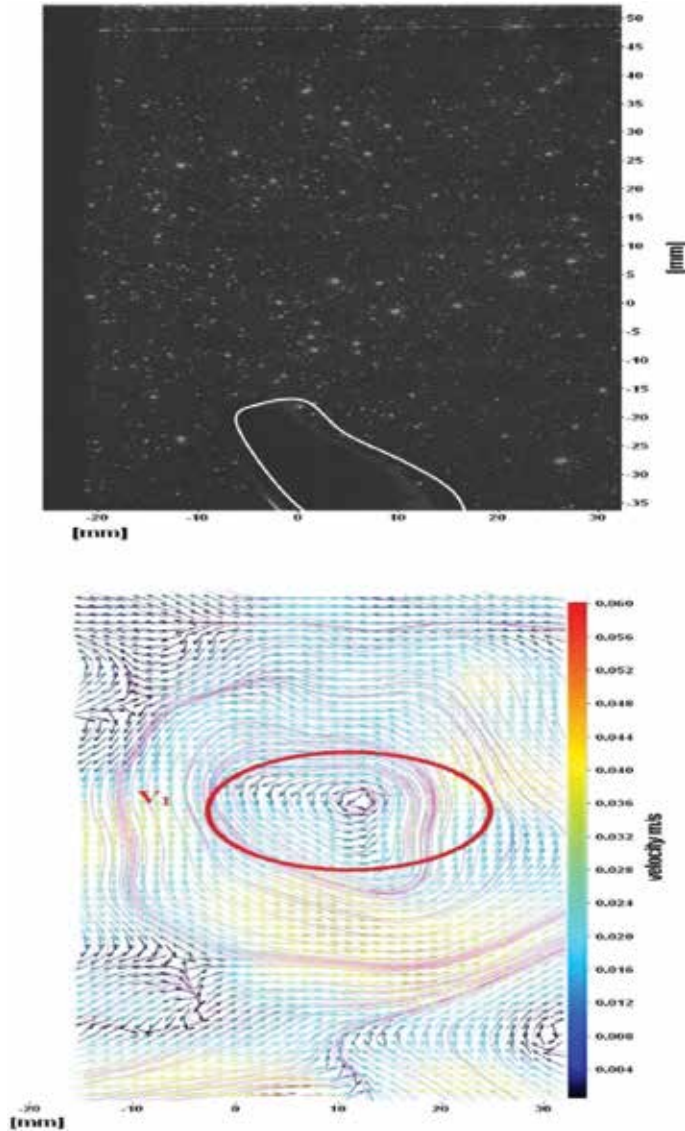
Figure 20.
Consecutive CCD image and velocity vector field around caudal fins stroke at center in YZ plane for Δt = 900 ms.
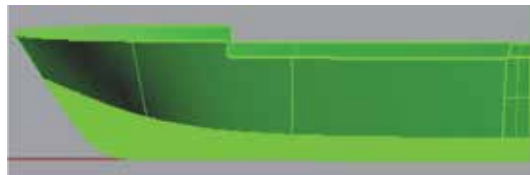

Figure 21.
Remotely operated surface ship model.

at the extreme aft. The principal dimensions of the body are 1.2 m long and 0.16 m diameter. The biomimetic caudal fin fitted at the end of the tail portion of the body acts as the main propulsor for generating thrust. The robotic fish comprises of three individual modules, pectoral fin mechanism, a caudal fin module, and a control system and its battery modules. The hull is made of fiber reinforced plastic (FRP)

Figure 22.
Caudal fin propulsion mechanism.
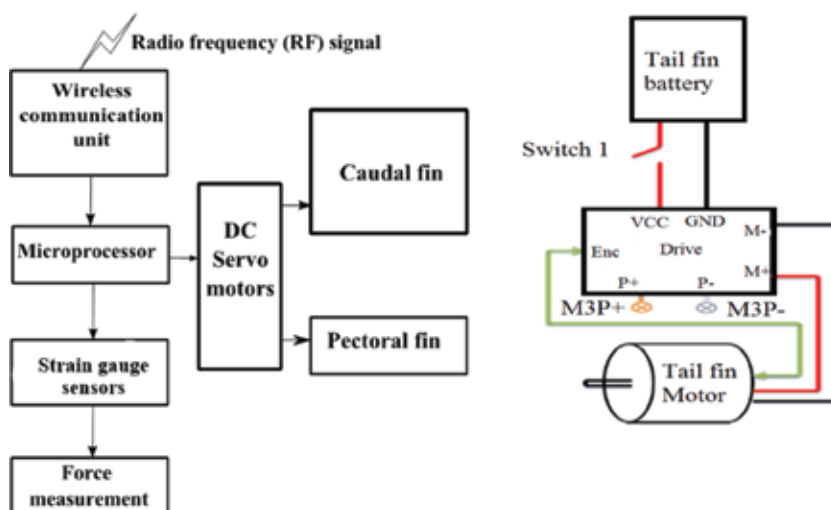
Figure 23.
Block diagram and caudal fin mechanism connections.

Figure 24.
Remotely operated surface ship model in the self-propelling mode.

material of 6 mm thick. The vehicle is propelled by a bioinspired caudal fin in wireless mode. The CFD estimated drag of the underwater vehicle with fins is 48 N and that for the bare hull is 33 N at a speed of 2.5 m/s. As expected, high-pressure regions are seen at the leading edges of pectoral and caudal fins and low-pressure regions are created at the trailing edges of the fins as shown in **Figure 29**. The high-pressure regions are also present in the forward nose of the hull.

3.5.1 Results and discussions

Experiments are conducted to predict the swimming and propulsive behavior of the bioinspired robotic fish in different operating conditions. The tests are

Figure 25.
Data acquisition system.
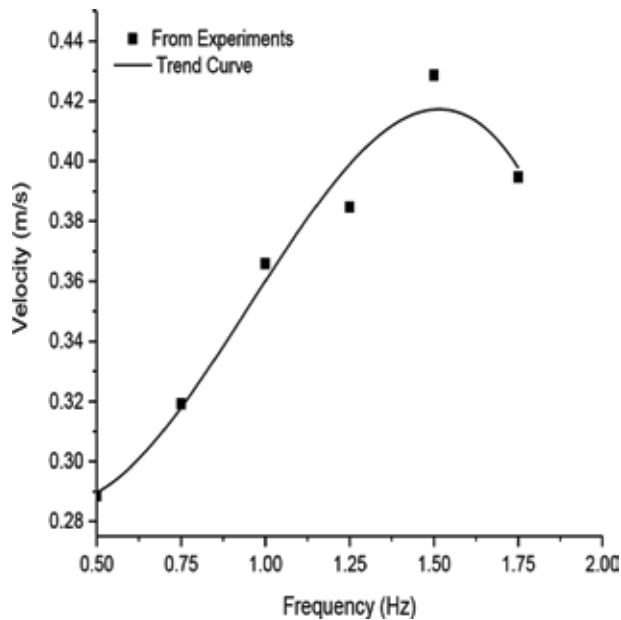
Figure 26.
Ship model velocity at different oscillation frequencies of the flap.

conducted in the towing tank and the vehicle swimming velocity and fin developed force is measured. The towing tank dimensions are 82 m long × 3.2 m wide × 3 m depth. The water depth used for all experiments is 2.6 m. The underwater vehicle is propelled by the thrust produced due to the oscillation of caudal fin fitted at the stern part of the vehicle. The swimming velocities at different oscillation frequencies are shown in **Figure 30**. The results show that the fin oscillation generates thrust forces for a range of frequency. At free surface condition, the velocity of 0.53 m/s is achieved at a frequency of 1.5 Hz with an amplitude of 180 mm. In submerged condition, the vehicle achieved a speed of 0.29 m/s. The body attains higher velocity at the surface condition, having less wetted surface area and thus reduced body resistance. In the case of submerged condition, the body resistance is more and hence moved with lesser speed. The thrust force generated by the caudal fin of robotic fish is measured by using strain gauge sensors mounted on the caudal fin shaft. **Figure 31** shows the thrust force developed by the oscillating fin at a different frequency. It is observed that the thrust force increases up to f = 1.0 Hz and then decreases with increase in frequency. The maximum thrust force of about 34.06 N is measured at f = 1.0 Hz in surface condition. A maximum thrust force of 18.6 N is observed in submerged condition
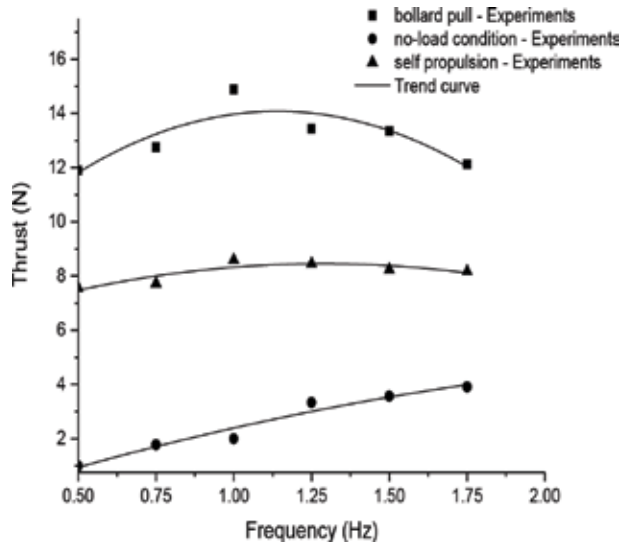
Figure 27.
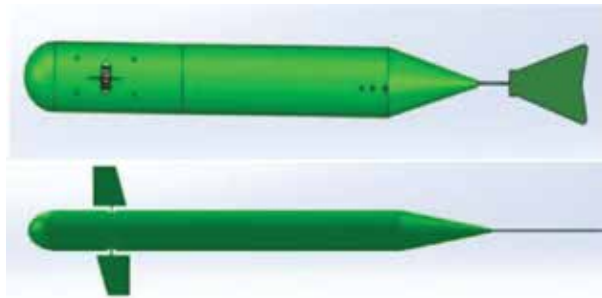*Thrust force developed by the oscillating foil in different ship model operating conditions.*

Figure 28.
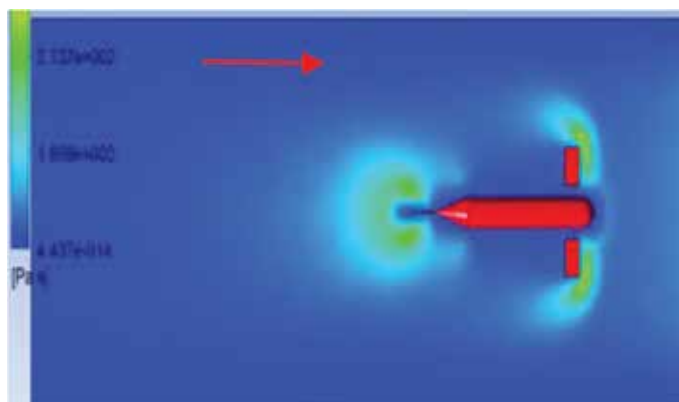*Robotic fish with pectoral and caudal fins.*

Figure 29.
Flow around the vehicle pectoral and caudal fins (V = 1 m/s).

at f = 0.75 Hz. In submerged condition, caudal fin deformed more due to higher loading and flexibility of fin resulting in reduced performance. As in the surface condition, the thrust produced by the oscillating fin reduced after f = 1.0 Hz.
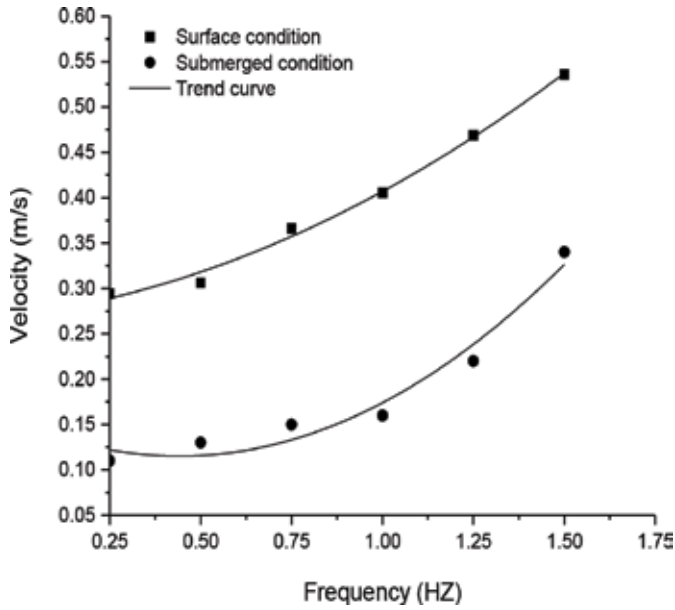
Figure 30.
Vehicle velocity at different frequencies of the fin at surface piercing and submerged conditions.
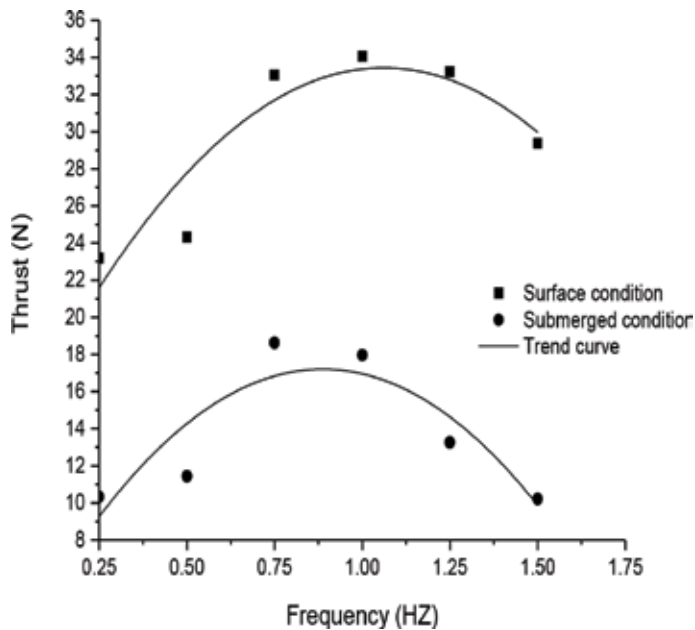

Figure 31.
Thrust force developed by the foil at different frequencies at the surface and submerged conditions.

Higher frequency of oscillation results in more flow separation and results in thrust reduction.

4. Summary and conclusions

The design and development of biomimetic robots based on nature locomotion involves multidisciplinary studies such as the biological behavior of fish, flow

visualization around it and its fins during swimming, and numerical and experimental determination of thrust and drag forces. Experimental and numerical studies are carried out to determine the propulsive performance of bioinspired aquatic vehicle fitted with tandem flapping foils. The work has taken shape with the selection of a ship model fitted with a pair of flexible flapping foil at its bottom resembling penguin flippers. The propulsion mechanism developed in Central Workshop (CWS) at IIT Madras is installed at the ship model bottom and then the fins oscillate at different amplitudes and frequencies. Rigid and flexible flapping foils are used in the studies to determine the hydrodynamic forces generated by the flapping foils. In understanding the limitations of potential theory in determining different hydrodynamic parameters, RANSE-based CFD method is used extensively for the numerical studies. A general purpose fluid flow solver FLUENT is used by exploring and exploiting its features to induce dynamic simulations to the fins so as to duplicate the oscillating fin system in the numerical environment. Experimental studies on the ship model, fitted with these penguin type flipper at its bottom, are carried out in the towing tank facility. The thrust generation capability and efficiency of flapping hydrofoils at different parameters (α_0, St, ψ) are studied experimentally and numerically.

In order to understand the natural characteristics of fish swimming, PIV measurements are carried out on a live shark fish to understand and analyze the hydrodynamic behavior of its propulsion using the caudal fin. Sharks exhibit high-performance aquatic locomotion through oscillation of its forked caudal fin. The velocity vector plots show that caudal fins produce reverse von Karman vortex street resulting in an afterward jet formation that gives the propulsive force. This study helped in understanding the flow pattern around the fish and its fins to take the information further to engineering applications. These type of propulsors with improved propulsive characteristics, maneuverability, and creation of less turbulence are inspiring qualities for its adoption in the propulsion of autonomous marine vehicles.

Inspired by the natural aquatic swimming fish, bioinspired remotely operated surface ship and underwater vehicle fitted with caudal fin is studied in detail. The performance of a remotely operated surface ship model propelled by tuna-mimicking caudal fins is evaluated. Design of caudal fin and its control system are carried out. Using the experimental set-up, swimming velocities and thrust forces of a surface ship fitted with the caudal fin in the axial direction are measured at different oscillation frequencies and amplitude of the fin. This information inspired and helped in thinking about the development of a combination of oscillating foil system constituted by the caudal and a pair of pectoral fins to propel underwater vehicles. Numerical studies are used to estimate the drag forces on the body with the bare hull and also the hull fitted with pectoral and caudal fins. The vehicle fitted with caudal fin is studied experimentally at different frequencies and constant amplitude. The thrust force is measured using the strain gauges mounted on the caudal fin connecting rod. The propulsive forces are measured at different oscillation frequencies for the case when the body is surface and below the surface. The vehicle has the ability for better performance, by incorporating pectoral fins also, which will generate additional thrust and also help in the better maneuvering of the vehicle.

Acknowledgements

Conflict of interest

The authors declare that they have no competing interests.

Author details

Naga Praveen Babu Mannam* and P. Krishnankutty
Indian Institute of Technology Madras, Chennai, India

*Address all correspondence to: mpraveenmn@gmail.com

IntechOpen

References

[1] Schouveiler L, Hover FS, Triantafyllou MS. Performance of flapping foil propulsion. Journal of Fluids and Structures. 2005;**20**(7): 949-959

[2] Gottlieb JR, Tangorra JL, Esposito CJ, Lauder GV. A biologically derived pectoral fin for yaw turn maneuvers. Applied Bionics and Biomechanics. 2010;**7**(1):41-55

[3] Lauder GV, Madden PGA, Tangorra JL, Anderson E, Baker TV. Bioinspiration from fish for smart material design and function. Smart Materials and Structures. 2011;**20**(9): 094014

[4] Shinde SY, Arakeri JH. Flexibility in flapping foil suppresses meandering of the induced jet in absence of free stream. Journal of Fluid Mechanics. 2014;**757**:231-250

[5] Lucas KN, Thornycroft PJ, Gemmell BJ, Colin SP, Costello JH, Lauder GV. Effects of non-uniform stiffness on the swimming performance of a passively-flexing, fish-like foil model. Bioinspiration & Biomimetics. 2015; **10**(5):056019

[6] Lua KB, Lu H, Zhang XH, Lim TT, Yeo KS. Aerodynamics of two-dimensional flapping wings in a tandem configuration. Physics of Fluids. 2016; **28**(12):121901

[7] Yang L, Su YM. CFD simulation of flow features and vorticity structures in tuna-like swimming. China Ocean Engineering. 2011;**25**(1):73-82

[8] Hao D, Bao-Wei S, Yong-hui C. Design and prototype development of a 1-DOF flapping-foil and gliding UUV. Journal of Marine Science: Research and Development. 2012;**S10**:001. DOI: 10.4172/2155-9910.S10-001

[9] Ahmed T, Welaya Y, Abdulmotaleb S. Numerical modeling of the hydrodynamic performance of hydrofoils for auxiliary propulsion of ships in regular head-waves. In: Proceedings of the ASME 2017 36th International Conference on Ocean, Offshore and Arctic Engineering OMAE 2017; 25-30 June 2017; Trondheim, Norway; 2017

[10] Mannam NP, Krishnankutty P, Vijayakumaran H, Sunny RC. Experimental and numerical study of penguin mode flapping foil propulsion system for ships. Journal of Bionic Engineering. 2017;**14**(4):770-780

[11] Babu MNP, Mallikarjuna JM, Krishnankutty P. Hydrodynamic study of freely swimming shark fish propulsion for marine vehicles using 2D particle image velocimetry. Robotics and Biomimetics. 2016;**3**(1):3

[12] Mannam NP, Krishnankutty P. Hydrodynamic study of flapping foil propulsion system fitted to the surface and underwater vehicles. Ships and Offshore Structures. 2018:1-9

Edited by Alessandro Serpi and Mario Porru

The transport sector is one of the most valuable sectors in the world. It represents the large oil consumers but still relies mainly on fossil fuels. Since the world trend in fossil fuel use is expected to increase further, a more sustainable transportation system is unavoidable to cope with emerging economic and social issues, such as massive energy consumption and emissions of pollutant gases. In this regard, this book provides an overview of some recent and promising technological advancements in propulsion systems, ranging from on-board components to different propulsion system architectures. In particular, the book aims at giving a brief but significant insight into propulsion system design and architecture, by covering different topics and application fields (road, marine, and aerospace).

IntechOpen